

FINAL REPORT

Sources of Organic Particulate Matter in Houston: Evidence from DISCOVER-AQ data - Modeling and Experiments

AQRP Project 14-024

Prepared by:

Lea Hildebrandt Ruiz, The University of Texas at Austin

Bonyoung Koo and Greg Yarwood, Ramboll Environ

The University of Texas at Austin
Center for Energy and Environmental
Resources
10100 Burnet Road
Bldg. 133, CEER
Austin, Texas 78758

Ramboll Environ
773 San Marin Drive, Suite 2115
Novato California, 94998

QA Requirements: Audits of Data Quality: 10% Required



Acknowledgement

The preparation of this report is based on work supported by the State of Texas through the Air Quality Research Program administered by The University of Texas at Austin by means of a Grant from the Texas Commission on Environmental Quality (TCEQ).

Table of Contents

Acknowledgement	2
Executive Summary.....	6
1.0 Introduction	8
2.0 Inventory Analysis	10
3.0 Laboratory Experiments.....	11
3.1 Experimental Procedures.....	11
3.1.1 Instrument Descriptions	12
3.1.2 Calibration Procedures.....	16
3.1.2 Data Analysis.....	17
3.2 Experimental Results	21
3.2.1 Formation of SOA	21
3.2.2 Composition of SOA.....	25
3.2.3 Volatility (VBS parameters) of SOA.....	26
4.0 Chemical Mechanism.....	29
5.0 Photochemical Modeling.....	30
6.0 DISCOVER-AQ Data Analysis	35
6.1 Description of Site Location and Instrumentation	35
6.2 ACSM Operation, Calibration and Data Work-up	36
6.2.1 Adjustments to standard fragmentation table	37
6.2.2 Quantification, Data Averaging and Detection limits.....	38
6.2.3 Diurnal patterns: analysis of statistical significance and characterization.....	39
6.3 Organic Aerosol Concentrations and Composition.....	40
6.3.1 Comparison to other instruments	43
7.0 Positive Matrix Factorization (PMF) Analysis.....	46
8.0 Model Evaluation.....	51
8.1 Evaluation of OC and EC using PM2.5 Filter Measurements.....	51
8.2 Evaluation of OA mass and O:C ratio using ACSM PM1 measurements	56
8.3 Evaluation of OA composition using PMF analysis.....	60
8.4 Contemporary vs Fossil Carbon Analysis	63
8.5 Contributions of SOA Formation Pathways.....	65

8.6 Improvements to the Base Case Modeling.....	67
8.6.1 Additional Basis Set for CIOA	67
8.6.2 Updated Aerosol Yields for Monoterpene+NO ₃	68
8.6.3 Adjusted Aerosol Yields for IVOC Precursors.....	68
8.6.4 Fixed Biomass Burning POA Emissions from Area Sources.....	69
8.6.5 SOA Formation from Alkane VOC Precursors	69
8.7 Evaluation of the Revised Model Performance	75
9.0 Audits of Data Quality.....	82
10.0 Conclusions and Recommendations	83
11.0 References	86

Figures

FIGURE 1. OUTLINE OF PROJECT TASKS	9
FIGURE 2. PHOTOGRAPHS OF THE ENVIRONMENTAL CHAMBER AND SURROUNDING INSTRUMENTATION.	12
FIGURE 3. ILLUSTRATION OF THERMODENUDE SAMPLING SCHEMES.....	14
FIGURE 4. SCHEMATIC OF THERMODENUDE BODY	15
FIGURE 5. THERMODENUDE TEMPERATURE PROFILE.....	16
FIGURE 6. ORGANIC AEROSOL FORMED FROM THE PHOTO-OXIDATION OF N-PENTADECANE	23
FIGURE 7. ORGANIC AEROSOL FORMED FROM THE PHOTO-OXIDATION OF MINERAL SPIRITS	24
FIGURE 8. ORGANIC AEROSOL MASS YIELDS FROM THIS AND PREVIOUS WORK	25
FIGURE 9. SUMMARY OF ORGANIC AEROSOL COMPOSITION	26
FIGURE 10. THERMOGRAM OF SOA GENERATED.....	27
FIGURE 11. EFFECTIVE ENTHALPY OF VAPORIZATION OF SOA FORMED FROM IVOC OXIDATION	27
FIGURE 12. ACCOMMODATION COEFFICIENT OF SOA FORMED FROM IVOC OXIDATION	28
FIGURE 13. VOLATILITY DISTRIBUTION OF SOA FORMED	28
FIGURE 14. CAMX MODELING DOMAIN	31
FIGURE 15. DAILY TOTAL EMISSIONS IN THE 4-KM MODELING DOMAIN (AVERAGED OVER SEPTEMBER)	35
FIGURE 16. TIME SERIES OF ORGANICS, NITRATES, SULFATE AND AMMONIUM.....	41
FIGURE 17. DIURNAL CYCLE OF ORGANIC, SULFATE AND NITRATE MASS CONCENTRATIONS.....	42
FIGURE 18. DIURNAL CYCLE OF ORGANIC AEROSOL OXYGEN TO CARBON RATIO (O:C).....	43
FIGURE 19. COMPARING PM ₁ MEASUREMENTS TAKEN BY THE ACSM AND THE SEMS.	44
FIGURE 20. COMPARING MEASUREMENTS TAKEN BY THE ACSM AND FROM FILTERS.....	45
FIGURE 21. PROFILES OF SELECTED PMF FACTORS.	48
FIGURE 22. TIME SERIES OF SELECTED FACTORS	49
FIGURE 23. DIURNAL CYCLE OF PMF FACTORS.	50
FIGURE 24. MODELED VS. OBSERVED OC AND EC CONCENTRATIONS AT CONROE.....	52

FIGURE 25. MODELED VS. OBSERVED OC AND EC CONCENTRATIONS AT MOODY TOWER	53
FIGURE 26. MODELED VS. OBSERVED OC AND EC CONCENTRATIONS AT MANVEL CROIX	54
FIGURE 27. HOURLY OBSERVED PM1 AND MODELED PM2.5 OA CONCENTRATIONS AT CONROE.	57
FIGURE 28. DIURNAL CYCLES OF OBSERVED AND MODELED OA CONCENTRATIONS AT CONROE.	58
FIGURE 29. DIURNAL CYCLES OF OBSERVED AND MODELED O:C RATIOS.	59
FIGURE 30. COMPARISON OF OA COMPOSITION BY PMF AND CAMX.	61
FIGURE 31. AVERAGE DIURNAL CYCLES OF OA COMPOSITION BY PMF AND CAMX.	62
FIGURE 32. OBSERVED VS. MODELED ORGANIC CARBON COMPOSITIONS	64
FIGURE 33. CONTRIBUTIONS TO DAILY AVERAGE SECONDARY OC CONCENTRATIONS	66
FIGURE 34. OC CONCENTRATIONS PREDICTED BY THE BASE MODEL AND THE REVISED MODEL WITH COOKING INFLUENCED ORGANIC AEROSOL	70
FIGURE 35. OC CONCENTRATIONS PREDICTED BY THE BASE MODEL AND THE REVISED MODEL WITH UPDATED MONOTERPENE AEROSOL YIELDS	71
FIGURE 36. OC CONCENTRATIONS PREDICTED BY THE BASE MODEL AND THE REVISED MODEL WITH ADJUSTED IVOC AEROSOL YIELDS.	72
FIGURE 37. OC CONCENTRATIONS PREDICTED BY THE BASE MODEL AND THE REVISED MODEL WITH FIXED BIOMASS BURNING POA EMISSIONS FROM AREA SOURCES	73
FIGURE 38. OC CONCENTRATIONS PREDICTED BY THE BASE MODEL AND THE REVISED MODEL WITH SOA FORMATION FROM LONG ALKANE VOC PRECURSOR	74
FIGURE 39. MODELED VS. OBSERVED OC CONCENTRATIONS USING THE REVISED MODEL	76
FIGURE 40. HOURLY PM2.5 OA CONCENTRATIONS BY THE REVISED MODEL AND ACSM MEASUREMENTS OF PM1 OA AT CONROE.	78
FIGURE 41. DIURNAL CYCLES OF MODELED OA CONCENTRATIONS AND O:C RATIOS AT CONROE.	79
FIGURE 42. HOURLY OA COMPOSITION AND AVERAGE DIURNAL CYCLE OF OA COMPOSITION	80
FIGURE 43. CONTEMPORARY CARBON FRACTIONS ESTIMATED BY RADIOCARBON ANALYSIS ON THE HIGH VOLUME FILTER SAMPLES (HV2.5) AND PREDICTED BY THE REVISED MODEL	81

Tables

TABLE 1. LIST OF IVOCs STUDIED AND THEIR PROPERTIES	10
TABLE 2. SUMMARY OF MEASURED SPECIES AND INSTRUMENTATION USED	13
TABLE 3. INPUTS TO MASS TRANSFER MODEL	19
TABLE 4. SOLUTION SPACE USED BY MASS TRANSFER MODEL	21
TABLE 5. EXPERIMENTAL CONDITIONS FOR ALL EXPERIMENTS CONDUCTED	21
TABLE 6. EVAPORATION MODEL INPUTS AND RESULTS	29
TABLE 7. SOA SURROGATES AND VBS SOA MASS YIELDS USED FOR IVOCs (JATHAR ET AL., 2014).	29
TABLE 8. MOLECULAR PROPERTIES OF THE 1.5-D VBS SPECIES (KOO ET AL., 2014)	30
TABLE 9. PHYSICS OPTIONS USED IN THE WRF SIMULATION OF THE AUGUST-SEPTEMBER, 2013 MODELING PERIOD	32
TABLE 10. FRACTIONS OF NMOG EMISSIONS BY COMBUSTION SOURCE TYPE	34
TABLE 11. PERFORMANCE METRICS ^A OF MODELED OC AND EC CONCENTRATIONS AGAINST FILTER MEASUREMENTS	55
TABLE 12. VOLATILITY DISTRIBUTION OF POA EMISSIONS.	67
TABLE 13. VBS SOA MASS YIELDS FOR THE REACTION OF MONOTERPENE WITH NO ₃	68
TABLE 14. PERFORMANCE METRICS OF REVISED MODEL OC CONCENTRATIONS AGAINST FILTER MEASUREMENTS	77

Executive Summary

The new annual National Ambient Air Quality Standard (NAAQS) for particulate matter smaller than 2.5 micrometers in diameter (PM_{2.5}) brings the Houston region to near non-attainment for PM_{2.5}, underlining the importance of understanding the composition and sources of PM_{2.5} in Houston. Over half of fine PM in the Houston region is composed of organic material including primary organic aerosol (POA), which are compounds that are emitted as particles and have not reacted in the atmosphere and secondary organic aerosol (SOA), which is formed when gas-phase compounds undergo one or more chemical transformations in the gas phase, forming less volatile compounds that then partition between the gas and particle phases. Understanding the sources and formation of organic aerosol is therefore very complex, and significant uncertainties remain. In this work laboratory experiments, ambient measurements and a photochemical model were combined to better understand the sources of organic particulate matter in the Houston region.

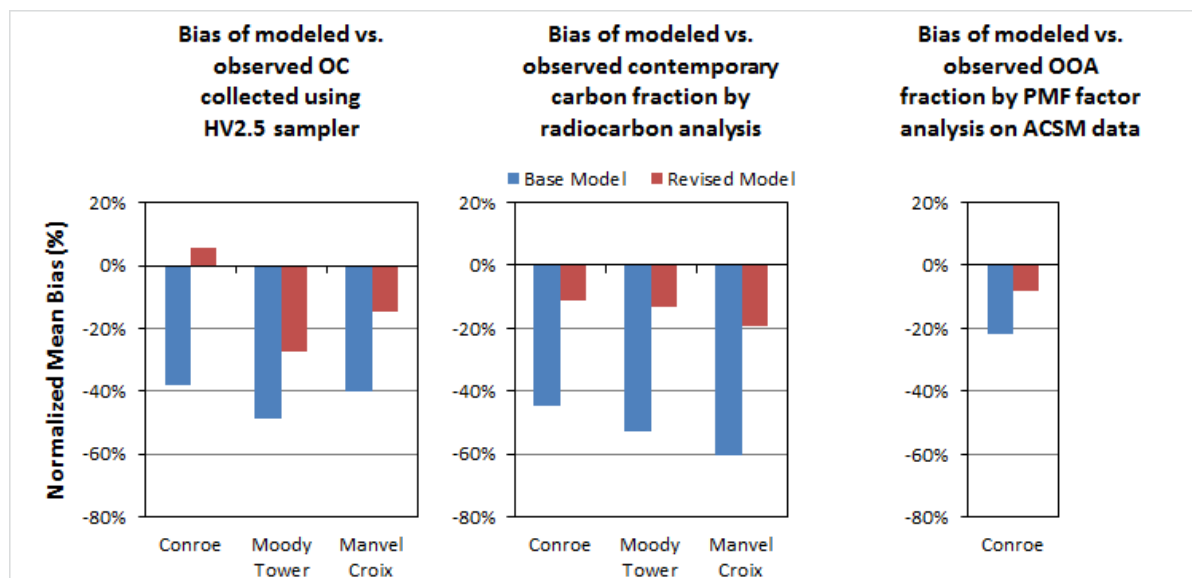
Sixteen laboratory chamber experiments were conducted to form SOA from the oxidation of different intermediate volatility organic compounds (IVOCs). Out of the six IVOCs studied (n-pentadecane, 2,6,10-trimethyldodecane, 2-methylnaphthalene, butyl CARBITOL™, Texanol™, and mineral spirits), all but Texanol™ formed secondary organic aerosol. SOA mass yields of 2-methylnaphthalene measured in this study agreed well with literature data. A novel contribution of this work is quantification of the SOA yield from butyl CARBITOL™, a glycol ether used in surface coatings. The SOA yields from this compound were similar to yields from 2-methylnaphthalene. The vapor pressure of SOA formed from n-pentadecane, 2,6,10-trimethyldodecane and mineral spirits was analyzed using a thermodenuder developed as part of this work. The SOA formed from mineral spirits was more volatile than the SOA formed from n-pentadecane and 2,6,10-trimethyldodecane (a branched pentadecane).

Ambient data collected during an ambient measurement campaign in Houston, TX termed Deriving Information on Surface Conditions from Column and Vertically Resolved Observations Relevant to Air Quality (DISCOVER-AQ, <http://discover-aq.larc.nasa.gov/>) were analyzed focusing on the concentrations and composition of fine particulate matter. The data were obtained at an air quality monitoring ground site in Conroe, TX (30.350278°N, 95.425000°W) located approximately 60 km north-northwest from the Houston, TX urban center and approximately 125 km northwest of the nearest coastline. On average 65% of the mass of non-refractory particulate matter smaller than 1 micrometer in diameter (PM₁) was due to organic material (including organic nitrates), highlighting the importance of organics in controlling fine PM mass in the Houston region. Positive matrix factorization analysis (PMF) was applied to the organic aerosol mass spectra measured by aerosol chemical speciation monitor (ACSM). The data were best represented by two factors of oxygenated organic aerosol (OOA), a more oxidized OOA (MO- OOA) and a less oxidized OOA (LO-OOA), as well as a fresher factor representative of hydrocarbon like organic aerosol (HOA) and biomass burning organic aerosol (BBOA). According to this analysis on average 85% of the organic aerosol sampled at

Conroe consisted of oxygenated organic aerosol, highlighting the importance of atmospheric processing in influencing concentrations of organic particulate matter in the Houston region.

The Comprehensive Air quality Model with Extensions (CAMx) utilizing the 1.5 dimensional volatility basis set (1.5-D VBS) was applied to simulate organic aerosol formation in the Houston region during the 2013 DISCOVER-AQ campaign. Emissions of IVOC from major combustion sources were added using IVOC fractions of total non-methane organic gas (NMOG) emissions estimated from environmental chamber studies. The model results were evaluated against PM_{2.5} filter measurements at Conroe, Moody Tower and Manvel Croix and PM₁ ACSM measurements at Conroe. The base model generally underpredicts the observed total organic carbon (OC) concentrations and PMF-estimated OOA fractions. The radio carbon analysis indicates that the base model underestimates contemporary carbon fractions while the modeled fossil carbon mass is comparable to observations.

Several improvements were made to the base model: a basis set for cooking-influenced organic aerosol was added, the organic aerosol mass yields from the reactions of monoterpenes and NO₃ were updated, the organic aerosol mass yields of IVOC precursors were adjusted, an error in the emissions of primary organic aerosol from biomass burning area sources was corrected and the formation of secondary organic aerosol from long alkane precursors (8-11 carbons) was added. The base case scenario was simulated again with the revised model. The results show that the revised model gives much better agreement than the base model with the measured OC concentrations, PMF-based OOA fractions, and contemporary carbon fractions by radiocarbon analysis.



The supplemental measurements in the evaluation database (including filter OC and radiocarbon analysis data, ACSM measurements and PMF analysis) were very useful in guiding model improvements and providing a more informative evaluation. This project greatly benefited from the AQRP projects 14-024 and 14-029 that collected these data.

1.0 Introduction

The TCEQ is responsible for managing the impacts of Texas' emissions on its air quality. The Texas State Implementation Plan (SIP) includes strategies for attaining air-quality standards for ozone, fine particulate matter (PM_{2.5}) and regional haze. Regional photochemical models and their chemical mechanisms are important tools for the development of SIPs because they establish quantitative linkages between primary emissions and secondary pollutants such as ozone and particulate matter. Laboratory chamber experiments can be used to develop and test chemical mechanisms or parameterizations for the models. Ambient observations are another important tool because they allow observation of the concentrations and processing of pollutants occurring in the complex atmosphere, and they can also be used for testing of regional photochemical models. The combination of photochemical models, laboratory experiments and ambient measurements is therefore an especially powerful tool for understanding and managing Texas air quality. We combined these tools to better understand the sources of fine PM in the Houston region.

The United States Environmental Protection Agency recently lowered the annual National Ambient Air Quality Standard (NAAQS) for PM_{2.5} from 15 to 12 $\mu\text{g m}^{-3}$ (US EPA, 2013). This new annual standard brings the Houston region to near non-attainment for PM_{2.5}, underlining the importance of understanding the composition and sources of PM_{2.5} in the Houston region. The University of Texas at Austin (UT-Austin) under the leadership of Principle Investigator (PI) Lea Hildebrandt Ruiz recently collected air-quality measurements in the Houston region as part of AQRP project 12-012, including measurements of PM concentration and composition, as well as the concentrations of gas-phase species (Hildebrandt Ruiz and Yarwood, 2013). Preliminary data analysis indicated that the majority – up to 70% – of fine PM measured in Conroe, TX (~ 70 km North of the urban center) was composed of organic material (Hildebrandt Ruiz and Yarwood, 2013). This is consistent with studies conducted during the last decade, which have also found that a significant fraction of fine PM in Texas is composed of organic material (Allen, 2005; Bahreini et al., 2009). An improved understanding of Houston organic aerosol is therefore essential and will directly benefit the TCEQ in understanding how to manage Houston's air quality.

Traditionally, organic aerosol (OA) has been classified as primary or secondary OA (POA or SOA). In this classification, POA refers to compounds that are emitted as particles and have not reacted in the atmosphere. SOA is formed when gas-phase compounds undergo one or more chemical transformations in the gas phase, forming less volatile compounds that then partition between the gas and particle phase (Donahue et al., 2006; Pankow et al., 2001). These gas-phase precursors of SOA are classified (in decreasing order of vapor pressure/volatility) as volatile organic compounds (VOC), intermediate volatility organic compounds (IVOC) or semivolatile organic compounds (SVOC). Sources of OA in Houston include POA and SOA from urban anthropogenic activity, the petrochemical industry and fires, as well as SOA from biogenic VOC. Understanding the sources and formation of OA is therefore very complex, and significant uncertainties remain.

This project included analysis of recently collected ambient data during DISCOVER-AQ, new environmental chamber experiments and photochemical modeling of the Houston region. Laboratory experiments focused on the formation of OA from IVOC because the contributions from these species have not received much attention, the emissions of IVOC are expected to be high in Houston, and the contributions of IVOC to SOA appear to be important but underestimated (Robinson et al., 2007; Shrivastava et al., 2008). For the formation of SOA from VOC and IVOC precursors the photochemical model uses a new state of the art approach based on the Volatility Basis Set (VBS) (Donahue et al., 2006) which has recently been implemented in CAMx (and also the Community Multi-scale Air Quality (CMAQ) model) to account for important aspects of OA formation such as the semi- volatile nature of POA and NO_x-dependent yields for SOA (Koo et al., 2013). This new scheme accounts for systematic variations in both volatility and oxidation state (the organic aerosol O:C ratio) and is referred to as a 1.5-dimensional (1.5D) VBS.

The tasks which were part of this work and how they are inter-connected are outlined in Figure 1.

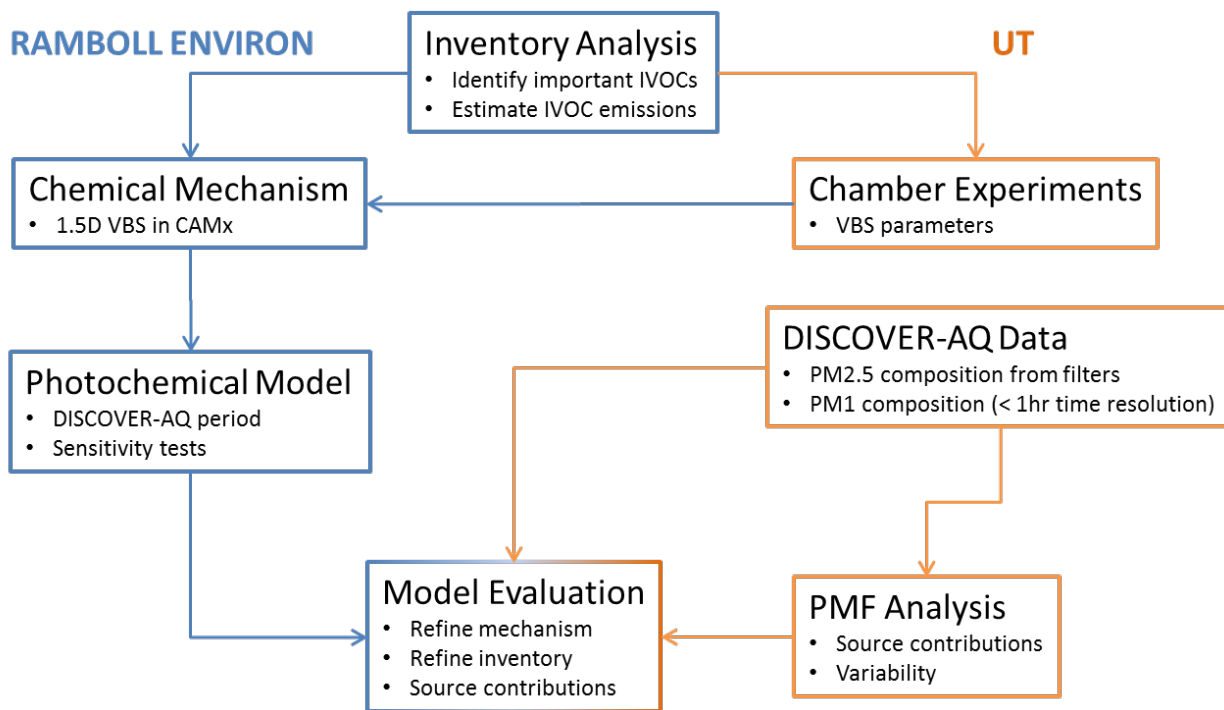


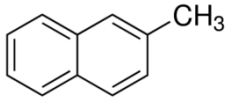

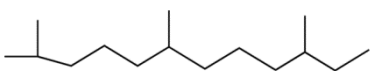
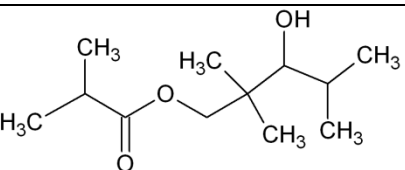
Figure 1. Outline of project tasks

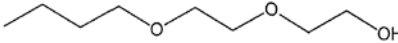
2.0 Inventory Analysis

Information on the magnitude of IVOC emissions is very limited. Recently, Jathar et al. (2014) have estimated IVOC fractions of total non-methane organic gas (NMOG) emissions from gasoline engines, diesel engines and biomass burning. Using this information, we were able to estimate IVOC emissions for mobile source, area source and fire emission sectors as discussed further in Section 5.

Seeking information on IVOC emissions from the point source sector we reviewed the TCEQ's point source emission inventory for Harris County. Specifically, we reviewed version 4b of the 2012 STARS emissions inventory which contains speciated NMOG emissions reported by industry. This inventory reports 19,518 tons/year of NMOG for Harris County classified as 491 compounds or mixtures of compounds. The mixtures of compounds are poorly defined and account for a substantial fraction of NMOG (e.g., 3,306 tons/year of VOC-Unclassified) and the TCEQ has procedures for disaggregating mixtures similar to those described in (Pacific Environmental Services, 2002). A review of compounds (rather than mixtures) with emissions of more than 1 ton/year in Harris County identified two potential IVOCs: butyl CARBITOL™ (3.5 tons/year) and methyl naphthalene (1.7 tons/year). Compounds were considered potential IVOCs if they have higher molecular weight and lower boiling point than naphthalene. Several compound mixtures associated with petrochemicals processing were identified that could contain IVOCs, including Crude Oil (312 tons/year), Fuel Oil-Unidentified (73 tons/year), Gas Oil (65 tons/year), Vacuum Bottoms (37 tons/year) and Asphalt Fumes (1.1 tons/year). Table 1 summarizes the list of IVOCs we decided to study in environmental chamber experiments.

Table 1. List of IVOCs studied and their properties

IVOC name	Chemical formula	Molecular Weight	Boiling point (°C)	Chemical structure
2-methylnaphthalene (MN)	C ₁₁ H ₁₀	142.2	241	
n-pentadecane	C ₁₅ H ₃₂	212.4	270	
2,6,10-trimethyldodecane (TMD)	C ₁₅ H ₃₂	212.4	249	
Texanol™	C ₁₂ H ₂₄ O ₃	216.3	254	

IVOC name	Chemical formula	Molecular Weight	Boiling point (°C)	Chemical structure
butyl CARBITOL™	C ₈ H ₁₈ O ₃	162.2	230	
Mineral spirits	(several)			

2-methylnaphthalene (2-MN) was chosen as a proxy for polycyclic aromatic hydrocarbons (PAHs). The formation of organic aerosol from 2-MN was studied in previous work (Chan et al., 2009), and thus results for this IVOC can be compared to published data. Pentadecane was chosen as a proxy for a linear alkane IVOC. 2,6,10-Trimethyldodecane was chosen as proxy for a branched alkane IVOC. We also chose to study the SOA formation from oxidized IVOCs which, to our knowledge, has not been done before and presents a novel contribution. Texanol™ and butyl CARBITOL™ were chosen as they are abundant in water-based surface coatings (http://cfpub.epa.gov/si/speciate/ehpa_speciate_browser_details.cfm?ptype=G&number=3140) and are expected to have high emissions. Mineral spirits were chosen as they are widely used in surface coatings as a solvent. These compounds (mineral spirits, Texanol™ and butyl CARBITOL™) represent IVOCs from non-combustion sources, and the formation of organic aerosol from these sources has not previously been studied.

3.0 Laboratory Experiments

Environmental chamber experiments were conducted to form SOA from the oxidation of IVOC and to evaluate the oxidation state and vapor pressure (volatility) of the SOA formed.

3.1 Experimental Procedures

Experiments were conducted in the Atmospheric Physicochemical Processes Laboratory Experiments (APPLE) chamber located at the University of Texas at Austin (UT-Austin). Photographs of the chamber and surrounding instrumentation are shown in Figure 2. The APPLE chamber consists of a 12 m³ Teflon® bag (Welch Fluorocarbon) suspended inside of a temperature controlled enclosure. The walls of the enclosure are equipped with ultraviolet (UV) lights (204 GE T12 Blacklights; peak emission at 368 nm), which enable the simulation of photo-oxidation reactions; for example, the UV lights can photolyze hydrogen peroxide (H₂O₂) producing 2 hydroxyl radicals (HO·), and it can photolyze nitrous acid (HONO) producing HO· and nitric oxide (NO). A typical experiment started by filling the Teflon® bag with clean air, produced using an Aadco zero air generator (Model 737-14A). Measurements were taken with only clean air in the chamber, and they confirmed that the air was indeed clean. Inorganic seed particles (usually ammonium sulfate, (NH₄)₂SO₄) are then injected which serve as surface area

onto which oxidized organic vapors can condense, and which aid in the correction for wall losses (Hildebrandt et al., 2009). Propene is injected which serves as a tracer for OH radical concentrations. The IVOC of choice was then injected using a heated injector which was designed and built for this project. An oxidant precursor (H_2O_2 or HONO) was also injected. When everything was injected into the chamber and well mixed, as indicated by all species concentrations reaching constant levels, the UV lights were turned on photolyzing H_2O_2 or HONO to produce OH and commence the oxidation reactions to form SOA.

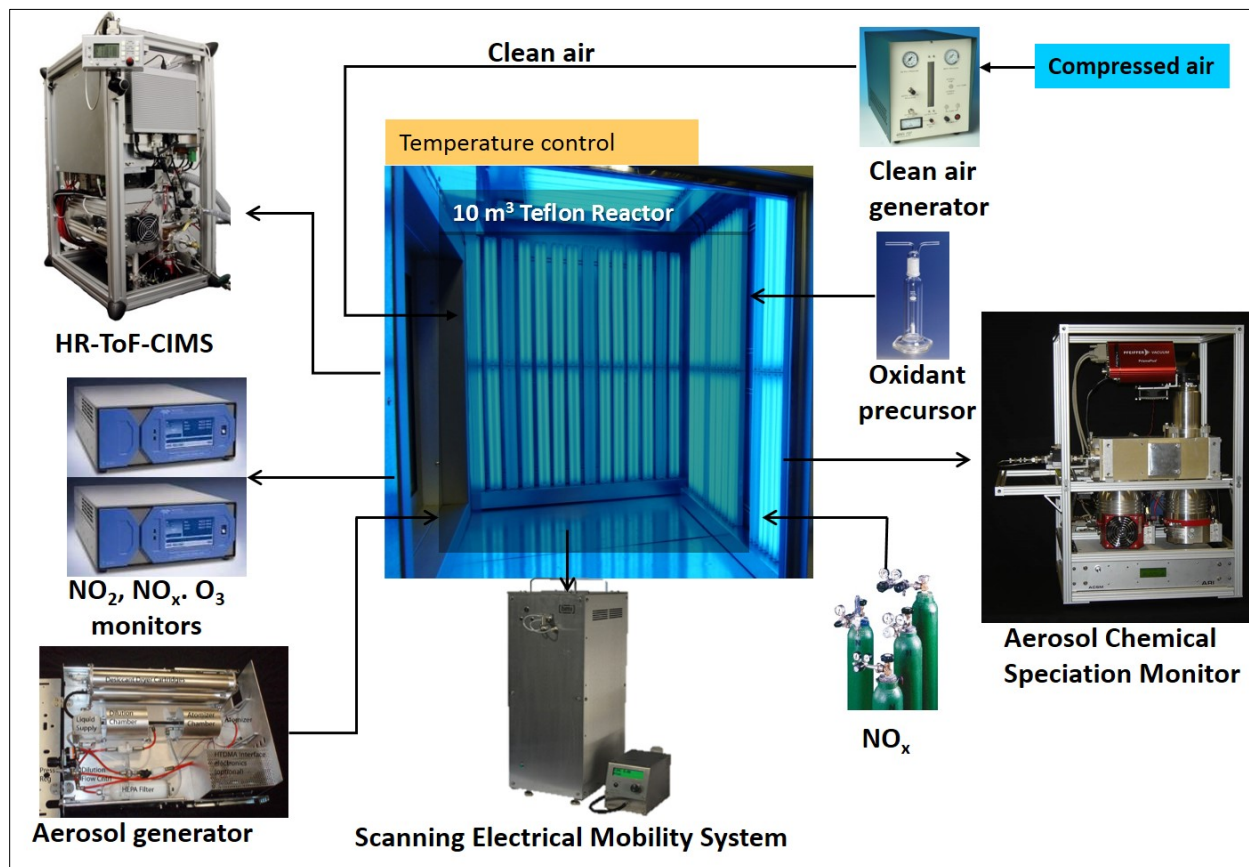


Figure 2. Photographs of the environmental chamber and surrounding instrumentation.

3.1.1 Instrument Descriptions

The concentration and composition of gas- and particle-phase species were monitored throughout each experiment. Table 2 summarizes the instruments used for gas- and particle phase measurements. The amount of SOA formed was monitored using an aerosol chemical speciation monitor (ACSM, Ng et al., 2011), which measures non-refractory PM_{10} species (organics, nitrate, sulfate and ammonium). The volume of SOA formed was measured using a scanning electrical mobility system (SEMS, Brechtel Manufacturing, Inc.), which measures

particle size distributions from which total particle volume can be calculated. Data from the SEMS was used to correct the ACSM data for collection efficiency. The ACSM also measures the total organic aerosol mass spectrum, from which the SOA oxygen-to-carbon ratio (O:C) can be estimated (Aiken et al., 2008; Canagaratna et al., 2015).

Table 2. Summary of measured species and instrumentation used

Species	Instrumentation		
	Make and Model	Principle	Comments
Ozone (O ₃)	Teledyne Instruments Model 200E	Photometry	Standard photometric analyzer.
NO, nitrogen dioxide (NO ₂). NO _x	Teledyne Instruments Model 400E	Chemiluminescence	Standard ambient monitoring instrument for NO/NO ₂ /NO _x measurements.
NO ₂	Environnement, Inc.	Cavity Attenuated Phase Shift Spectroscopy	Measures NO ₂ without conversion to NO, thereby avoiding interference from other nitrogen-containing species.
Aerosol size distribution	SEMS, Brechtel, Inc.	Scanning Electric Mobility Spectrometer	Particle size based on electric mobility.
Aerosol (PM ₁) chemical composition	ACSM, Aerodyne Research, Inc.	Aerosol Chemical Speciation Monitor	PM ₁ bulk composition: particles are flash vaporized and resulting vapors are ionized via electron impact and analyzed via quadrupole mass spectrometry
VOC chemical composition	HR-ToF-CIMS, Aerodyne Research, Inc.	High Resolution Time of Flight Chemical Ionization Mass Spectrometer	Determines molecular formula of gas-phase species by time of flight; chemical ionization lessens fragmentation.

Some gas-phase species were monitored using UT Austin's High Resolution Time of Flight Chemical Ionization Mass Spectrometer (HR-ToF-CIMS). This commercially available instrument measures the chemical composition of gas-phase species (Yatavelli et al., 2012)

using a high resolution Time-of-Flight Mass Spectrometer (ToFMS) from ToFwerk AG (Thun, Switzerland). In contrast to the scanning procedures used by quadrupole mass spectrometers (QMS), ToFMS is a technique which simultaneously measures the concentrations of all mass-to-charge (m/z) values of interest. Pulses of ions are accelerated to a high kinetic energy and their subsequent travel times are measured and used to determine m/z values. Chemical ionization used in the HR-ToF-CIMS is a soft ionization technique which avoids fragmentation of the molecular components.

A thermodenuder (TD) was built to as part of this project to evaluate the volatility (vapor pressure) of the SOA formed. In a TD the aerosol is heated to a predefined and controlled temperature. The SOA is measured after being subjected to this heating and compared to the SOA that bypassed the TD, obtaining a so-called thermogram – the mass fraction of organic aerosol remaining after heating versus TD temperature. The TD set-up and two sampling schemes are illustrated in Figure 3 below.

The body of the TD used in this project was designed by UT-Austin and built by Swagelok®. Heating and temperature control of the TD is achieved using three sets of high temperature heating tapes (McMaster, 4550T111 and 4550T172), thermocouples (Omega Engineering, KMQSS-062U-5) and proportional-integral-derivative (PID) controllers (Omega Engineering, CN7500). A control module was purchased from Aerodyne Research, Inc. to interface with thermocouples, heating tapes, automated 3-way valves, PID controllers, and particle phase instruments (e.g. ACSM). Figure 4 below shows a schematic of the TD built by Swagelok®. A 1-meter 316 stainless steel (SS) seamless stainless steel tube (1.0'' OD, 0.065'' wall) was used. The heating region is comprised of three zones, each controlled by a set of heating tape, thermocouple, and PID controller. Each 1/16'' thermocouple is positioned using a Swagelok fitting to monitor the centerline temperature.

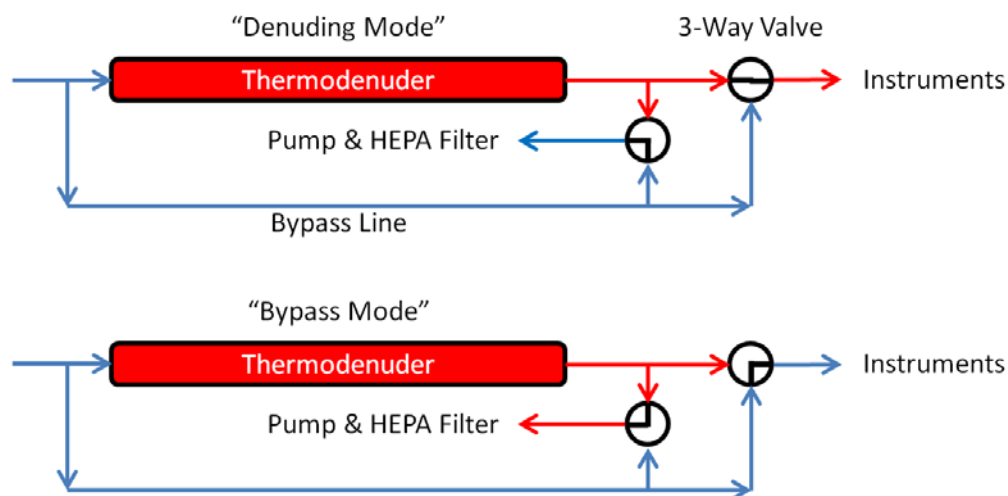


Figure 3. Illustration of thermodenuder sampling schemes showing bypass flow (blue lines) and thermally denuded flow (red lines). Exhaust flow is collected with High Efficiency Particulate Air (HEPA) filter.

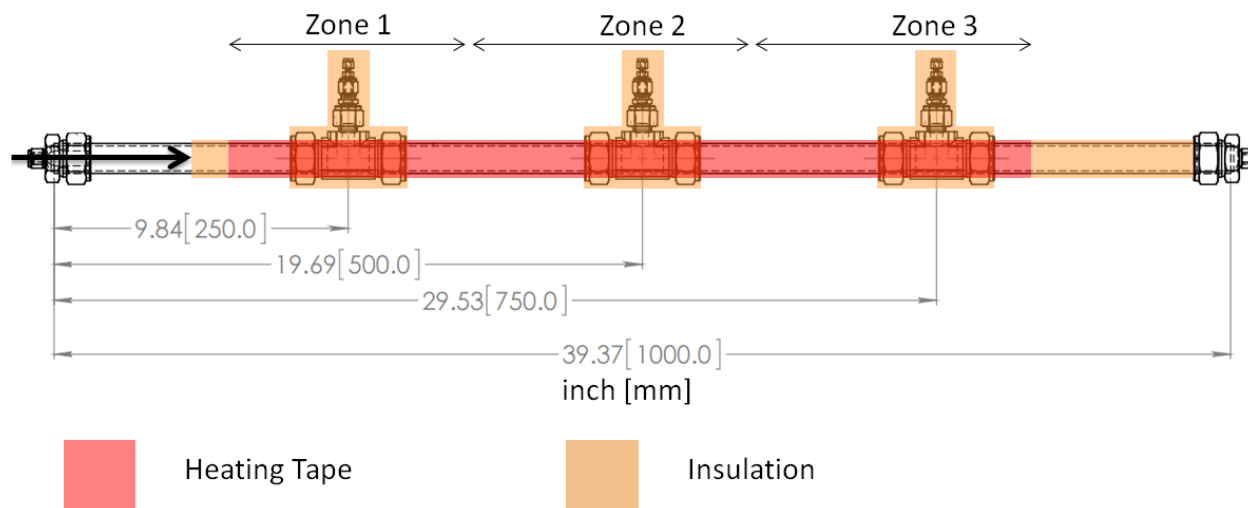


Figure 4. Schematic of thermodenuder body

The heating tape and insulation material were positioned to minimize variation in the temperature profile. Figure 5 below shows the temperature profile in the final design of the TD for the 50°C and 200°C setpoints at a flowrate of 1 liter per minute (LPM). At 1 LPM, the average sample flow velocity through the TD cross section (4.43 cm²) is 3.76 cm/s (assuming plug flow). Total residence time is 26.6 s. In practice, we define an effective heating region (21~78cm) as highlighted in Figure 5, where the measured centerline temperatures are 50.5 ± 1.9°C (3.8%) and 202 ± 11°C (5.4%) for 50°C and 200°C setpoints, respectively. The residence time in the heating region is therefore 57% of the total residence time, or 15.1s. Adjusted for temperature-dependent gas flow velocity (Huffman et al., 2009), the expected residence times are 12.3s and 8.2s for the 50°C and 200°C setpoints. At 0.6 LPM, the expected residence time are 20.5s and 13.7s. This residence time is higher than that of most previous TDs (e.g. Huffman et al., 2009), which is advantageous as it allows for more complete desorption.

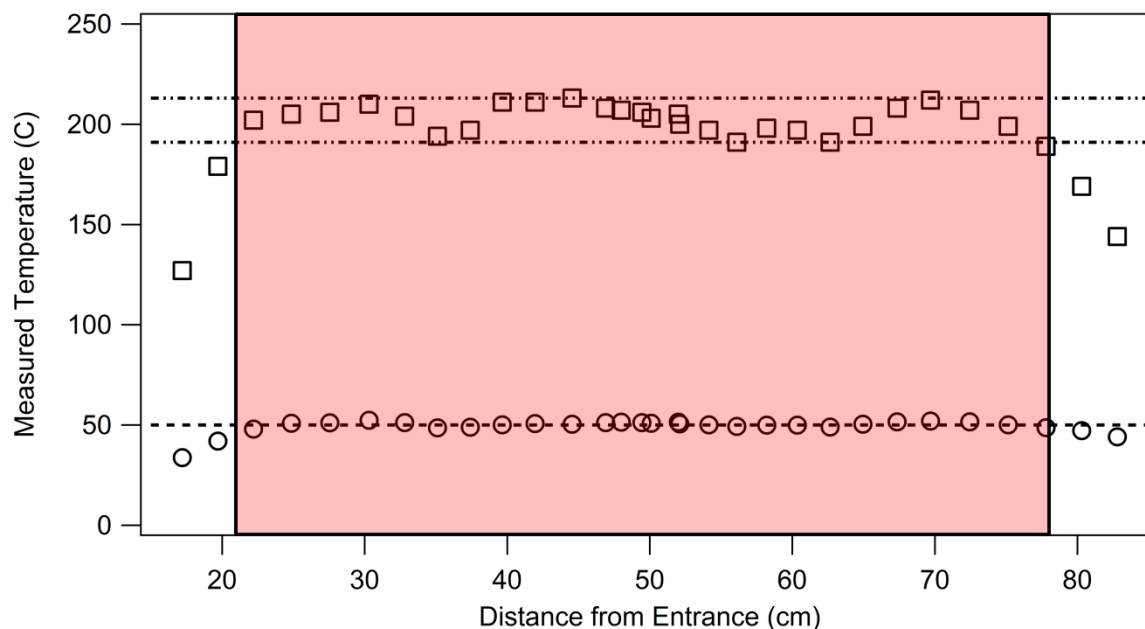


Figure 5. Thermodenuder Temperature Profile

3.1.2 Calibration Procedures

Standard gas monitors (O_3 , NO_x , NO_2)

Calibration methods and time resolution are similar for these instruments and are therefore described together here. These standard gas monitors were operated with 1-minute time resolution. The instruments were calibrated using a 4-point calibration curve before and after this set of experiments. In addition, a zero calibration was performed every day that the monitor is operated.

SEMS

The SEMS was operated with a 2-min time resolution. Particle sizing was confirmed using polystyrene latex spheres, using the procedures recommended by the manufacturer, before and after this set of experiments was performed. The plumbing delay between the DMA and the CPC was measured before this set of experiments was started, as recommended by the manufacturer.

ACSM

Sample flow into the ACSM was calibrated using a needle valve and flow measurement (gilibrator). The instrument response to nitrate, sulfate and ammonium was measured using standard calibration procedures suggested by the manufacturer before and after this set of experiments. The response factor of organics relative to nitrate has been measured previously and was used to quantify organics in this work. The collection efficiency of particles in the ACSM was estimated by comparing total concentrations measured by the ACSM to concentrations measured by the SEMS.

HR-ToF-CIMS

The HR-ToF-CIMS was operated at a 1 second time resolution, but the data will be averaged to 1 minute time resolution before archiving. Data from this instrument was not used quantitatively for this project. The HR-ToF-CIMS is a new, state-of-the art instrument, and standard QC procedures have not, yet, been established. We are continuing to communicate with the manufacturer (Aerodyne Research), as well as other researchers who have participated in the development and the first deployments of this instrument to confirm that the instrument is performing optimally.

3.1.2 Data Analysis

Mass spectrometer data from the HRTof-CIMS were saved in hierarchical data format (hdf) by the data acquisition software provided by the manufacturer. The data were processed using the data analysis software “Tofware”, provided by the manufacturer and written in Igor Pro (Wavemetrics). The functions in Tofware include a correction for the time of flight (ToF) duty cycle, a mass calibration based on selected known ions, interpolation and subtraction of the baseline, and determination of the resolution and shape of the ion peaks. The signal is then integrated - either all signal at a nominal mass to charge ratio (m/z) for unit mass resolution (UMR) analysis or each individual ion peak for high resolution (HR) analysis.

Data from the ACSM were analyzed using the data analysis software “ACSM Local” provided by the manufacturer and written in Igor Pro. In addition to calculating and displaying the chemically speciated aerosol mass loadings, ACSM Local has tools for examining the ACSM data stream in detail and monitoring instrument performance. Particles can bounce on the vaporizer resulting in a collection efficiency (CE) of less than 1. ACSM data were simultaneously corrected for CE and chamber wall losses by assuming that all particles lost to the walls are able to participate in gas-particle partitioning as if they were in suspension. This assumes that there are no mass transfer limitations to gas-particle partitioning close to the chamber walls. If this is the case, the ratio of organics (including organic nitrates) to ammonium sulfate should remain the same for suspended and wall-deposited particles, and corrected mass concentrations of organics and organic nitrates were obtained by multiplying the ratio of organics to ammonium sulfate by the initial ammonium sulfate concentration, as has been done in previous work (Hildebrandt et al., 2009).

Data from the Scanning Electric Mobility Spectrometer (SEMS) were also processed by the data analysis software provided by the manufacturer which “inverts” the data from units of number vs. voltage to number vs. particle mobility diameter (D_m), resulting in a particle size distribution. The software also corrects the data for multiply charged particles (assuming a Boltzmann charge distribution) and accounts for diffusion. The data are then read into and displayed in Igor Pro. Data from the NO_x , NO_2 and O_3 monitors were saved in time-stamped delimited text formats. These data did not need additional processing.

3.1.2.1 Quantification of SOA yields

The production of SOA from the oxidation of the IVOCs was quantified using a fractional aerosol mass yield, Y , which is defined as the ratio of the concentration of SOA formed (C_{OA}), divided by the mass of IVOC reacted (ΔC_{IVOC}):

$$Y = \frac{C_{OA}}{\Delta C_{IVOC}} \quad (1)$$

The SOA is assumed to be in equilibrium, and the partitioning of organic compounds between the gas and particle phase can be characterized by an effective saturation mass concentration C_i^* . The fraction of a given compound i in the condensed (particle) phase is given by (Donahue et al., 2006):

$$\xi_i = \left(1 + \frac{C_i^*}{C_{OA}}\right)^{-1} \quad \text{with } C_{OA} = \sum_i C_i \xi_i \quad \text{and} \quad (2)$$

$$Y = \frac{C_{OA}}{\Delta C_{IVOC}} = \frac{\sum_i C_i \xi_i}{\Delta C_{IVOC}} = \sum_i \frac{C_i}{\Delta C_{IVOC}} \left(1 + \frac{C_i^*}{C_{OA}}\right)^{-1} \quad (3)$$

where C_i is the total concentration of compound i .

The amount of IVOC reacted was estimated as follows: First, the concentrations of OH were calculated based on the observed decay of propene. Then, the amount of IVOC reacted was estimated based on known rates of reaction between the IVOC and OH, also taking into account the measured IVOC wall losses. The gas chromatograph was down for maintenance and not available for these experiments.

3.1.2.1 Analysis of organic aerosol volatility

Volatility data were collected for several experiments after the SOA had formed and UV lights had been turned off. Thermodenuder (TD) data were analyzed in terms of Mass Fraction Remaining (MFR) after heating and vaporization in the thermodenuder. Using the total organic mass concentration from the ACSM, the MFR was calculated by dividing the mass concentration of the denuded OA by the mass concentration of the OA that had passed through the bypass. These data are presented in the form of a thermogram, which shows the MFR as a function of temperature in the TD. Considering that there was no inorganic nitrate added in these experiments, the “nitrate” measured by the ACSM is presumed to be due to organic nitrates and added to the organics measured by the ACSM for this analysis.

Particle concentrations decline in the smog chamber after SOA formation chemistry ceases due to losses to the chamber walls. This can lead to biases in the estimated MFR when bypass concentrations before or after the TD sampling period are used. A more accurate MFR was

obtained by interpolation of the bypass OA concentrations corresponding to the TD sampling times.

Particle losses in the TD were also taken into account. These losses occur due to diffusion (primarily of small particles), sedimentation (primarily of large particles), and thermophoresis; the losses can therefore be a function of sample flow rate, temperature, and particle size (Burtscher et al., 2001). All experiments in this project used the same flow rate at 1 liter per minute (LPM). Furthermore, previous characterization of number losses in the thermodenuder suggested that loss rates are not a strong function of particle size above ~ 80 nm particle diameter (Huffman et al., 2008; Wehner et al., 2002). Volumetric average bypass particle diameters were greater than 200nm for all TD experiment conducted. Thus, in this work we assume that particle loss rates are independent of size. Temperature-dependent particle loss was characterized using lab-generated NaCl aerosol, which is expected to be non-volatile over the temperature range tested (25~200 °C). The organic MFR was thus calculated using the following equation,

$$MFR = \frac{C_{OA,TD} + C_{NO_3,TD}}{C_{OA,Bypass} + C_{NO_3,Bypass}} \frac{1}{1 - f_N} \quad (4)$$

where $C_{OA,TD}$, $C_{NO_3,TD}$, $C_{OA,Bypass}$, $C_{NO_3,Bypass}$ are ACSM bypass and thermodenuder mass concentrations for organics and nitrate, respectively, averaged over 10-15 minutes for a given TD temperature. The expected particle number loss f_N was converted to and applied as a volume loss correction factor. Considering that these data were collected when the UV lights were turned off (so no photochemical reactions were occurring in the chamber), it is reasonable to assume that the composition and volatility over these averaging periods was not changing.

Due to the non-equilibrium conditions in the TD, a dynamic mass transfer model developed by Riipinen et al. (2010) was used to estimate the relative volatility of the OA formed in the experiments (Expt.) outlined in Table 4. Briefly, aerosol evaporation is simulated using experimental inputs including the thermogram (MFR vs TD temperature), TD residence time, TD length, particle mode diameter, mass concentration, and OA density. Model inputs are summarized in Table 3.

Table 3. Inputs to mass transfer model

	Expt. 1 n-Pentadecane	Expt. 6 TMD	Expt. 15 Mineral Spirits
Residence Time * (s)	15.7	15.7	15.7
Heating Length * (m)	0.57	0.57	0.57
OA Density † (µg/cm ³)	1.40	1.40	1.40
Avg. Bypass Dp ‡ (nm)	448.9	247.4	508.7
Avg. Bypass Mass ‡ (µg/m ³)	53.7	67.6	42.2

(*) TD characterization data; (†) Assumed; (‡) Measured

The model discretizes and investigates the entire possible solution space, as outlined in Table 4, to calculate the expected thermograms, where x_i is the fractional mass contribution of aerosols with effective saturation concentration C_i^* (discretized at $\Delta x_i=0.1$). This method utilizes the volatility basis set (VBS) approach (Donahue et al., 2006) to account for the component complexity in the SOA formed. The following bins set was used

$$\{C_i^*\} = \{0.01; 0.1; 1; 10\} \mu g / m^3$$

As described in Karnezi et al. (2014), the percentage error between expected and experimental MFR is calculated as:

$$E_i = \frac{100}{n} \sqrt{\sum_i^n (MFR_{i,guess} - MFR_i)^2} \quad (5)$$

where $MFR_{i,guess}$ is the MFR for a certain combination of parameters for data point i (corresponding to a specific temperature), MFR_i is the “measured” MFR, and n is the number of the different temperatures used in our measurements. Results with error below a set threshold are then used to compute a weighted average (\bar{x}) of each parameter, using the inverse error as the weighting factor:

$$\bar{x} = \frac{\sum_i^N \left[(x_i) \cdot \left(\frac{1}{E_i} \right) \right]}{\sum_i^N \left[\frac{1}{E_i} \right]} \quad (6)$$

The uncertainty is then calculated as the standard deviation (σ) of each parameter:

$$\sigma = \sqrt{\frac{\sum_i^N \left[(x_i - \bar{x})^2 \cdot \left(\frac{1}{E_i} \right) \right]}{\sum_i^N \left[\frac{1}{E_i} \right]}} \quad (7)$$

Table 4. Solution space used by mass transfer model

	Min	Max	# of Solutions
x_i	0	1	275
α	0.01	1	8
ΔH_{vap}	10 kJ/mol	200 kJ/mol	9

3.2 Experimental Results

3.2.1 Formation of SOA

A total of 16 environmental chamber experiments were conducted to form SOA from the oxidation of IVOCs listed in Table 1. Experimental conditions of these experiments are summarized in Table 5; all experiments were conducted at low relative humidity (< 5% RH) and at room temperature (~ 25°C). The dependence of SOA formation on relative humidity can be important, has not been studied systematically, and should be the focus of future work.

Table 5. Experimental conditions for all experiments conducted

Expt.	IVOC	Oxidant	NO _x	[IVOC] ₀ ($\mu\text{g m}^{-3}$)
1	n-pentadecane	HONO	High	190
2	n-pentadecane,	H ₂ O ₂	Low	350
3	TMD	H ₂ O ₂	Low	130
4	TMD	H ₂ O ₂	High	250
5	TMD	HONO	High	190
6	TMD	HONO	High	190
7	butyl CARBITOL™	H ₂ O ₂	Low	160
8	butyl CARBITOL™	HONO	High	240
9	Texanol™	HONO	High	140
10	Texanol™	O ₃ + H ₂ O ₂	Low	310
11	Texanol™	HONO + Cl	High	340
12	Mineral Spirits	H ₂ O ₂	Low	730*
13	Mineral Spirits	HONO	High	730*
14	Mineral Spirits	HONO	High	2700*
15	Mineral Spirits	HONO	High	2700*
16	2-MN	HONO	High	120

* assuming all compounds in the mixture have the molecular weight of decane

With the exception of TexanolTM, all IVOCs studied formed a significant amount of SOA upon photo-oxidation by the hydroxyl radical under high NO_x conditions. For example, Figure 6 shows the time series of organic aerosol formed during Experiments 1 and 5 which utilized HONO as an OH radical precursor to oxidize n-pentadecane and 2,6,10-trimethyldodecane (a branched pentadecane), respectively. It is clear that these IVOCs form a significant amount of organic aerosol upon oxidation, consistent with previous work (Aimanant and Ziemann, 2013; Lim and Ziemann, 2009; Presto et al., 2010; Tkacik et al., 2012).

Figure 7 shows the time series of organic aerosol formed during Experiment 15, which utilized HONO as an OH radical precursor to oxidize mineral spirits. The quantification of SOA yields from mineral spirits is only possible if the exact composition of mineral spirits is known and that information was unavailable to us. Nevertheless, our data indicate that the oxidation of mineral spirits forms a large amount of organic aerosol which could significantly affect air quality in Texas and other regions. The composition of mineral spirits and their SOA yields should be quantified in a future study so that the OA formation from this source can be accounted for in chemical transport models.

A drift in the calibration of the scanning electrical mobility system (SEMS) interfered with our ability to quantify the amount of particulate matter formed, and therefore the organic aerosol mass yield, in experiments 1 through 7. In experiments 9, 10 and 11 (using TexanolTM as IVOC precursor) no organic aerosol was formed, and in experiments 12 – 15 (mineral spirits) the organic aerosol mass yield cannot be quantified because the complex mix of mineral spirits components is unknown. This leaves us only with experiments 8 and 16 to quantify organic aerosol mass yields; the other experiments still provide useful qualitative data (for example, whether organic aerosol forms from the oxidation of that precursor). Figure 8 below shows the organic aerosol mass yield from butyl CARBITOLTM (Expt. 8) and 2-methylnaphthalene (Expt. 16) as well as the OA mass yields of n-pentadecane and 2-methylnaphthalene from previous work. The SOA mass yield of 2-methylnaphthalene determined in this work are consistent with the yields from previous work, suggesting that our experimental and analysis procedures are appropriate. Our data further indicate that the formation of organic aerosol from butyl CARBITOLTM is significant and comparable to other known, non-oxidized IVOC precursors. Butyl CARBITOLTM is an important constituent in paint and similar. According to our analysis of the point source emissions inventory discussed in Section 2.0 above the emissions of Butyl CARBITOLTM are high and important to Texas air quality. The SOA formation from this species should therefore be represented in chemical transport models. Our research group is currently conducting additional experiments to further investigate SOA formation from this precursor.

During experiments using TexanolTM as an IVOC precursor organic aerosol concentrations remained below the detection limit of the ACSM. It thus appears that the SOA formation from TexanolTM is insignificant under ambient conditions and does not need to be represented in chemical transport models.

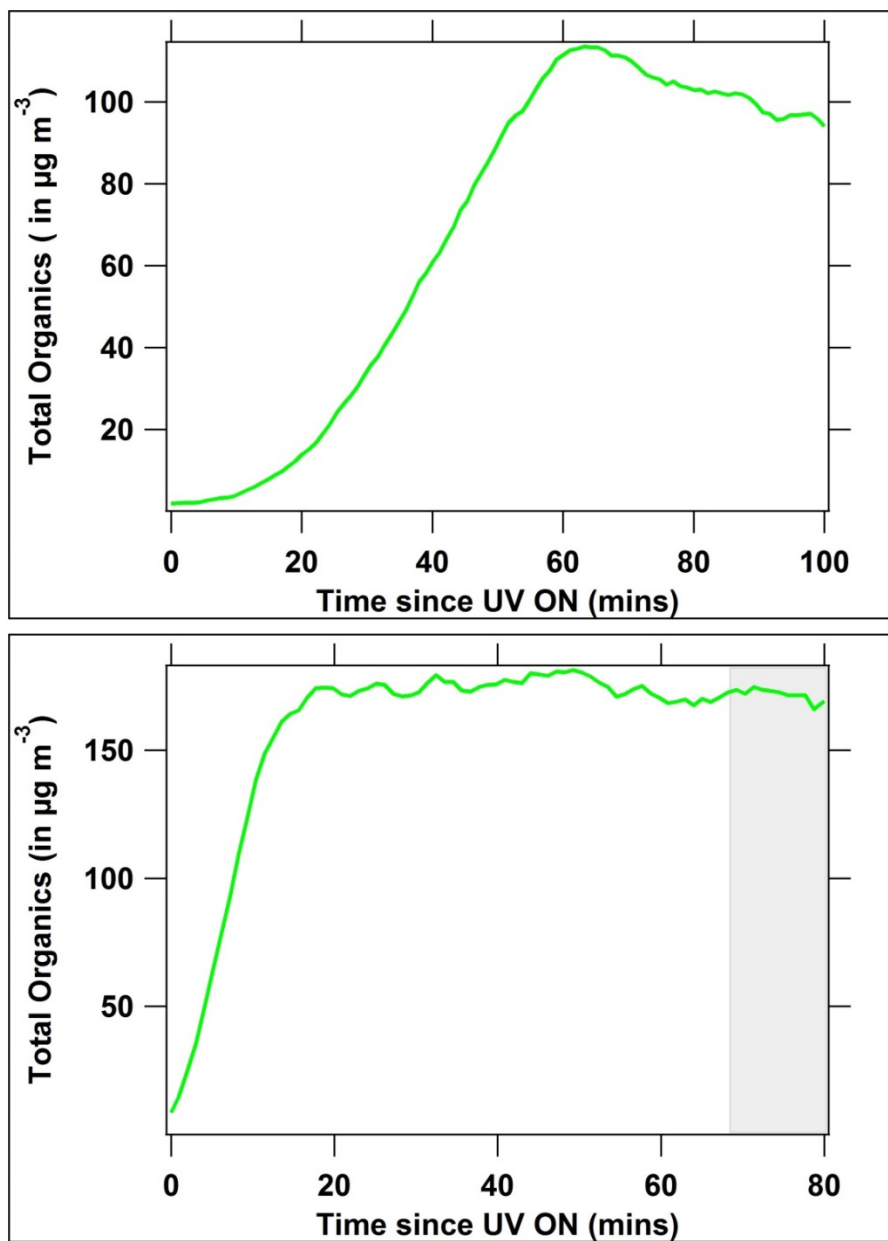


Figure 6. Organic aerosol formed from the photo-oxidation of n-pentadecane (top panel : Expt. 1) and 2,6,10-trimethyldodecane (bottom panel : Expt. 5).

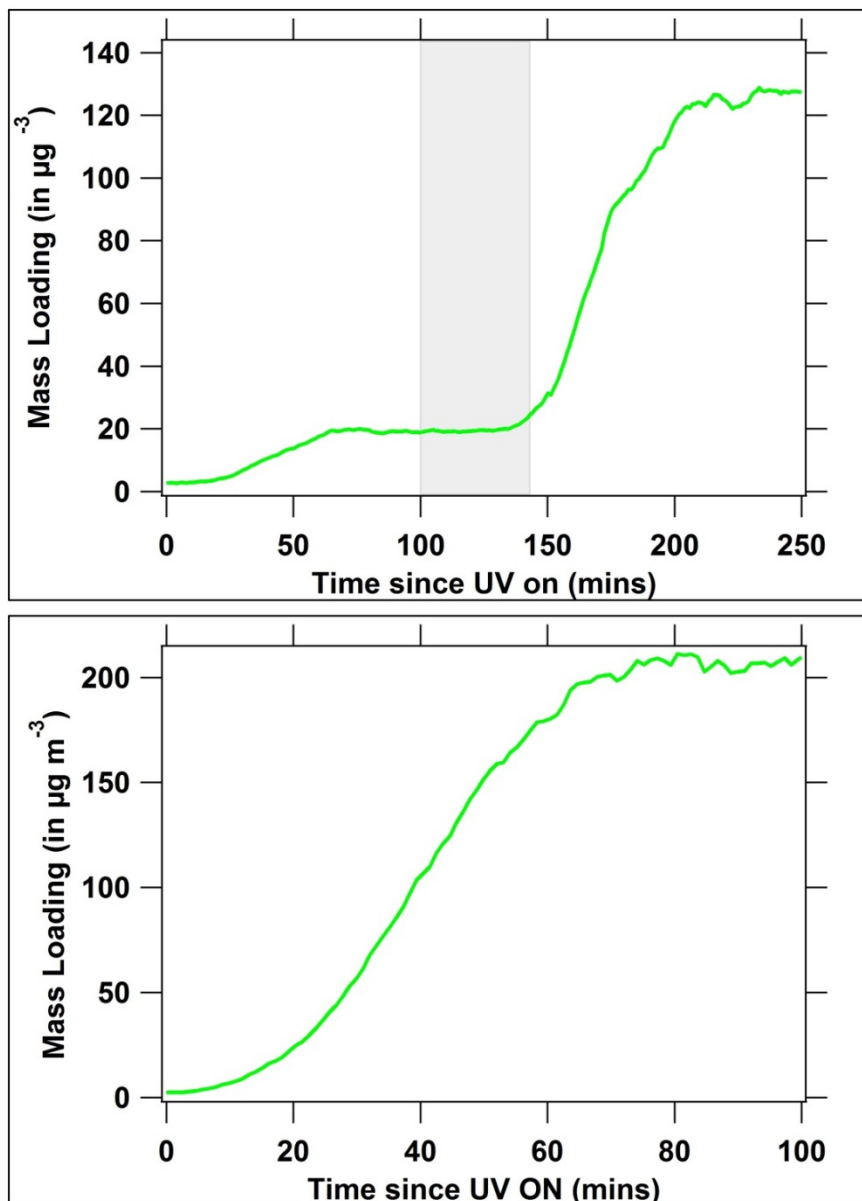


Figure 7. Organic aerosol formed from the photo-oxidation of mineral spirits (Top : Expt. 15; Bottom : Expt. 14). The grey shaded portion in the top panel represents time when UV lights were switched off and additional HONO and mineral spirits were injected.

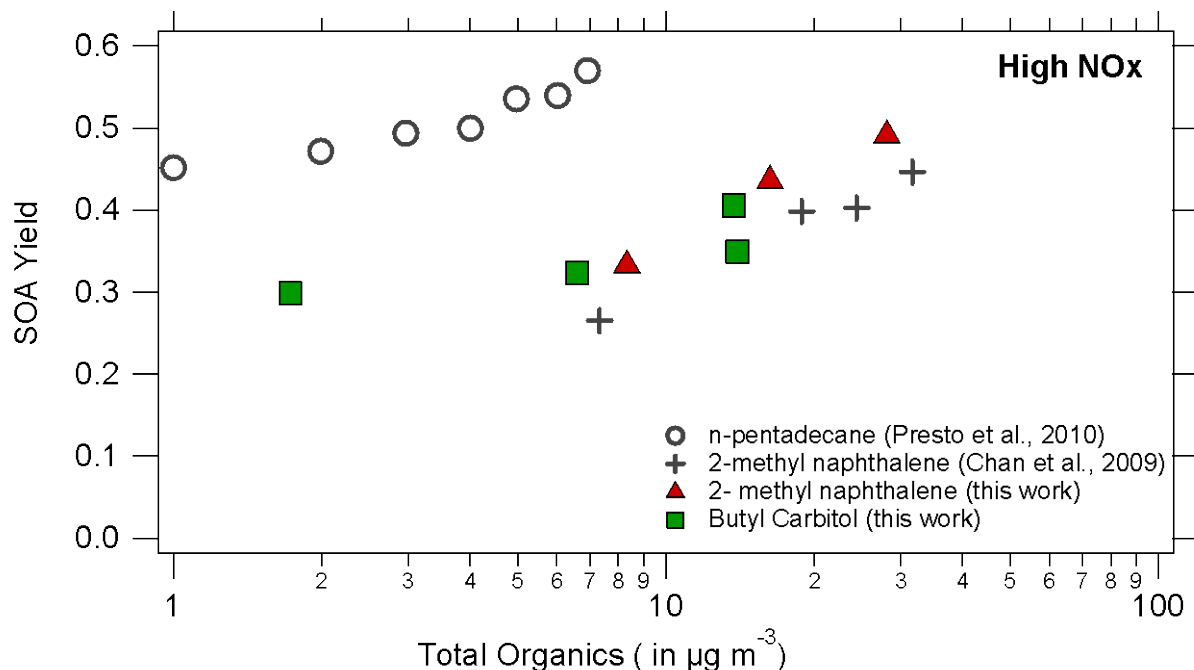


Figure 8. Organic aerosol mass yields from this and previous work.

3.2.2 Composition of SOA

In addition to the total (PM_{10}) organic aerosol mass, the ACSM also provides a measure of the total mass spectrum from which the organic mass spectrum is derived. The mass fragments at m/z 44 mostly correspond to the CO_2^+ ion (Aiken et al., 2008) and can therefore be used as a semi-empirical measure of the extent of oxidation in the system. The fragments at m/z 43 are thought to mostly correspond to the $C_2H_3O^+$ ion, a singly oxidized species. The fraction of organic mass at m/z 43 and m/z 44, $f_{43} = [m/z\ 43] (\mu g\ m^{-3}) / C_{OA} (\mu g\ m^{-3})$ and $f_{44} = [m/z\ 44] (\mu g\ m^{-3}) / C_{OA} (\mu g\ m^{-3})$, where C_{OA} is the total mass concentration of the organic aerosol, can therefore be used to represent moderately oxidized and strongly oxidized organic aerosol, respectively (Ng et al., 2010). Ng et al. (2010) found that the composition of ambient organic aerosol falls within a triangular region on a plot of f_{44} versus f_{43} .

Figure 9 plots f_{44} versus f_{43} of the organic aerosol formed during the experiments listed in Table 5, excluding experiments 9-11 (TexanolTM) in which organic aerosol concentrations remained below the detection limit. The figure also shows the triangular region identified by Ng et al. (2010) typical of ambient organic aerosol. Blue symbols indicate data from low NO_x experiments and red symbols indicate data from high NO_x experiments. The data suggest that the composition of the secondary organic aerosol formed in these experiments is consistent with organic aerosol observed in the atmosphere. In addition, the SOA formed in high NO_x experiments was generally more oxidized than SOA formed in low NO_x experiments. This could be related to the higher OH concentrations achieved when using HONO as an OH precursor compared to the OH

concentrations achieved when using H₂O₂ as a precursor. Furthermore, the SOA formed from butyl CARBITOLTM was the most oxidized SOA (for both high and low NO_x conditions), consistent with the fact that the precursor molecule (butyl CARBITOLTM) is already oxidized.

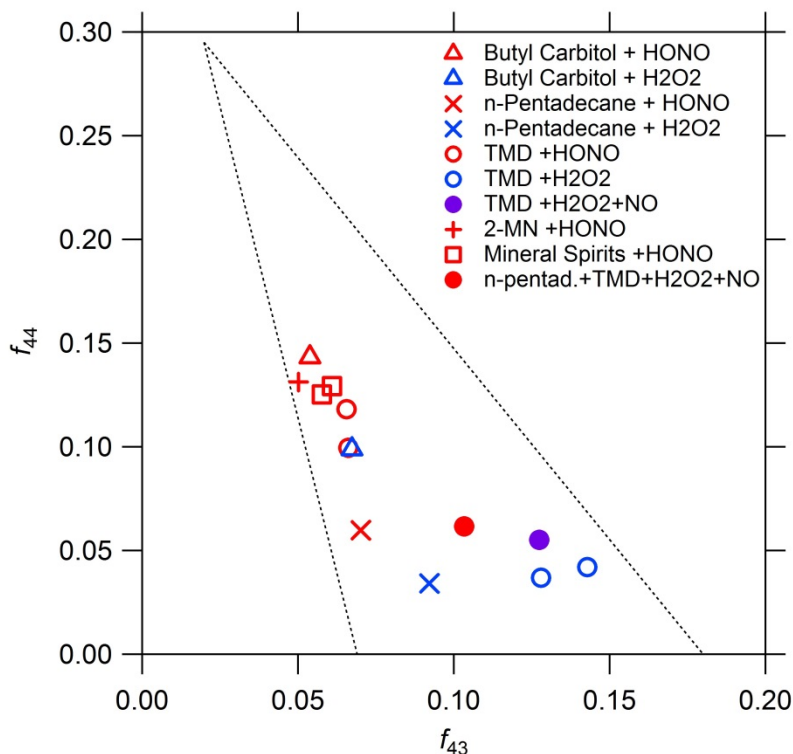


Figure 9. Summary of organic aerosol composition, represented as f_{43} and f_{44} , from all experiments

3.2.3 Volatility (VBS parameters) of SOA

In order to quantify the volatility of the organic aerosol formed, the MFR data were modeled in a mass transfer model as described in section 3.1.2.1. The resulting thermogram of organic aerosol formed in experiments 1, 6 and 15 is shown in Figure 10. The data have been corrected for number losses as described in section 3.1.2.1. The organic aerosol formed from the oxidation of IVOCs is semivolatile – on average, at temperatures between 69.9 to 93.5°C, half of the organic aerosol evaporates in the thermodenuder. Equilibrium partitioning of organic aerosol is therefore consistent with our data.

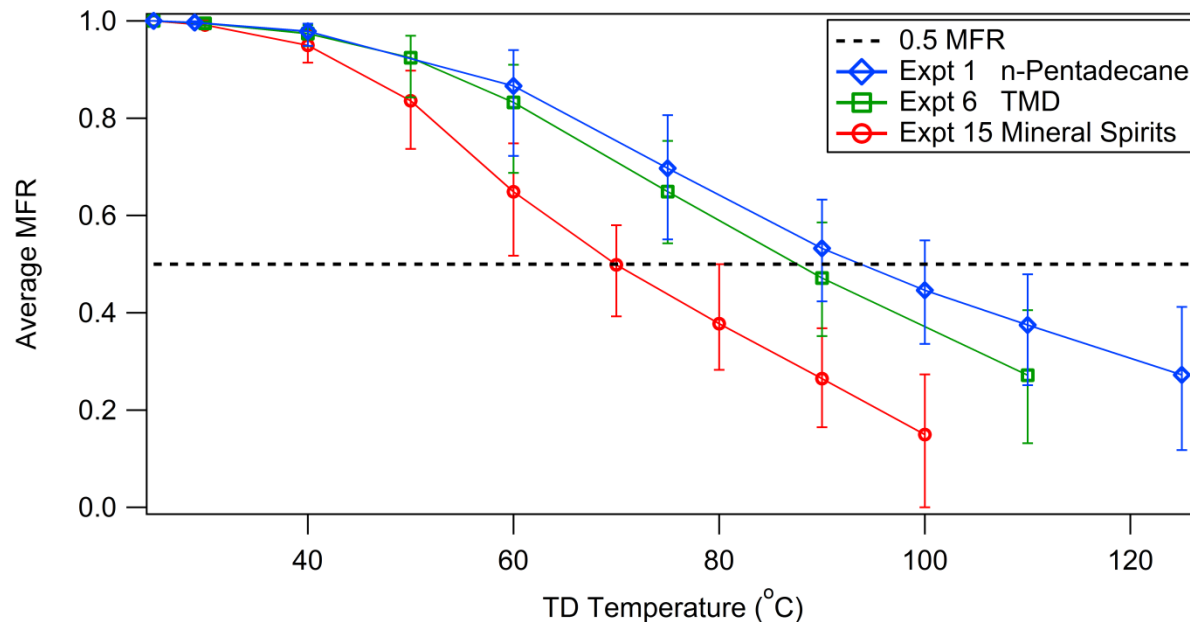


Figure 10. Thermogram of SOA generated. Profiles for n-pentadecane and TMD are within range of calculated uncertainty.

As seen in Figure 10, SOA generated from n-pentadecane and branched pentadecane exhibit similar volatility, as well as similar effective enthalpy of vaporization, accommodation coefficient, and volatility distribution, as shown in Figures 10, 11 and 12, respectively. Both forms of pentadecane lead to formation of SOA that is less volatile than SOA formed from mineral spirits. Evaporation model input and results are summarized in Table 6.

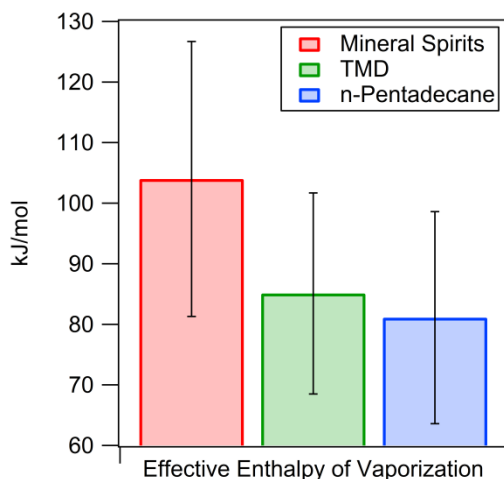


Figure 11. Effective enthalpy of vaporization of SOA formed from IVOC oxidation

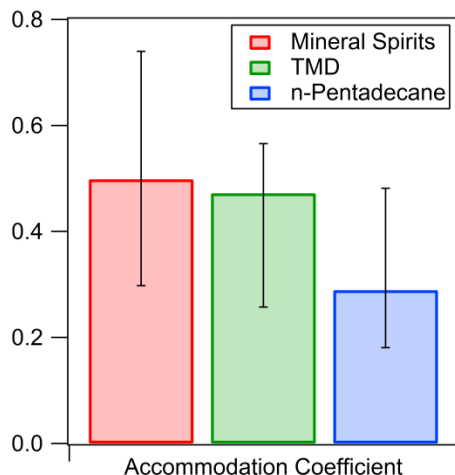


Figure 12. Accommodation coefficient of SOA formed from IVOC oxidation

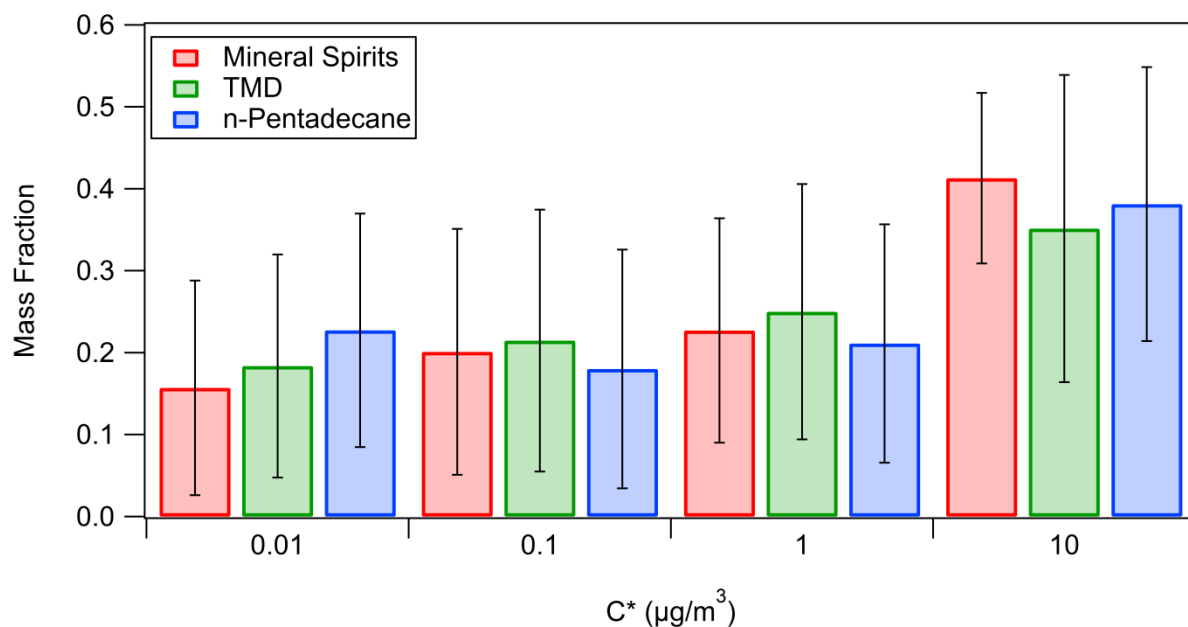


Figure 13. Volatility distribution of SOA formed from the oxidation of mineral spirits, n-pentadecane, and branched pentadecane. SOA formed from pentadecane is less volatile than SOA formed from mineral spirits.

Table 6. Evaporation model inputs and results

	Expt 1 n-Pentadecane	Expt 6 TMD	Expt 15 Mineral Spirits
x ($C^* = 10^{-2} \mu\text{g}/\text{m}^3$)	0.227 ± 0.142	0.184 ± 0.136	0.157 ± 0.131
x ($C^* = 10^{-1} \mu\text{g}/\text{m}^3$)	0.180 ± 0.146	0.215 ± 0.160	0.201 ± 0.150
x ($C^* = 10^0 \mu\text{g}/\text{m}^3$)	0.211 ± 0.145	0.250 ± 0.156	0.227 ± 0.137
x ($C^* = 10^1 \mu\text{g}/\text{m}^3$)	0.381 ± 0.167	0.352 ± 0.187	0.413 ± 0.104
Avg. Accom. Coeff.	0.181 ~ 0.481	0.257 ~ 0.566	0.298 ~ 0.740
$\Delta H_{\text{vap,avg}}$ (kJ/mol)	81.1 ± 17.5	85.1 ± 16.6	104.0 ± 22.7
50% MFR Temp. ($^{\circ}\text{C}$)	81 ~ 107	78.4 ~ 99.5	61.4 ~ 80.0

4.0 Chemical Mechanism

In this study, three classes of IVOC were added to represent SOA precursors from major combustion sources (gasoline and diesel engines and biomass burning) that are not typically accounted in the current emissions inventory, based on recent smog chamber data (Jathar et al., 2014). Estimation of the IVOC emissions is described in Section 5.

The VBS scheme requires aerosol yields of SOA precursors for each volatility bin. Following the assessment of Jathar et al. (2014), IVOC from diesel engines is represented by C15 n-alkane (n-pentadecane), and IVOC from gasoline engines by C13 n-alkane (n-tridecane). IVOC from biomass burning is represented by C15 n-alkane. Table 7 lists IVOC species and their SOA mass yields.

Table 7. SOA surrogates and VBS SOA mass yields used for IVOCs (Jathar et al., 2014).

IVOC species	SOA surrogate	C^* ($\mu\text{g m}^{-3}$)			
		0	1	10	100
IVOD (from on- and off-road diesel engines)	n-pentadecane	0.044	0.071	0.41	0.30
IVOG (from on- and off-road gasoline engines)	n-tridecane	0.014	0.059	0.22	0.40
IVOB (from biomass burning)	n-pentadecane	0.044	0.071	0.41	0.30

The rate constant for IVOC oxidation via gas-phase OH reaction is assumed to be $4 \times 10^{-11} \text{ cm}^3 \text{ molec}^{-1} \text{ sec}^{-1}$ (at 298K, Robinson et al., 2007). C^* is the saturation mass concentration (see Donahue et al., 2006).

5.0 Photochemical Modeling

The latest version of CAMx (CAMx V6.20; ENVIRON, 2015) was applied to simulate OA formation in the Houston region during the DISCOVER-AQ campaign (August-September 2013). Carbon-Bond 6 Revision 2 (CB6r2; Hildebrandt Ruiz and Yarwood, 2013) was selected for the gas-phase chemistry mechanism and 1.5-D VBS scheme (Koo et al., 2014) was used to model primary and secondary OA in the atmosphere. The VBS scheme uses 4 separate basis sets to differentiate fossil (anthropogenic) from modern (biogenic) carbon as well as SOA or aged POA from fresh emissions. Source-specific volatility distribution factors are applied for POA emissions from gasoline and diesel vehicles, other anthropogenic sources, and biomass burning. Table 8 lists the model OA species and their molecular properties.

Table 8. Molecular properties of the 1.5-D VBS species (Koo et al., 2014)

Basis Set	Model Species Name ^a	C* ^b ($\mu\text{g m}^{-3}$)	$\overline{\text{OS}}_c$ ^c	C # ^e	O # ^f	MW (g mole^{-1})	OA/OC
OOA	PAS0 & PBS0	0 ^d	0.102	7	4.90	172	2.05
	PAS1 & PBS1	1	-0.188	7.25	4.38	167	1.92
	PAS2 & PBS2	10	-0.463	7.5	3.84	163	1.81
	PAS3 & PBS3	100	-0.724	7.75	3.30	158	1.70
	PAS4 & PBS4	1000	-0.973	8	2.74	153	1.59
HOA	PAP0	0 ^d	-1.52	17	2.69	278	1.36
	PAP1	1	-1.65	17.5	2.02	275	1.31
	PAP2	10	-1.78	18	1.34	272	1.26
	PAP3	100	-1.90	18.5	0.632	268	1.21
	PAP4	1000	-2.00	19	0.0	266	1.17
BBOA	PFP0	0 ^d	-0.704	10	4.32	205	1.71
	PFP1	1	-1.02	11	3.60	208	1.58
	PFP2	10	-1.29	12	2.85	211	1.47
	PFP3	100	-1.52	13	2.08	213	1.37
	PFP4	1000	-1.73	14	1.27	215	1.28

^a The model VBS species name consists of 4 characters that indicate sequentially the phase (P – particle; V – vapor), the source (A – anthropogenic; B – biogenic; F – fire), the formation (P – primary; S – secondary), and the volatility bin number (0 to 4).

^b Effective saturation concentration.

^c Average oxidation state of carbon.

^d Properties of the lowest volatility bins were estimated assuming $C^* = 0.1 \mu\text{g m}^{-3}$, but they actually represent all OA with $C^* \leq 0.1 \mu\text{g m}^{-3}$, and are treated as non-volatile in the model.

^e average number of carbon atoms per molecule

^f average number of oxygen atoms per molecule

The CAMx domain consists of a 36-km continental-scale grid and a nested 12-km grid that covers entire Texas and a 4-km nested grid covering the Houston area (Figure 14).



Figure 14. CAMx modeling domain with outer 36 km grid and nest 12 km (blue) and 4 km (green) grids

CAMx meteorological inputs for this application were developed using version 3.6.1 of the Weather Research Forecast (WRF; Skamarock et al., 2008) meteorological model released August 14, 2014. The WRF model was run for the 2013 DISCOVER-AQ period in a configuration developed for a previous Texas modeling application. The model was run from August 16 to September 30, 2013 with the first 8 days (August 16-23) being spin-up days in order to match the measurement period at the Conroe ground site (August 24 to September 30). A summary of the WRF model configuration is provided in Table 9. The model was run as a series of independent 5-day simulations which were started before the DISCOVER-AQ period, on August 15, 2013, in order to provide CAMx with meteorological inputs for a 2-week spinup period. We turned on the Kain-Fritsch cumulus parameterization (K-F; Kain, 2004) for the 36 and 12 km domains and turned the scheme off for the Houston 4 km domain, as suggested by WRF developers for domains with horizontal resolutions finer than around 10 km (Skamarock et al., 2008). We prepared the WRF meteorological fields for CAMx using the WRFCAMx program. We made several enhancements to the WRF meteorological fields. First, we applied the Yonsei University vertical diffusivity (YSU Kv) methodology within WRFCAMx in order to promote consistency between the WRF and CAMx models. Next, we enhanced sub-grid

cloudiness for all domains using a diagnosis of thermodynamic properties similar to that used by the CMAQ model. Finally, we applied patches to the vertical diffusivity fields in order to enhance nighttime mixing in urban areas (commonly called the “Kv100” patch) and mixing below convective clouds (the “Kv cloud” patch).

Table 9. Physics options used in the WRF simulation of the August-September, 2013 modeling period

WRF Treatment	Option Selected	Notes
Microphysics	WRF Single Moment -6 (WSM-6)	A simple efficient scheme with ice and snow processes suitable for mesoscale grid sizes.
Longwave Radiation	Rapid Radiative Transfer Model for GCMs (RRTMG)	RRTMG includes random cloud overlap and improved efficiency over RRTM.
Shortwave Radiation	RRTMG	Same as above, but for shortwave radiation.
Surface Layer Physics	5 th generation Pennsylvania State University / National Center for Atmospheric Research Mesoscale Model (MM5) similarity	
Land Surface Model (LSM)	Noah	Two-layer scheme with vegetation and sub-grid tiling.
Planetary Boundary Layer (PBL) scheme	Yonsei University (YSU)	YSU (Korea) Asymmetric Convective Model with non-local upward mixing and local downward mixing.
Cumulus parameterization	Kain-Fritsch in the 36 km and 12 km domains. None in the 4 km domain.	4 km is assumed to explicitly simulate cumulus convection, so parameterization is not typically used.
Analysis nudging	Nudging applied to winds, temperature and moisture in the 36 km and 12 km domains	Temperature and moisture nudged above PBL only
Observation Nudging	None	
Initialization Dataset	12 km North American Model (NAM)	
Kain-Fritsch RRTMG Interaction	Turned on for 36/12 km domains (only applicable for domains with cumulus parameterization)	Subgrid cloud information fed back to radiation scheme (Alapaty et al., 2012)

Anthropogenic emissions were provided by TCEQ in CAMx-ready format for the 36/12/4 km domains compatible with CB6 mechanism. Elevated point source emissions include day-specific Continuous Emissions Monitoring (CEM) data made available by the Acid Rain Program for the

September 2013 modeling period. Surface emissions including area, mobile, and low-point sources are from TCEQ's 2012 day-of-week specific emissions inventory. TCEQ's anthropogenic emissions include PM precursors (e.g., sulfur dioxide and ammonia) and primary fine PM emissions. Emissions of coarse PM are not included.

The inventory of biogenic emissions was generated using the Model of Emissions of Gases and Aerosols from Nature (MEGAN) version 2.1 (Guenther et al., 2012), the same model used in TCEQ's SIP modeling. MEGAN driving variables include weather data, Leaf Area Index (LAI), plant functional type (PFT) cover and compound-specific emission factors (EF) that are based on plant species composition. TCEQ provided the LAI data for the 36/12/4 km domains. ArcGIS software was applied to generate MEGAN PFT/EF input files. The MEGAN model was applied using the daily meteorology (temperature and solar radiation) from the WRF model outputs to generate day-specific biogenic emissions for the 36/12/4 km domains. Recent modeling studies conducted by ENVIRON suggest that the MEGAN biogenic emissions model may be generating excessive isoprene emissions (ENVIRON and ERG, 2013). To mitigate this issue, we reduced MEGAN isoprene by a factor of two following an improvement introduced for Near Real-Time ozone modeling (Johnson et al., 2013).

Fire emissions were based on the Fire Inventory from NCAR (FINN) version 1 dataset, downloadable from <http://bai.acd.ucar.edu/Data/fire/>. The global dataset contains daily emissions for each satellite pixel, an area of approximately 1 km². Emission species include NO, NO₂, PM_{2.5}, CO, and non-methane organic gas (NMOG). Fire points within 5 km of one another are assumed to be part of the same fire and assigned properties of a larger fire. The daily fire emissions were processed for the September 2013 modeling period using an updated version of EPS3 version 3.20. EPS3 incorporates the Western Regional Air Partnership (WRAP) methodology to temporally and vertically allocate the fire emissions.

Emissions of sea-salt particles including sodium, chloride, and sulfate, depend upon wind speed and were estimated using the 2013 WRF hourly, gridded meteorology. The sea salt aerosol fluxes from both open oceans (Smith and Harrison 1998; Gong, 2003) and breaking waves in the surf zone (de Leeuw et al., 2000) are a function of wind speed at 10 meter height.

IVOC emissions for the base case simulation were estimated based on the source-specific emissions inventory data provided by TCEQ and unspciated fractions of total NMOG emissions estimated by Jathar et al. (2014). Table 10 shows NMOG fractions of 3 different combustion source types (gasoline, diesel, and biomass burning) by source sector. These fractions were estimated based on the TCEQ inventory data of the 8 HGB-area counties.

Table 10. Fractions of NMOG emissions by combustion source type

	Onroad	Nonroad	Offroad	Area	Oil & Gas	Fires^a	Unspeciated fraction^b
Gasoline	88.6%	80.9%	1.7%	-	-	-	25%
Diesel	11.4%	10.1%	40.8%	-	-	-	20%
Biomass burning	-	-	-	1.9%	-	100%	20%

^a Open burning emission based on NCAR's fire inventory data (FINN)

^b Unspeciated fraction of NMOG emission (Jathar et al., 2014)

Unspeciated NMOG emissions for these combustion sources were assumed to be IVOC emissions. Since the current speciation profiles were normalized to the sum of the speciated compounds rather than the total NMOG emissions in order to include all of the organic mass in the model, the updated emissions renormalized the speciation profiles to account for unspeciated organics, resulting reduced emissions of speciated organics (Jathar et al., 2014). Note that NMOG emissions of the area and oil & gas (O&G) sectors are predominantly from fugitive or natural gas combustion sources, which we didn't include in our IVOC estimation due to lack of data. Sensitivity tests to assess impact of IVOC emissions for these sources are recommended. Figure 15 compares the current vs. updated emissions of the traditional VOC precursors (toluene, xylene, benzene, isoprene, and monoterpenes) and IVOC for the 4-km Houston modeling domain.

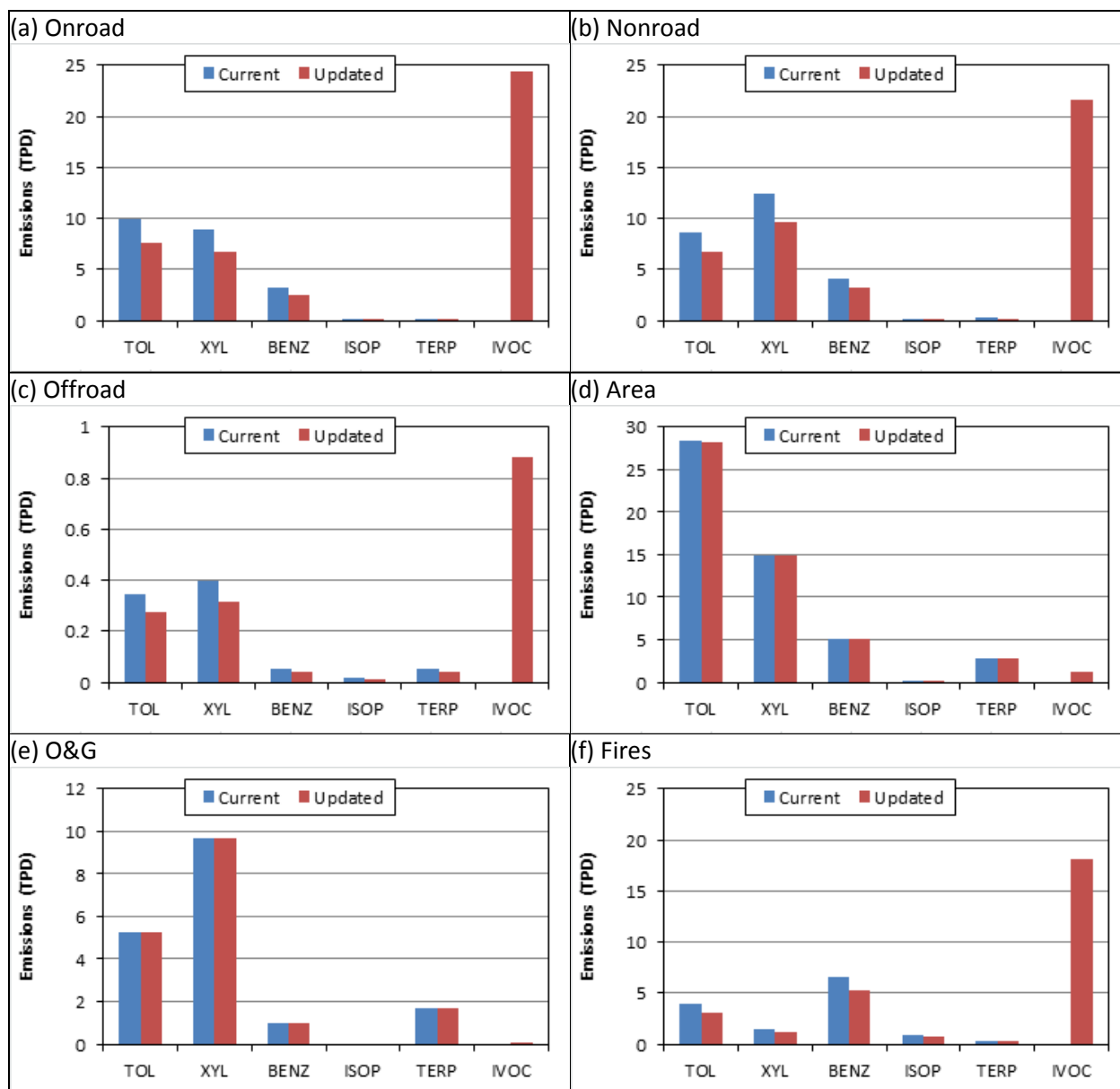


Figure 15. Daily total emissions in the 4-km modeling domain (averaged over September)

6.0 DISCOVER-AQ Data Analysis

6.1 Description of Site Location and Instrumentation

Data on concentrations and composition of gas and particle-phase species were taken during the DISCOVER-AQ 2013 campaign (Deriving Information on Surface Conditions from Column and Vertically Resolved Observations Relevant to Air Quality, <http://discover-aq.larc.nasa.gov/>) in Houston, TX for the period of September 1, 2013 – October 1, 2013. The data was obtained at

an air quality monitoring ground site in Conroe, TX (30.350278°N, 95.425000°W) situated next to the Lone Star Executive Airport in Montgomery county. The site is located approximately 60 km NNW from the Houston, TX urban center and approximately 125 km NW of the nearest coastline. The area surrounding Conroe, TX is primarily affected by pollution in the outflow of air from Houston, which hosts significant energy and petrochemical industries in addition to a large urban population. The regional atmospheric chemistry is also influenced by marine air from the Gulf of Mexico. The site itself is located in the middle of a field adjacent to the airport, with a gravel parking lot nearby and bordered by trees approximately 200 meters to the North.

A permanent Texas Commission on Environmental Quality (TCEQ) ambient measurement station exists at this site and provided continuous meteorological data for the duration of the campaign. Measured parameters included wind speed, wind direction, temperature and relative humidity. NO_x and O₃ monitors were also present at the TCEQ site. During DISCOVER-AQ a temporary ground site was set up adjacent to the permanent station. This temporary site housed an NO₂ monitor (Model AS32M from Environnement) which utilizes cavity attenuated phase shift spectroscopy (CAPS) to provide a direct absorption measurement of nitrogen dioxide (Kebabian et al., 2008). NO_x was measured using a chemiluminescence NO_x monitor (Teledyne Model 200E), and O₃ was measured by direct UV absorption (Teledyne, 400E). An Aerosol Chemical Speciation Monitor (ACSM, Aerodyne Research) (Ng et al., 2011) was used to measure the mass concentrations of non-refractory species in PM₁ (particulate matter smaller than 1 μm in diameter) including sulfate, nitrate, ammonium and organics. In the ACSM particles are flash vaporized at 600°C, and the resulting vapors are ionized using electron-impact ionization and then analyzed using a quadrupole mass spectrometer. A Scanning Electrical Mobility System (SEMS, Brechtel Manufacturing) was used to characterize particle size distributions and mass concentrations. A High Resolution Time-of-Flight Chemical Ionization Mass Spectrometer (HR-ToF-CIMS, Aerodyne Research) (Aljawhary et al., 2013; Bertram et al., 2011; Lee et al., 2014; Yatavelli et al., 2012) was employed to measure gas phase species. Daily PM_{2.5} filters were collected in collaboration with Drs. Sheesley and Usenko (AQR Project 14-029) using a TISCH Environmental high volume sampler (HV2.5). This report focuses on analysis of ACSM data since the project focus is on organic particulate matter.

6.2 ACSM Operation, Calibration and Data Work-up

The ACSM was set to scan between m/z 12 and 159 with a dwell time of 0.5, resulting in a scan time of 80 seconds. The instrument was set to alternate between sampling mode and filter mode, resulting in a cycle time of 160 seconds. Further averaging was performed in the post-analysis of the data. The vaporizer temperature was set at 600°C (as is standard) for fast vaporization of ammonium sulfate. The AMS measures only non-refractory (NR) PM₁, i.e. compounds that flash-vaporize at the heater temperature of 600°C. The collected data were analyzed using a

standard AMS fragmentation table and batch table (Allan et al., 2004), with a few modifications as detailed below.

The ACSM provides two measures of NR-PM₁ that are used in this analysis: the chemical composition and the total mass spectrum from which the organic mass spectrum is derived. The relative organic spectra are the contributions of the organic fragments at each m/z to the total organic mass. The mass fragments at m/z 44 mostly correspond to the CO₂⁺ ion (Aiken et al., 2008) and can therefore be used as a semi-empirical measure of the extent of oxidation in the system. Aiken et al. (2008) have shown that the fraction of organic mass at m/z 44, $f_{44} = [m/z\ 44] (\mu\text{g m}^{-3}) / C_{\text{OA}} (\mu\text{g m}^{-3})$, where C_{OA} is the total mass concentration of the organic aerosol, can be used to estimate the oxygen to carbon ratio (O:C) in the organic aerosol. They found significant correlation between O:C and f_{44} , which was recently updated by (Canagaratna et al., 2015) as:

$$(\text{O:C}) = 4.31 \times f_{44} + 0.079 \quad (8)$$

Aiken et al. (2008) also found a significant correlation between the ratio of organic mass to organic carbon (OM:OC) and O:C. This relationship was found to be applicable to field data as well as laboratory data and is described by:

$$(\text{OM:OC}) = 1.260 \times \text{O:C} + 1.180 \quad (9)$$

Thus, we can use the observed f_{44} to estimate O:C and OM:OC of the organic aerosol measured at Conroe.

The nitrate ionization efficiency (IE) of the ACSM, as well as the relative ionization efficiencies (RIEs) of sulfate and ammonium were measured twice at the beginning of the campaign (August 26 and 28) and twice after the campaign (September 9 and 28) using dried ammonium nitrate and ammonium sulfate particles with a diameter of 300 nm. The ratio of IE to the MS airbeam (AB) was constant for these calibrations (within noise), so the average IE/AB value of 3.29e-11 Hz⁻¹ was used for the whole campaign, and the IE was determined at any point by multiplying IE/AB by the current AB. The RIE of ammonium measured during the four IE calibrations (Aug. 26, 28 and Sept. 9 and 28) was 4.8, 4.9, 5.8 and 4.6, respectively, and the measured RIE of sulfate was 0.56, 0.67, 0.49 and 0.57. The variation in the values appeared random; therefore the average values of 5.0 and 0.57 were used for the entire campaign for ammonium and sulfate, respectively. The flow rate in the ACSM was 100 cm³ min⁻¹. Lens alignment and flow calibrations were performed at the beginning of the campaign.

6.2.1 Adjustments to standard fragmentation table

The fragmentation pattern of air at m/z 44 (CO₂⁺), m/z 29 (N¹⁵N⁺) and m/z 16 (O⁺) was evaluated using filter data which is collected continuously throughout the campaign. (The ACSM automatically alternates between passing the air through a particulate filter before analysis and measuring the full unfiltered air. Reported particulate concentrations are calculated by subtracting the concentrations in the filtered air from total concentrations.) N¹⁵N⁺ and CO₂⁺ were

calculated as constant fractions of the N_2^+ signal at m/z 28; the calculated fractions were $7.3\text{e-}3$ and $1.2\text{e-}3$ for N^{15}N^+ and CO_2^+ , respectively. O^+ was calculated as a constant fraction of N^+ ; the calculated ratio was 0.48. The correction for CO_2^+ from air using the N_2^+ signal was calculated by averaging the filter measurements throughout the campaign when particle-phase organics were below $1 \mu\text{g}/\text{m}^3$ – to avoid interference of organics being interpreted as CO_2^+ from air. The correction for N^{15}N^+ was calculated as an average of all filter data throughout the campaign.

Water dominates the signal in the background (filter) spectrum at m/z 16 (O^+) m/z 17 (OH^+) and m/z 18 (H_2O^+). The water fragmentation pattern can be determined by calculating the average ratio of m/z 16 / m/z 18 and m/z 17 / m/z 18 from the filter data. Using this method we determined that $\text{O}^+ = 26\%$ of H_2O^+ (different from 4% in the standard fragmentation table) and $\text{OH}^+ = 26.1\%$ of H_2O^+ (slightly different from the 25% in the standard fragmentation table).

Based on the recommendation by Aiken et al. (2008) and recent calibration experiments by Canagaratna et al. (2015) we used the following fragmentation pattern in relation to the m/z 44 signal: m/z 28 = 100%, m/z 18 = 100%. In the standard ACSM fragmentation table these ratios are set to 0% and 100%, respectively. This change in the fragmentation table increases the total organic signal, which was adjusted for as explained below.

6.2.2 Quantification, Data Averaging and Detection limits

For bulk composition analysis (organics, sulfate, ammonium, nitrate), every 10 data points were averaged, resulting in a time resolution of approximately 25 minutes (including 12.5 minutes of averaged sample and 12.5 minutes of averaged filter data), and 1607 data points throughout the campaign. (ACSM measurements were taken August 24 – September 30, 2013). The following detection limits were then calculated according to (Ng et al., 2011) and considering the 12.5 minutes sample averaging time: $0.440 \mu\text{g m}^{-3}$ (ammonium), $0.229 \mu\text{g m}^{-3}$ (organics), $0.037 \mu\text{g m}^{-3}$ (sulfate), $0.017 \mu\text{g m}^{-3}$ (nitrate). Application of the detection limits resulted in removal of 82% of the ammonium data, no removal of sulfate data, and removal of 1.2 and 0.6% of the data on organics and NO_3 , respectively. A 32 hour period in which the airbeam was abnormally high was also removed. When ammonium data were available, the mass ratio of ammonium to sulfate was 0.2807 on average, suggestive of acidic aerosol. Ammonium data were not available for most of the campaign due to low concentrations (and a relatively high detection limit) as reflected in the times series in Figure 16 below.

Quantification of aerosol concentrations measured by the ACSM is complicated by incomplete transmission of larger particles (>400 nm vacuum aerodynamic diameter) through the aerodynamic lens and particle bounce at the vaporizer. Use of the default collection efficiency of 0.5 (Middlebrook et al., 2012) resulted in good agreement with ancillary measurements. The updated fragmentation table results in a larger total organic signal than the default fragmentation table (since the organic signal at m/z 28 is set equal to the organic signal at m/z 44 instead of

equal to zero). The total organic concentration was adjusted for this difference before applying this default collection efficiency: $\text{Org_corr} = (\text{Org} * (1 - f_{44})) / 0.5$.

The f_{44} data were prepared as follows: first, every 5 data points were averaged. Then, datapoints for which $f_{44} < 0$ or $f_{44} > 1$ were removed since these are not physically possible. (20 data points were below zero, 10 data points were above 1). Then, every 5 data points were averaged again for an overall time resolution of approximately 1 hr. Then data were removed for which the signal of organics at m/z 44 (i.e. $f_{44} \times \text{org}$) was below the detection limit of organics for the 31.25 min averaging time. This resulted in removal of 13% of the final averaged data.

6.2.3 Diurnal patterns: analysis of statistical significance and characterization

We conducted one-way analysis of variance (ANOVA) tests for total bulk concentrations (organics, sulfate, and nitrate), f_{43} , f_{44} , and organic aerosol factors as dependent variables, and time of day as the independent variable. ANOVA tests determine whether there are statistically significant differences in the mean values of the dependent variables (Atkinson-Palombo et al., 2006). While ANOVA tests determine statistical significance of variation by time of day, they cannot quantify or characterize the diurnal cycle. Thus, we also conducted harmonic analysis (Atkinson-Palombo et al., 2006; Wilks, 1995) to characterize the diurnal cycle.

In brief, the general harmonic function is given by:

$$y_t = \bar{y} + C_k \cos(2\pi t/n - \phi_k) \quad (10)$$

where t is the time (1-24 in our diurnal analysis), \bar{y} is the mean of the time series (e.g. y_t is the mean value of f_{44} during hour t , \bar{y} is the mean value for the whole campaign), C_k is the amplitude of the k^{th} harmonic, n is the period ($n = 24$ here) and ϕ is the phase. Using only the first harmonic, we can estimate the amplitude (Atkinson-Palombo et al., 2006; Wilks, 1995) by

$$C_1 = [A_1^2 + B_1^2]^{1/2} \quad (11)$$

where

$$A_1 = 2/n \times \sum y_t \cos(2\pi t/n) \quad (12a)$$

$$B_1 = 2/n \times \sum y_t \sin(2\pi t/n) \quad (12b)$$

The phase is then given by:

$$\phi_1 = \tan^{-1}(B_1 / A_1) \pm \pi \quad \text{if } A_1 < 0 \quad (13a)$$

$$\phi_1 = \tan^{-1}(B_1 / A_1) \quad \text{if } A_1 > 0 \quad (13b)$$

$$\phi_1 = \pi / 2 \quad \text{if } A_1 = 0 \quad (13c)$$

The portion of the variance explained by the first harmonic, analogous to a correlation coefficient (R^2) commonly computed in regression analysis, is given by

$$V_1 = C_1^2 / 2s^2 \quad (14)$$

where s is the standard deviation of the n values.

The phase simply describes to what extent the observed cycle is offset from a standard cosine curve. The amplitude describes the magnitude of the diurnal cycle.

6.3 Organic Aerosol Concentrations and Composition

Figure 16 below shows time series of PM_{10} organics, ammonium, sulfate and nitrate measured by the ACSM throughout the campaign, as well as the campaign-average composition measured by the ACSM. Based on the mass spectral data, the “nitrate” measured by the ACSM (which is the sum of NO^+ and NO_2^+ fragments) was due to organic nitrates, not due to inorganic nitrate. This is consistent with analysis of inorganic composition from $PM_{2.5}$ filters, performed by the Desert Research Institute, which revealed very low concentrations of inorganic nitrate in $PM_{2.5}$. Thus, modeled organic aerosol concentrations should be compared to the sum of “organics” and nitrate” measured by the ACSM. On average 65% percent of the non-refractory PM_{10} mass was due to organic material (including organic nitrates) according to data from the ACSM, highlighting the importance of organics in controlling fine PM_{10} mass in the Houston region.

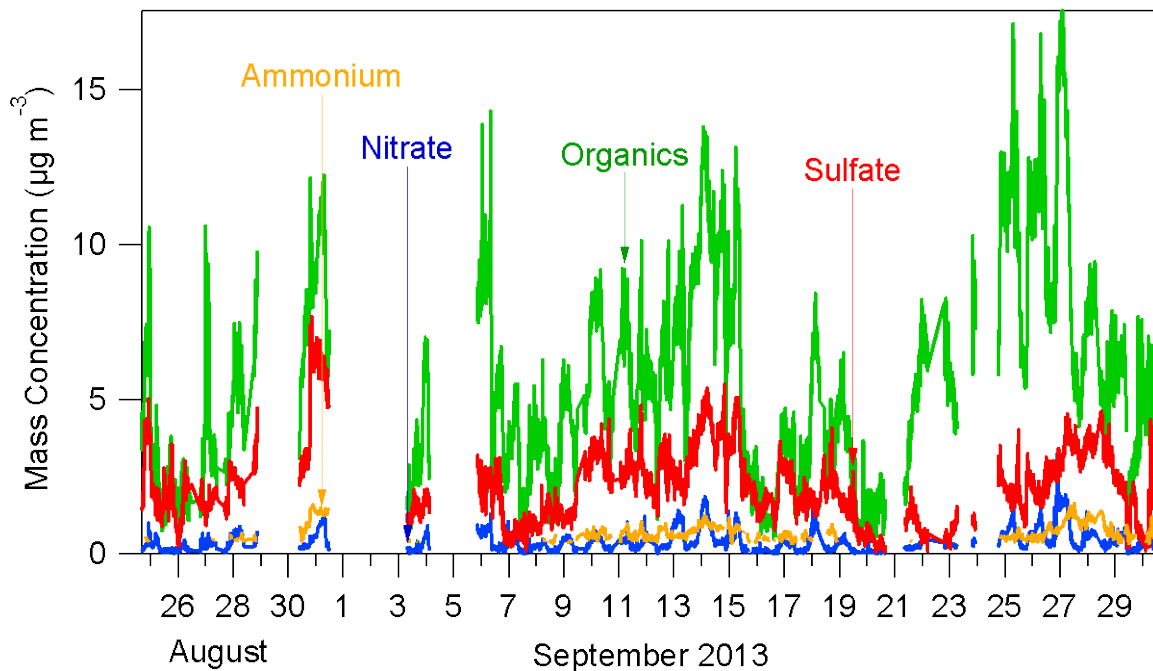


Figure 16. Time series of organics, nitrates, sulfate and ammonium measured throughout the campaign. Measured nitrates were due to organic nitrates.

Figure 17 shows the average diurnal variation of organics, nitrate and sulfate. Analysis of variance (ANOVA) revealed statistically significant variation by time of day for organic and nitrate concentrations ($p < 10^{-16}$), but no statistically significant variation by time of day for sulfate concentrations ($p = 0.77$). This is consistent with a more regional source of sulfate, with measured concentrations influenced by transport to the site, and a more local source of organics and organic nitrates, potentially night-time formation of organic aerosol from reactions of the nitrate radical with biogenic volatile organic compounds emitted in and near Conroe. Harmonic analysis revealed that the diurnal cycle of organics had an amplitude of $1.4 \mu\text{g m}^{-3}$ and phase of 0.66 which could explain 84% of the variance; the diurnal cycle of NO_3 had an amplitude of $0.25 \mu\text{g m}^{-3}$ and phase of 0.93 which could explain 87% of the variance. The similar phase of these two diurnal cycles is consistent with a common source, which is consistent with the NO_3 due to organic nitrogen species.

Figure 18 shows the average diurnal cycle of the organic aerosol oxygen to carbon ratio (O:C), estimated from f_{44} measured throughout the campaign as explained above. Analysis of variance (ANOVA) revealed statistically significant variation by time of day ($p < 10^{-16}$) with higher O:C in the afternoon, consistent with photochemical processing of the organic aerosol. Harmonic analysis suggests an amplitude of 0.11 and phase of -2.32 which could explain 87% of the variance.

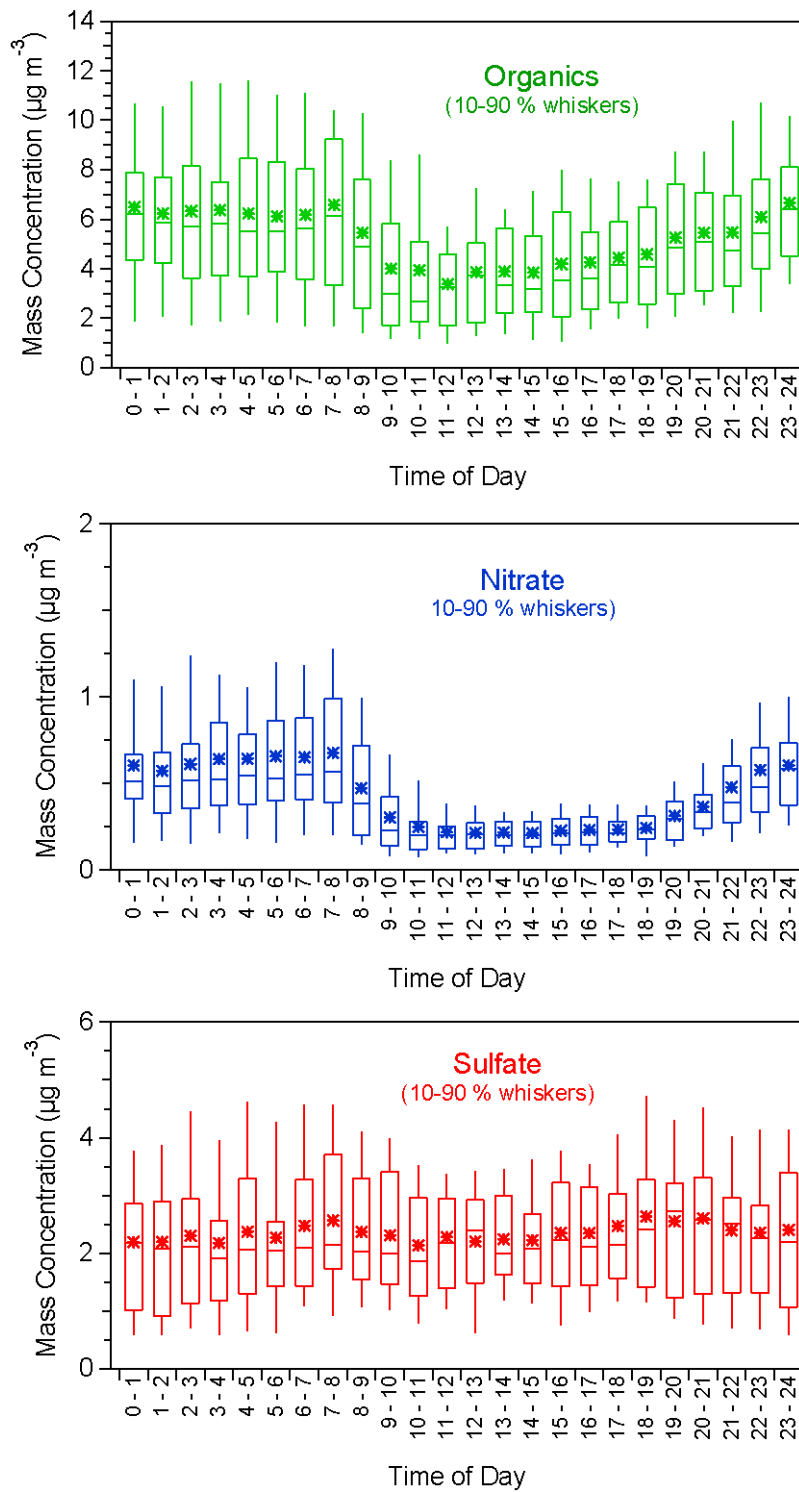


Figure 17. Diurnal cycle of organic, sulfate and nitrate mass concentrations.

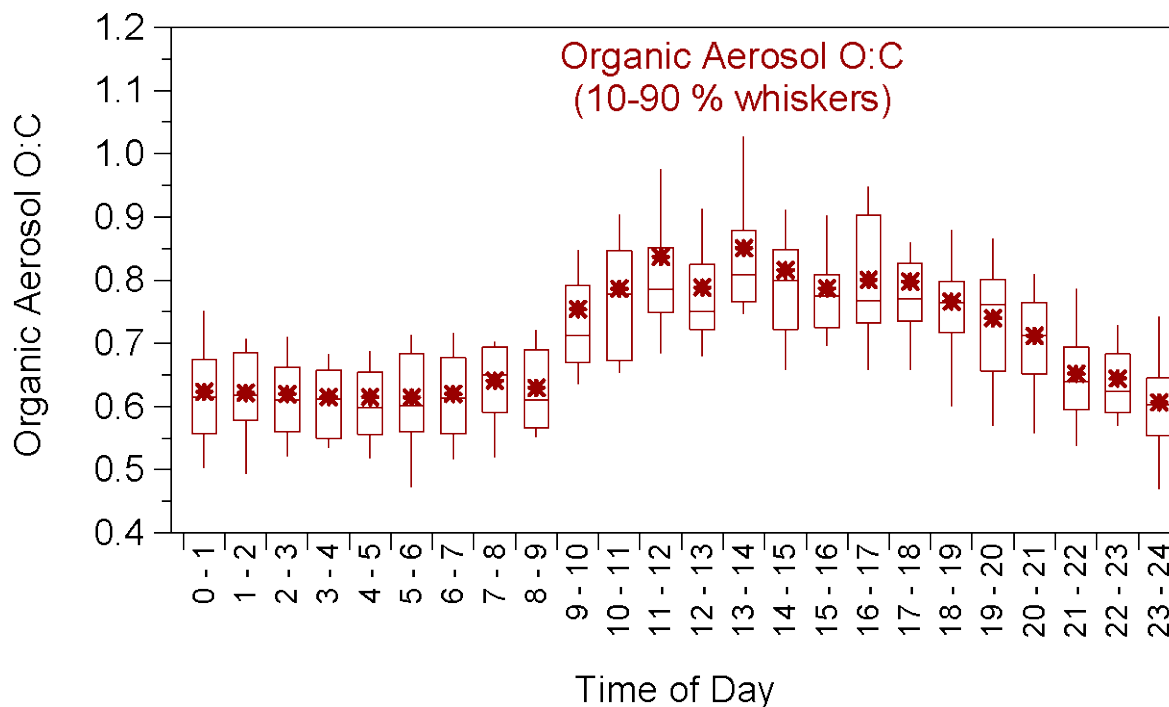


Figure 18. Diurnal cycle of organic aerosol oxygen to carbon ratio (O:C).

6.3.1 Comparison to other instruments

Measurements collected by the ACSM were compared to measurements of total particle volume taken by the SEMS and measurements of inorganic species from PM_{2.5} filter samples. Total volume concentrations measured by the SEMS were converted to mass concentrations using a bulk density calculated from ACSM composition. Total PM₁ mass concentrations measured by the ACSM and the SEMS generally agreed well (Figure 19). The SEMS exhibited higher concentrations which is expected since it measures total particle volume while the ACSM only measures non-refractory species. PM components such as black carbon and sea salt would thus be measured by the SEMS but not by the ACSM.

The comparison to filter measurements also generally showed good agreement (Figure 20). For measurements of sulfate, the filter data suggests higher concentrations (38% higher on average), which is consistent with the higher size cut-off of the filter samples (2.5 μm) compared to the ACSM (1 μm). The difference between filter and ACSM measurements of organics is lower (filters measured 12 % more organics on average), which suggests that between 1 and 2.5 μm particles generally exhibit a higher sulfate/organics ratio than the particles below 1 μm in diameter. The filter data further suggests that there was very little inorganic nitrate present in PM_{2.5}. This is consistent with the nitrate measured by the ACSM being due to organic nitrates, which is consistent with the mass spectral signature of nitrates measured by the ACSM.

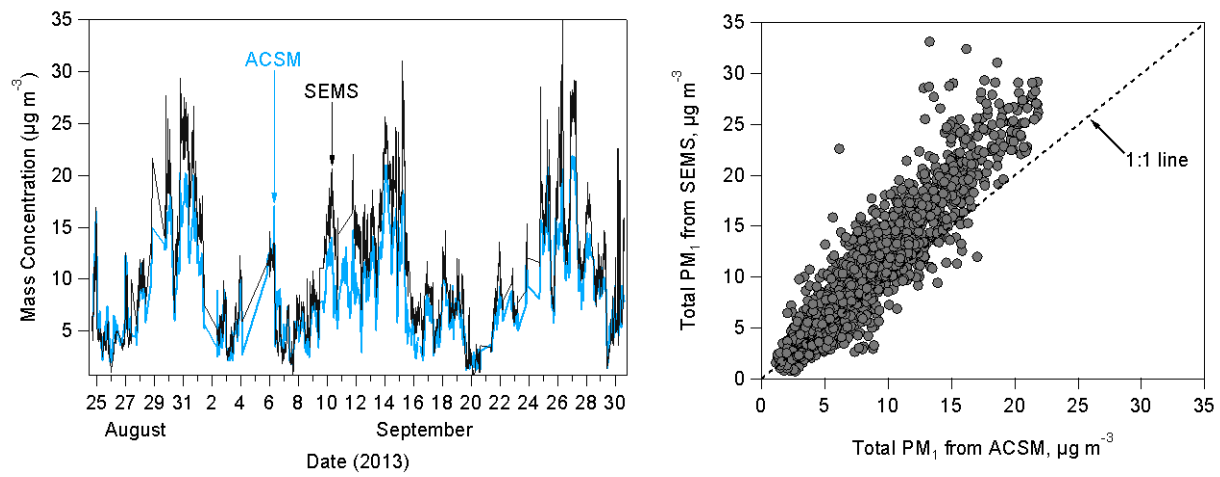


Figure 19. Time series (left) and scatter plot (right) comparing PM_{10} measurements taken by the ACSM and the SEMS.

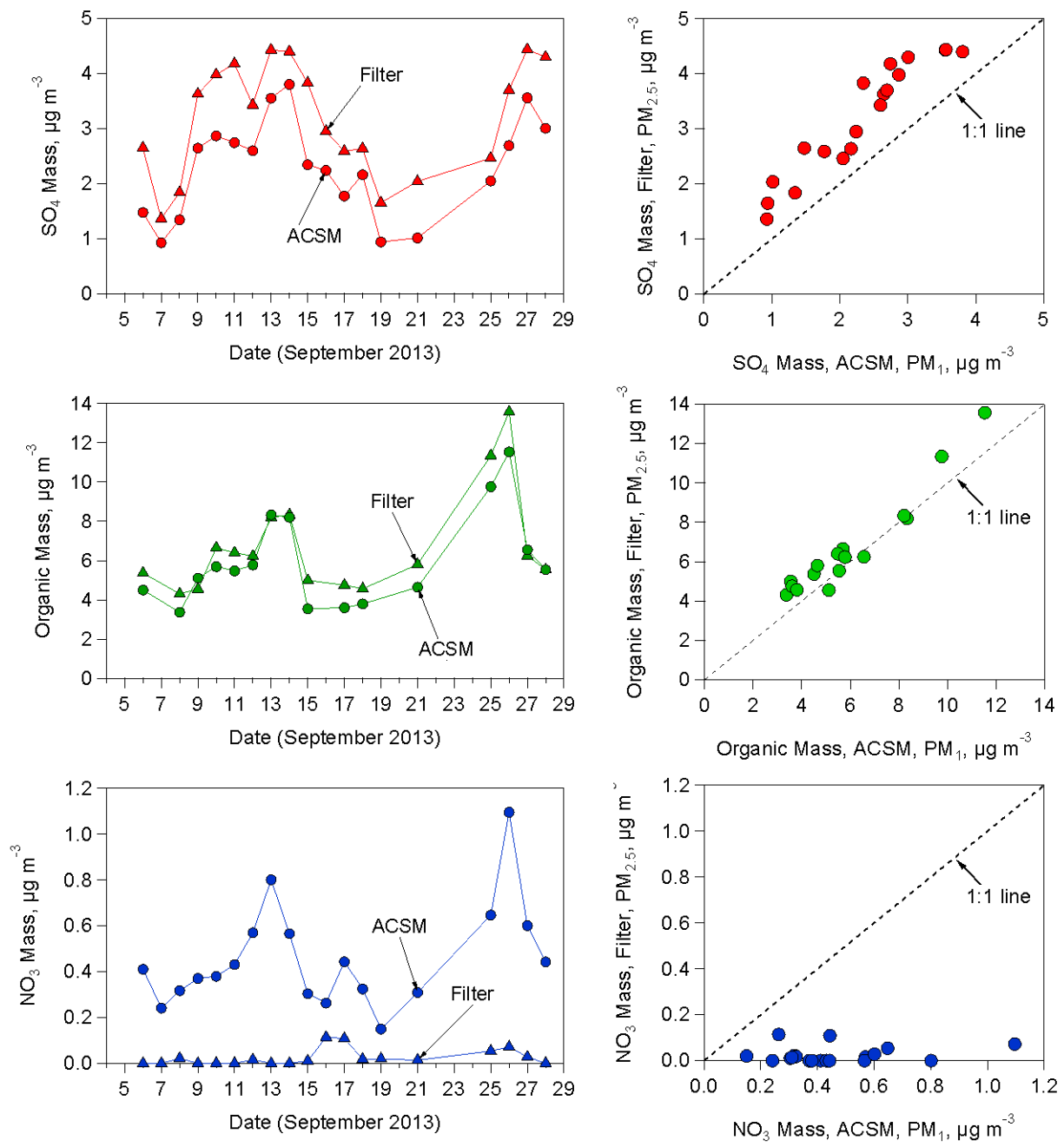


Figure 20. Time series (left) and scatter plots (right) comparing measurements of sulfate (top), organics (middle) and nitrate (bottom) taken by the ACSM (PM₁) and from filter measurements (PM_{2.5}).

7.0 Positive Matrix Factorization (PMF) Analysis

We applied positive matrix factorization (PMF; Paatero and Tapper, 1994) to the organic aerosol mass spectra measured by the ACSM. The PMF2 algorithm (version 4.2) by P. Paatero was used to solve the bilinear unmixing problem as represented and described below. PMF has proven useful in the analysis of ambient organic aerosol data, and details of the mathematical model, its application, output evaluation, and factor interpretation have been described elsewhere (Hildebrandt et al., 2010, 2011; Lanz et al., 2007, 2009; Ulbrich et al., 2009). A key assumption is that the measured dataset can be separated into a number of constant components (here, ACSM mass spectra) contributing varying concentrations over time. The problem is represented in matrix form by:

$$\mathbf{X}=\mathbf{GF}+\mathbf{E} \quad (15)$$

where \mathbf{X} is an $m \times n$ matrix of the measured data with m rows of average mass spectra (number of time periods = m) and n columns of time series of each m/z sampled (number of m/z sampled and fit = n). \mathbf{F} is a $p \times n$ matrix with p factor profiles (constant mass spectra), \mathbf{G} is an $m \times p$ matrix with the corresponding factor contributions, and \mathbf{E} is the $m \times n$ matrix of residuals. \mathbf{G} and \mathbf{F} are fit to minimize the sum of the squared and uncertainty-scaled residuals (Paatero and Tapper, 1994).

Various PMF solutions (obtained by varying the number of factors and other PMF settings) were examined and evaluated with respect to mathematical diagnostics and ancillary data (not included in the PMF analysis, e.g. ACSM-sulfate). The 3-factorial PMF solution appears to best represent our data. The profiles of the three factors are presented in Figure 21. Two of the factors resemble oxygenated organic aerosol (OOA), the other factor resembles fresher organic aerosol. We name the more oxidized OOA factor ($f_{43} = 3.8\%$, $f_{44} = 17.2\%$) MO-OOA (more oxidized OOA) and the less oxidized OOA factor ($f_{43} = 15.0\%$, $f_{44} = 5.8\%$) LO-OOA (less oxidized OOA). The third factor has mass spectral signatures representative of hydrocarbon like organic aerosol (HOA) and biomass burning organic aerosol (BBOA), and so we name the third factor ($f_{43} = 1.4\%$, $f_{44} = 6.6\%$) HBBOA.

The time series of MO-OOA showed a strong correlation with the time series of sulfate measured by the ACSM ($R^2 = 0.69$), whereas LO-OOA did not ($R^2 = 0.27$). Thus, MO-OOA correlated with a low-volatility inorganic component (sulfate). We also examined correlations of the factor profiles with factor profiles identified in previous work. The MO-OOA profile correlated most strongly with previously identified MO-OOA ($R^2 = 0.92$), the LO-OOA profile correlated most strongly with previously identified LO-OOA SOA ($R^2 = 0.87$) and α -pinene SOA ($R^2 = 0.91$), and the HBBOA correlated most strongly to previously identified BBOA ($R^2 = 0.77$) and OA from ship emissions ($R^2 = 0.67$).

Figure 22 shows time series of the factors in terms of absolute concentrations (top panel) and as a percentage of total organic signal (bottom panel). Figure 23 shows the diurnal cycle of the three PMF factors. According to analysis of variance (ANOVA), all three factors exhibited statistically significant variation by time of day ($p < 10^{-16}$ for HBBOA and LO-OOA, $p = 0.0001$ for MO-OOA). LO-OOA and HBBOA exhibited a clear pattern with higher concentrations at night, the same pattern exhibited by total OA. MO-OOA did not show this clear pattern, presumably because during the afternoon some LO-OOA and HBBOA is converted to the more highly oxidized MO-OOA. Harmonic analysis suggests that the diurnal cycle of LO-OOA has an amplitude of $0.78 \mu\text{g m}^{-3}$ and phase of 0.98 and can explain 88% of the variance; the diurnal cycle of HBBOA has an amplitude of $0.29 \mu\text{g m}^{-3}$, phase of 0.65 and can explain 78% of the variance. These two PMF factors (LO-OOA and HBBOA) hence have similar diurnal cycles (a cycle of similar phase), which is also similar to the phase of the diurnal cycle of total OA (Section 6). This could indicate that a similar process is controlling the concentrations of LO-OOA and HBBOA; for example, the decrease in concentrations of LO-OOA and HBBOA in the afternoon could be due to photochemical transformation of these species to MO-OOA. On average, 85% of the measured PM_{10} organics was due to oxygenated organic aerosol, which is representative of organic aerosol that has been processed in the atmosphere, highlighting the importance of atmospheric processing on controlling fine PM concentrations in the Houston region.

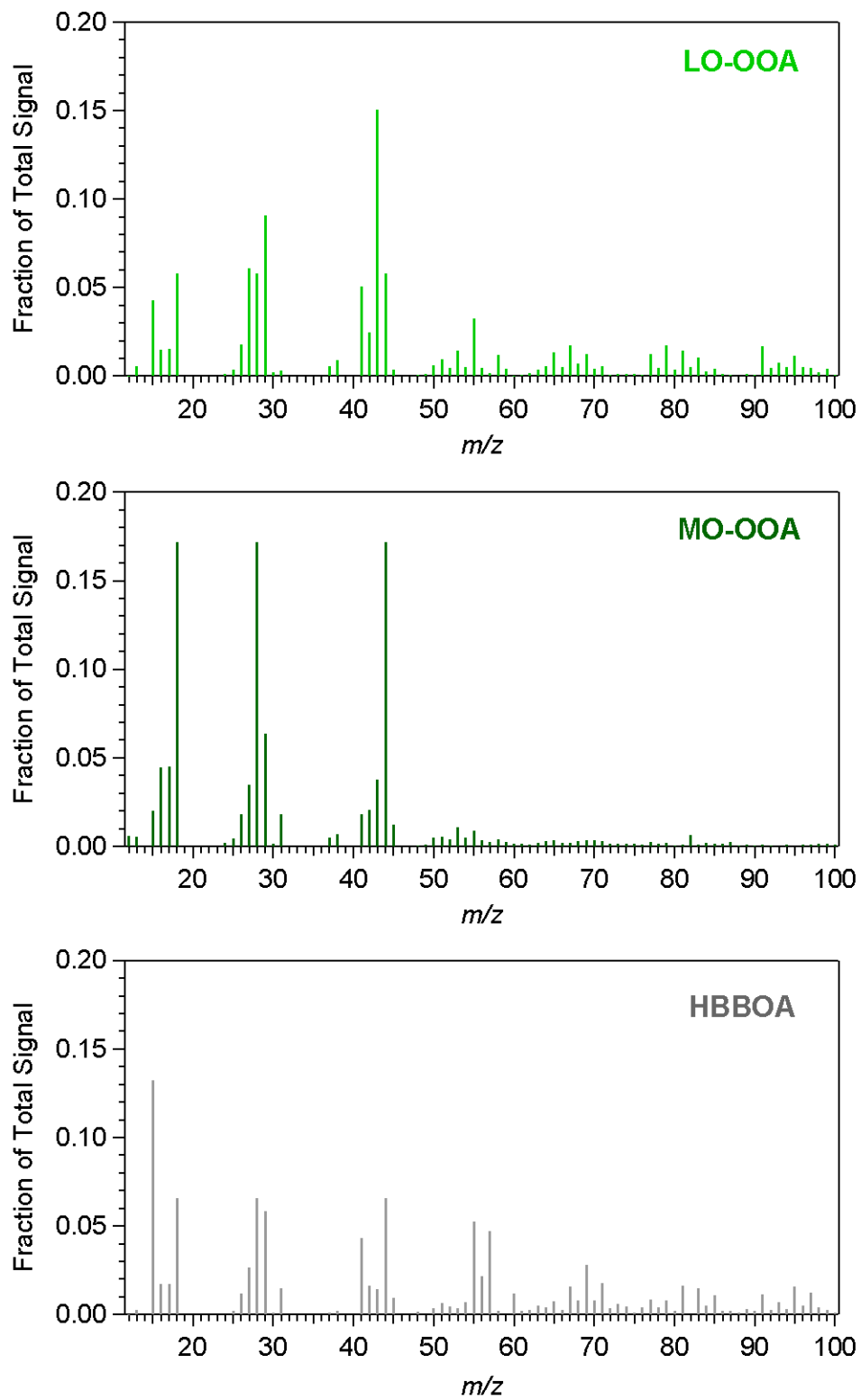


Figure 21. Profiles of selected PMF factors.

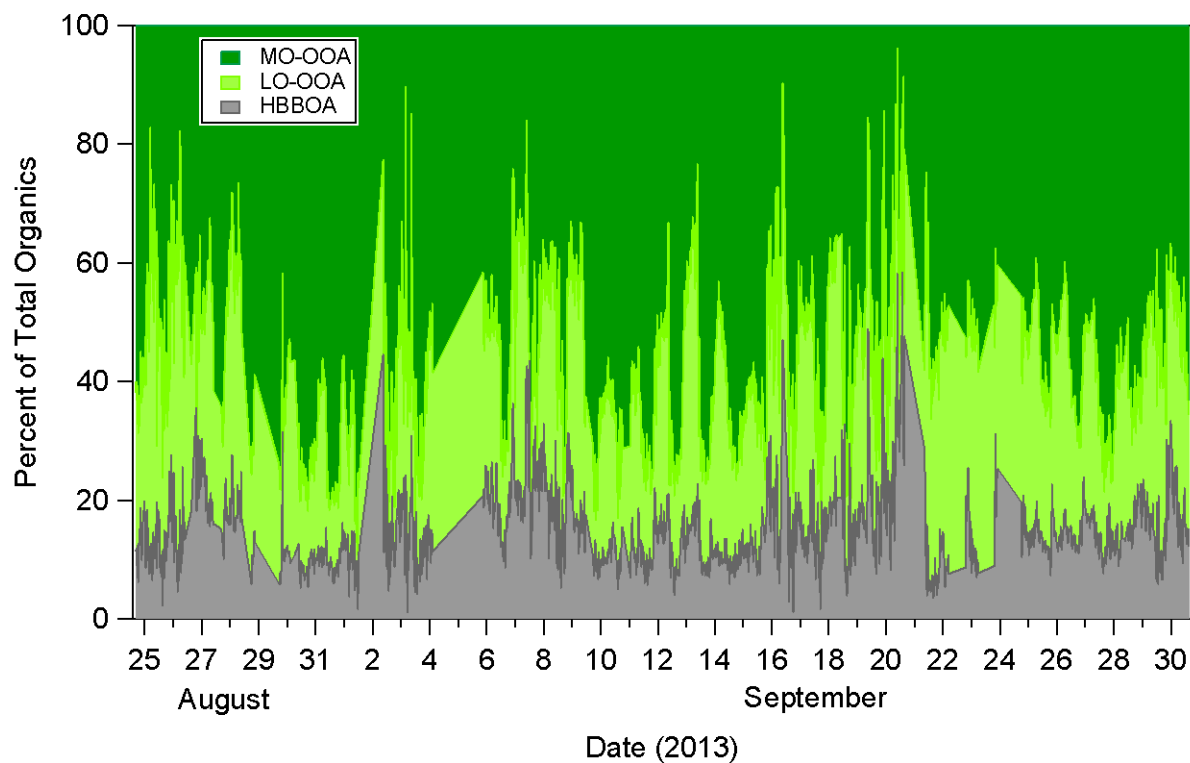
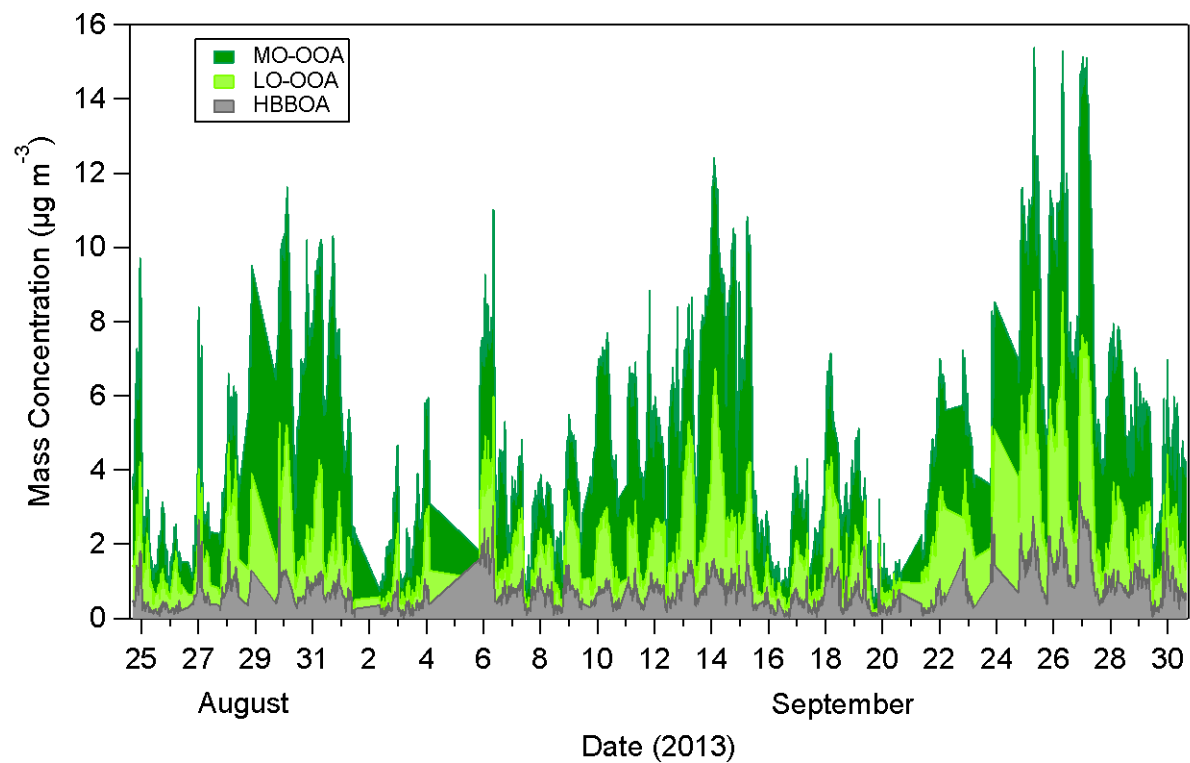


Figure 22. Time series of selected factors in terms of absolute concentrations (top panel) and fractional concentrations (bottom panel).

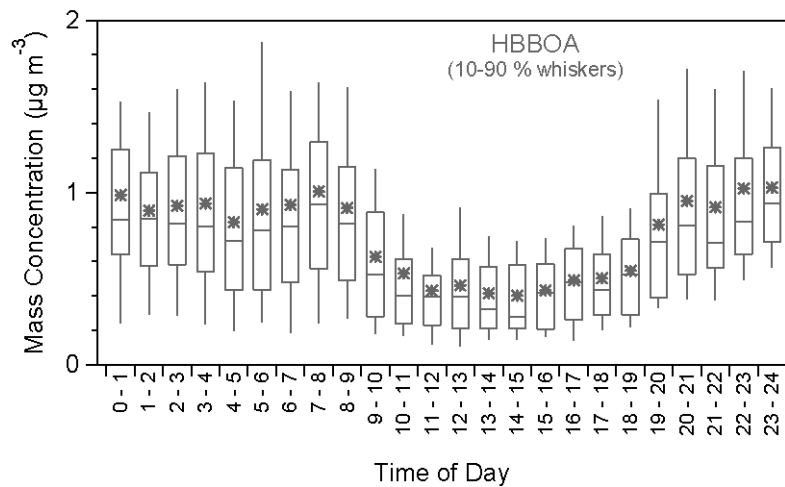
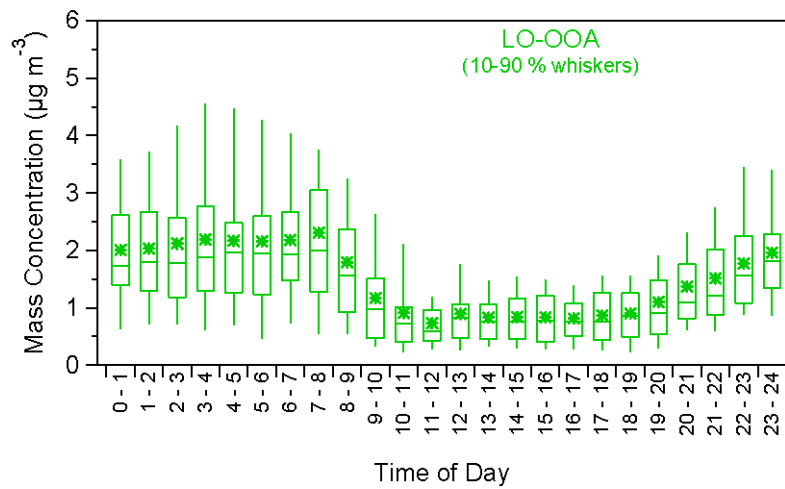
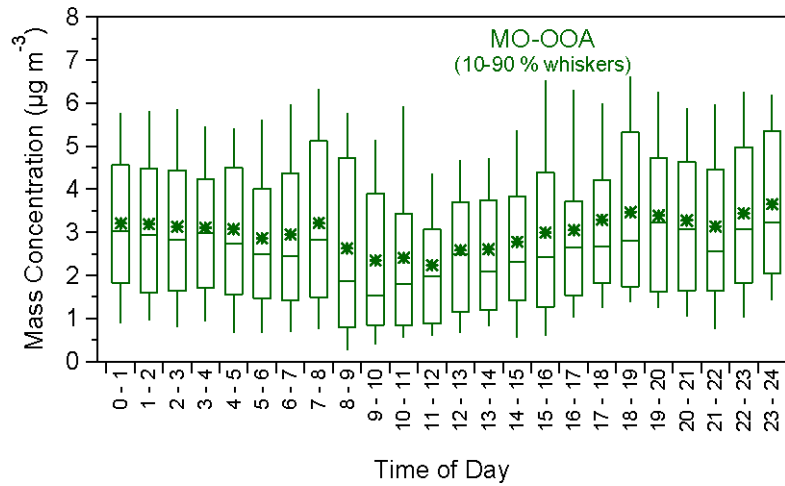


Figure 23. Diurnal cycle of PMF factors.

8.0 Model Evaluation

8.1 Evaluation of OC and EC using PM_{2.5} Filter Measurements

Filter-based PM_{2.5} measurements at the Conroe (CAMS 78), Moody Tower, and Manvel Croix (CAMS 84) monitoring stations were conducted by Drs. Sheesley and Usenko (Baylor University) during the 2013 DISCOVER-AQ campaign (AQRP Project 14-029). PM_{2.5} samples were collected using the TISCH Environmental high volume sampler (HV2.5) and the URG Corporation medium volume sampler (MV2.5) at Moody Tower and Manvel Croix while only the high volume sampler data is available at Conroe. Various sampling frequencies were used (3.5 to 24 hours). The measurement data has been corrected for field blanks, but no further artifact correction was applied.

Bulk analysis of OC and EC on quartz-fiber filters is typically done by heating the sample first under inert condition (in He) and then under oxidizing condition (in He and 2% O₂): OC is first volatilized in He and then EC in the next step. However, some OC can pyrolyse under the inert condition. Two methods are widely used to correct for OC pyrolysis: thermal optical transmittance (TOT) and thermal optical reflectance (TOR). Due to differences between the two methods, they result in different OC and EC concentrations. The OC and EC concentrations at the Conroe, Moody Tower, and Manvel Croix sites were analyzed using TOT. For comparison, we also estimated TOR OC and EC using the following relationship that was derived from data collected at the TCEQ Clinton Drive site (CAMS 403) in Houston:

$$OC_{TOR} = 0.91 OC_{TOT} + 0.0067$$

$$EC_{TOR} = 1.34 EC_{TOT} - 0.0079$$

Figures 23 through 25 compare observed OC and EC concentrations to modeled concentrations using the CAMx modeling described above. Modeled hourly concentrations were averaged to match the measurement sampling intervals. The OA:OC ratios shown in Table 8 were applied to convert modeled OA to OC. In general, CAMx underpredicts OC and overpredicts EC.

Differences between TOT and TOR are marginal. The model predicted the observed OC peak on 9/26 at Conroe relatively well, but significantly underpredicted observed peaks at Moody Tower and Manvel Croix. EC was consistently overpredicted except for the MV2.5 measurements at Manvel Croix. However, the absolute magnitudes of the EC biases are relatively small as EC concentrations are generally low.

Table 11 summarizes performance metrics of modeled OC and EC at each monitoring site.

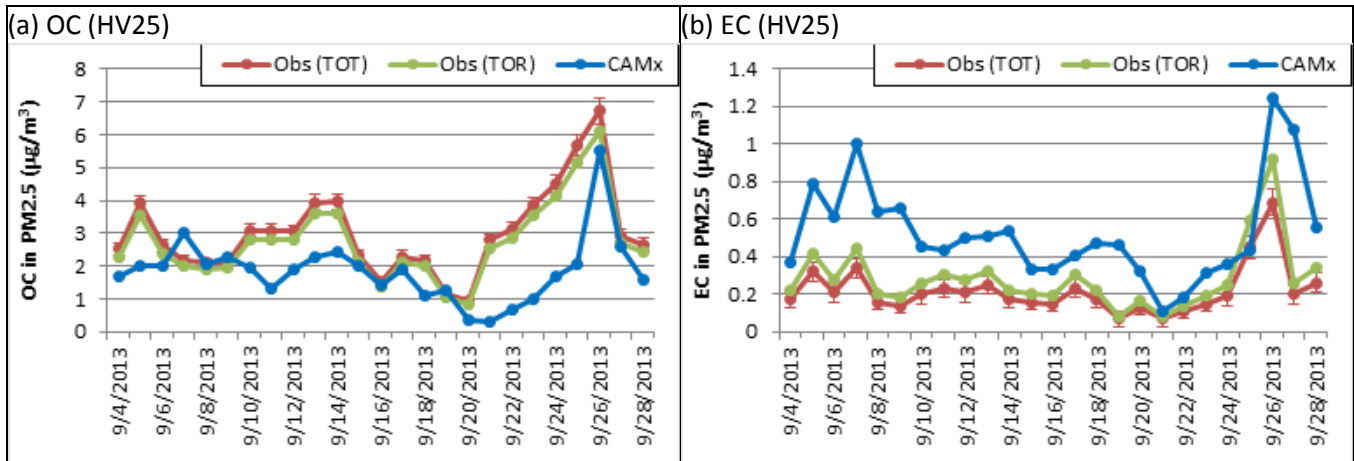


Figure 24. Modeled vs. observed OC and EC concentrations at Conroe during September 2013; PM2.5 was collected using the TISCH high volume sampler (HV25); OC and EC concentrations were analyzed using the thermal optical transmittance (TOT) technique; OC and EC via thermal optical reflectance (TOR) were estimated using an empirical relationship between TOT and TOR (see text).

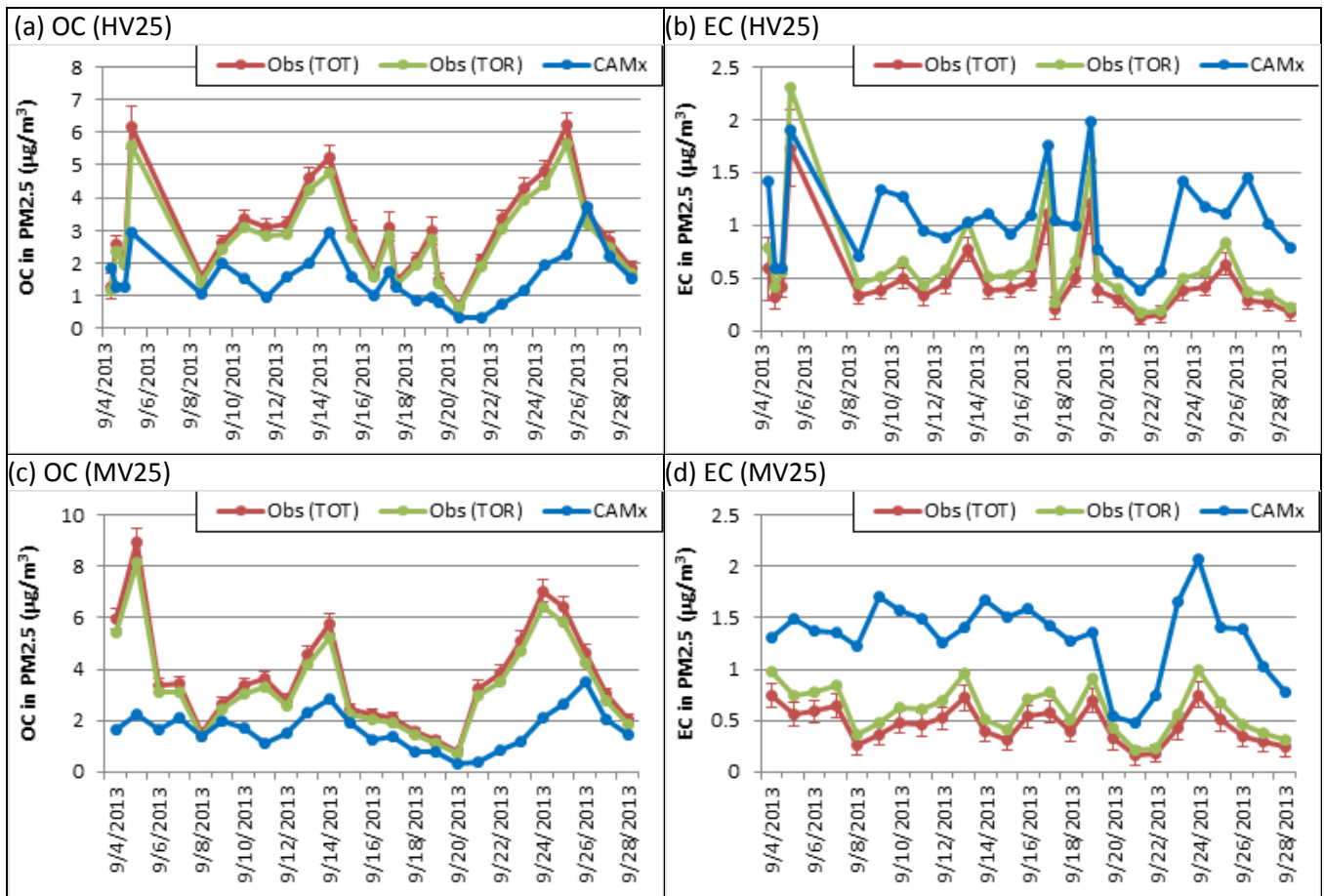


Figure 25. Modeled vs. observed OC and EC concentrations at Moody Tower during September 2013; PM_{2.5} was collected using the TISCH high volume sampler (HV25) and URG medium volume sampler (MV2.5); OC and EC concentrations were analyzed using the thermal optical transmittance (TOT) technique; OC and EC via thermal optical reflectance (TOR) were estimated using an empirical relationship between TOT and TOR (see text).

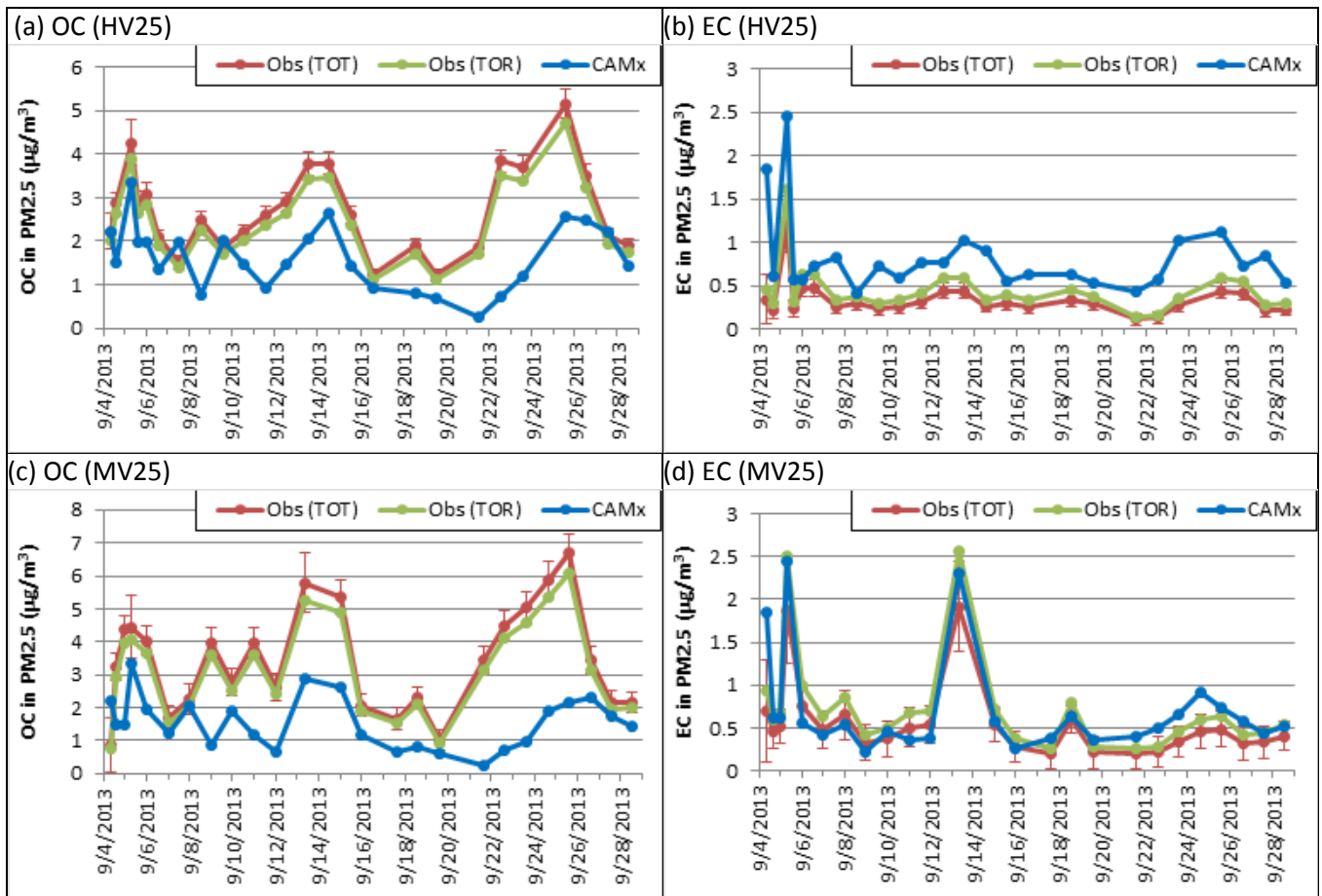


Figure 26. Modeled vs. observed OC and EC concentrations at Manvel Croix during September 2013; PM_{2.5} was collected using the TISCH high volume sampler (HV25) and URG medium volume sampler (MV2.5); OC and EC concentrations were analyzed using the thermal optical transmittance (TOT) technique; OC and EC via thermal optical reflectance (TOR) were estimated using an empirical relationship between TOT and TOR (see text).

Table 11. Performance metrics^a of modeled OC and EC concentrations against filter measurements.

	Site	Sampler	TOT					TOR				
			MO ^b	MB	ME	NMB	NME	MO ^b	MB	ME	NMB	NME
OC	Conroe	HV2.5	3.0	-1.2	1.2	-38%	41%	2.7	-0.89	1.0	-32%	37%
	Moody	HV2.5	3.0	-1.5	1.5	-49%	51%	2.7	-1.2	1.3	-44%	47%
	Tower	MV2.5	3.7	-2.0	2.0	-55%	55%	3.3	-1.7	1.7	-51%	51%
	Manvel	HV2.5	2.7	-1.1	1.1	-40%	42%	2.5	-0.85	0.96	-34%	39%
	Croix	MV2.5	3.4	-1.9	2.0	-55%	58%	3.1	-1.6	1.7	-50%	54%
EC	Conroe	HV2.5	0.22	0.31	0.31	141%	142%	0.28	0.24	0.25	85%	90%
	Moody	HV2.5	0.49	0.58	0.58	118%	118%	0.65	0.42	0.45	64%	69%
	Tower	MV2.5	0.46	0.87	0.87	189%	189%	0.61	0.72	0.72	119%	119%
	Manvel	HV2.5	0.34	0.48	0.48	142%	142%	0.44	0.37	0.38	84%	85%
	Croix	MV2.5	0.55	0.16	0.22	29%	41%	0.73	-0.02	0.20	-2%	27%

^a Definitions of performance metrics:

$$\text{Mean Bias (MB; } \mu\text{g}/\text{m}^3) = \sum_{i=1}^N (P_i - O_i) / N$$

$$\text{Mean Error (ME; } \mu\text{g}/\text{m}^3) = \sum_{i=1}^N |P_i - O_i| / N$$

$$\text{Normalized Mean Bias (NMB; \%)} = \sum_{i=1}^N (P_i - O_i) / \sum_{i=1}^N O_i$$

$$\text{Normalized Mean Error (NME; \%)} = \sum_{i=1}^N |P_i - O_i| / \sum_{i=1}^N O_i$$

where P_i and O_i are predicted and observed values on the i -th simulation day, respectively; N is the number of simulation days.

^b Mean observed concentration.

8.2 Evaluation of OA mass and O:C ratio using ACSM PM1 measurements

The 1.5-D VBS scheme predicts O:C ratio in addition to OA mass and the ACSM data provide an opportunity to evaluate model performance for both parameters simultaneously. A potential difficulty is that the model predicted PM_{2.5} whereas the ACSM measured PM₁, however this difficulty is minor because PM₁ OA accounts for most of the mass of PM_{2.5} OA. Comparison of the ACSM data with the filter measurements showed that on average the ratio of PM_{2.5} to PM₁ was approximately 1.14.

Figure 27 compares hourly PM_{2.5} OA concentrations predicted by CAMx with the ACSM PM₁ OA data. High time resolution ACSM data were aggregated into hourly averages to be consistent with the model output interval. As discussed in Section 6.3, mass spectral data suggests that the PM₁ nitrate measured by the ACSM is mostly organic nitrate, thus we compared the modeled OA with sum of the ACSM nitrate and organics. As in the evaluation using the filter measurements, the model underestimated observed OA concentrations throughout most of the modeling period.

Figure 28 compares diurnal profiles of OA concentrations modeled by CAMx vs. measured by the ACSM. Although modeled OA profile is showing much lower concentrations than the observed, both profiles show similar trends (OA decreases in the morning and increases in the evening).

For comparison with observed O:C ratios derived using the fraction of organic mass at m/z 44 (f_{44} ; see Section 6.2), modeled O:C ratios were calculated using the O:C ratio for each VBS species given in Table 8. Figure 29 shows diurnal variations of modeled and observed O:C ratios. Unlike the observed O:C profile which shows distinctively higher O:C in the afternoon, the model-predicted O:C profile is relatively flat except for early morning rush hour period when O:C decreases due to fresh emissions of OA that have lower O:C ratio. Overall, modeled OA is less oxidized (O:C = 0.3 ~ 0.5) than observed OA (O:C = 0.5 ~ 0.8).

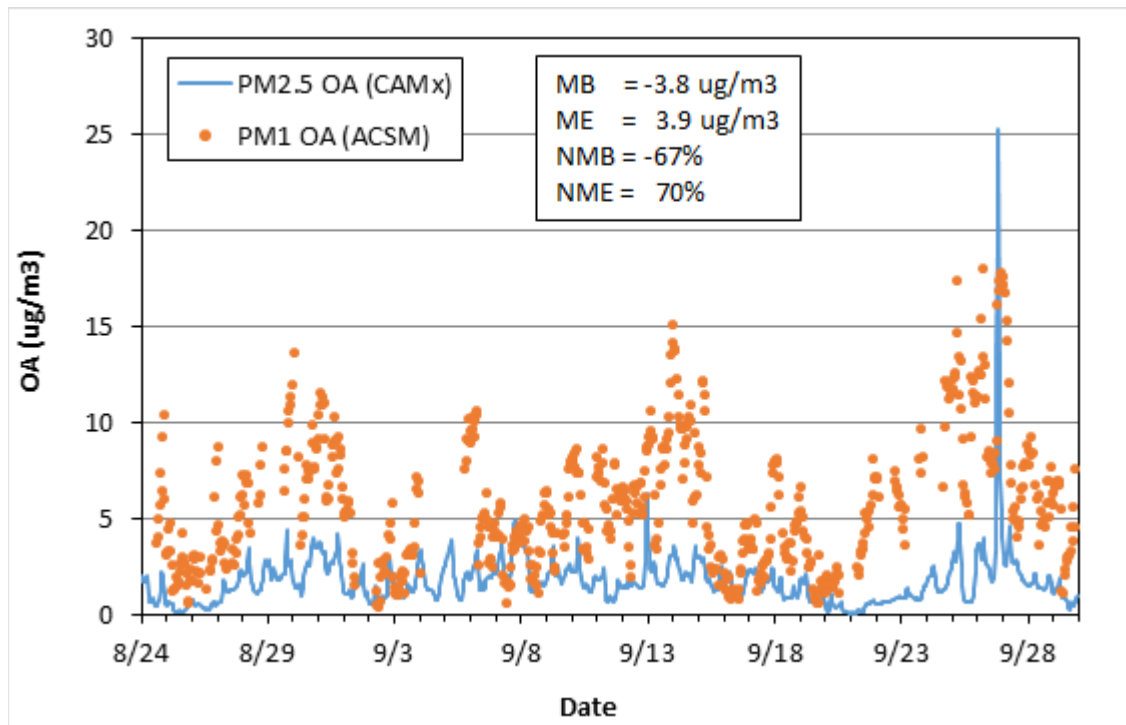
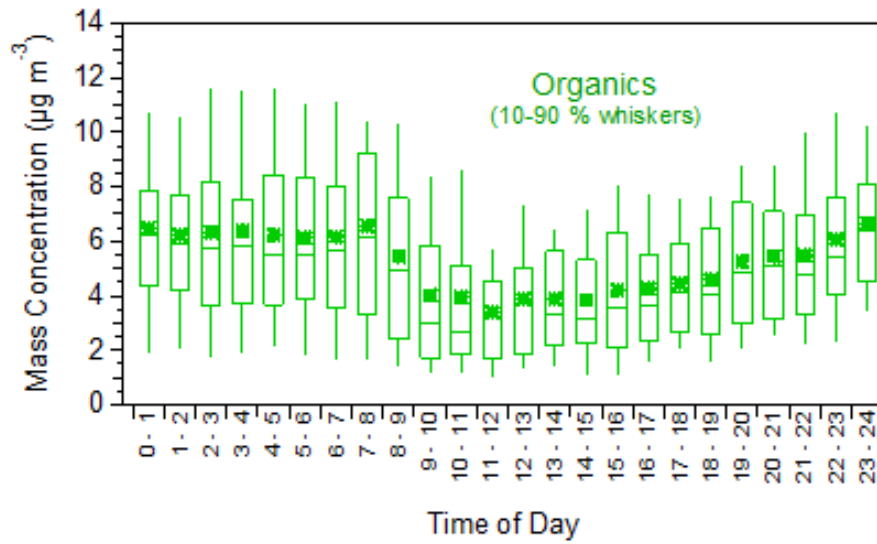


Figure 27. Hourly observed PM1 and modeled PM2.5 OA concentrations at Conroe.

(a) PM1 OA (ACSM)



(b) PM2.5 OA (CAMx)

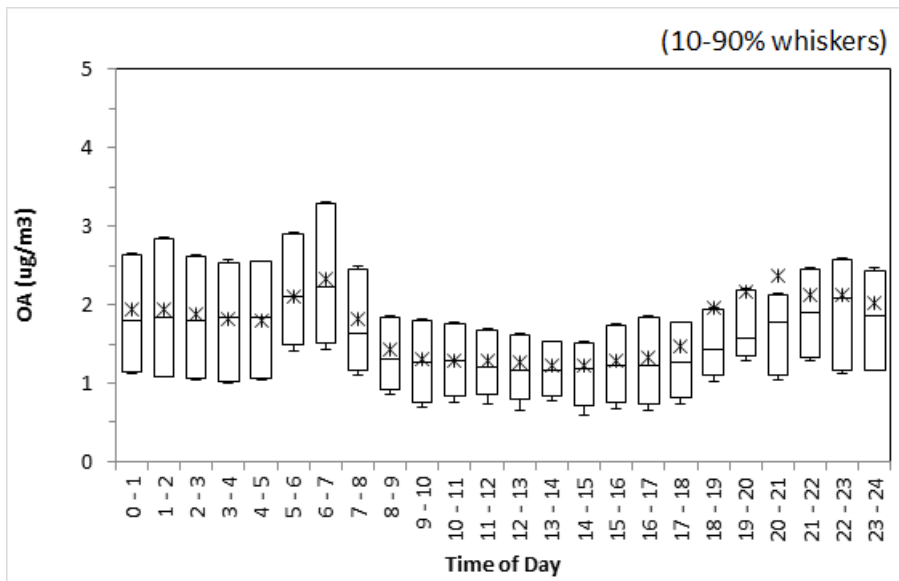
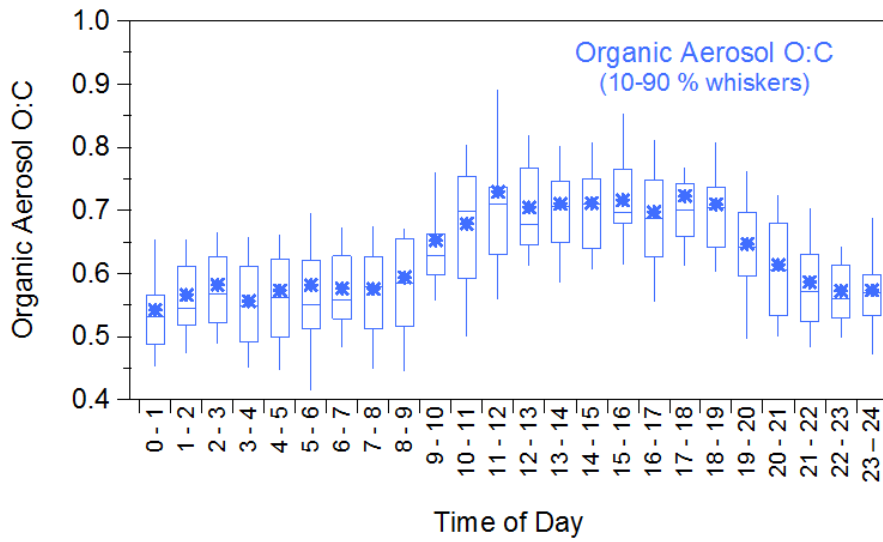


Figure 28. Box and whisker plots of diurnal cycles of observed and modeled OA concentrations at Conroe.

(a) ACSM PM1



(b) CAMx PM2.5

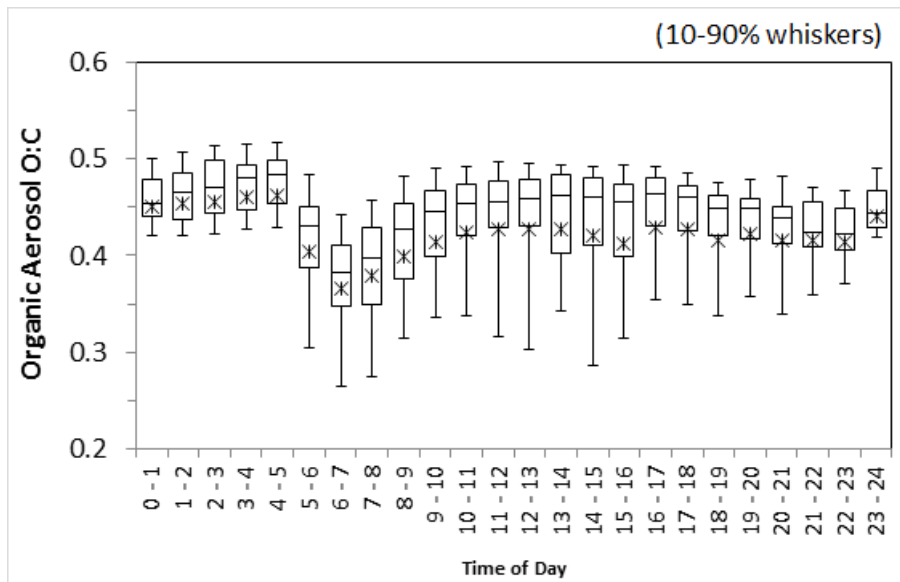
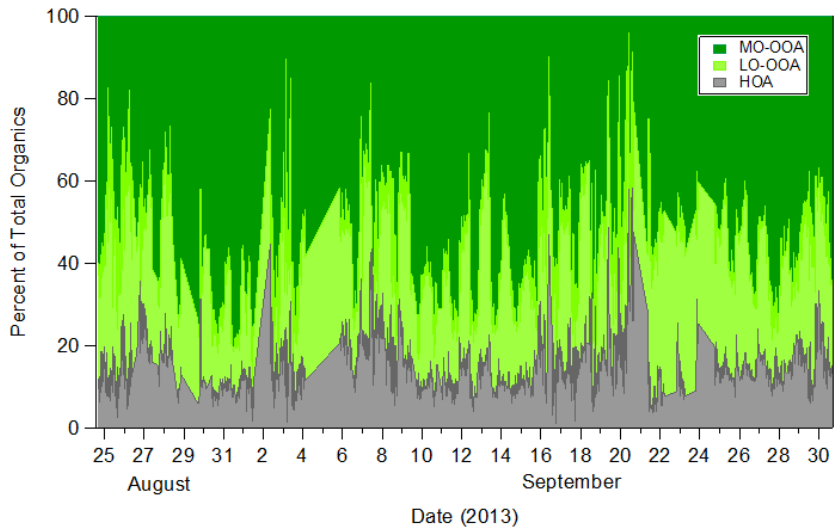


Figure 29. Box and whisker plots of diurnal cycles of observed and modeled O:C ratios.

8.3 Evaluation of OA composition using PMF analysis

As described in Section 7, PMF analysis on the AMS data collected by the ACSM identified one HOA/BBOA factor (named HBBOA) and two OOA factors (LO-OOA and MO-OOA). The CAMx VBS scheme uses 4 basis sets to separately track HOA (PAP), BBOA (PFP), and two OOA groups (PAS and PBS). Figure 30 compares time series plots of PMF-factored and CAMx-predicted OA composition. Average OOA fraction by PMF analysis (LO-OOA + MO-OOA) is higher (85%) than that predicted by CAMx (68%). This is consistent with the O:C evaluation result which suggests the modeled OA is less oxidized than the observed. Also, PMF and CAMx result in different diurnal profiles of OA composition (Figure 31). The HBBOA profile by PMF is relatively flat while CAMx shows HOA increasing in the morning rush hour period and BBOA increasing in the evening. Although total OOA by PMF does not vary much during the day, it clearly shows transformation of LO-OOA to MO-OOA (aging) in the afternoon.

(a) OA composition by PMF



(b) OA composition by CAMx

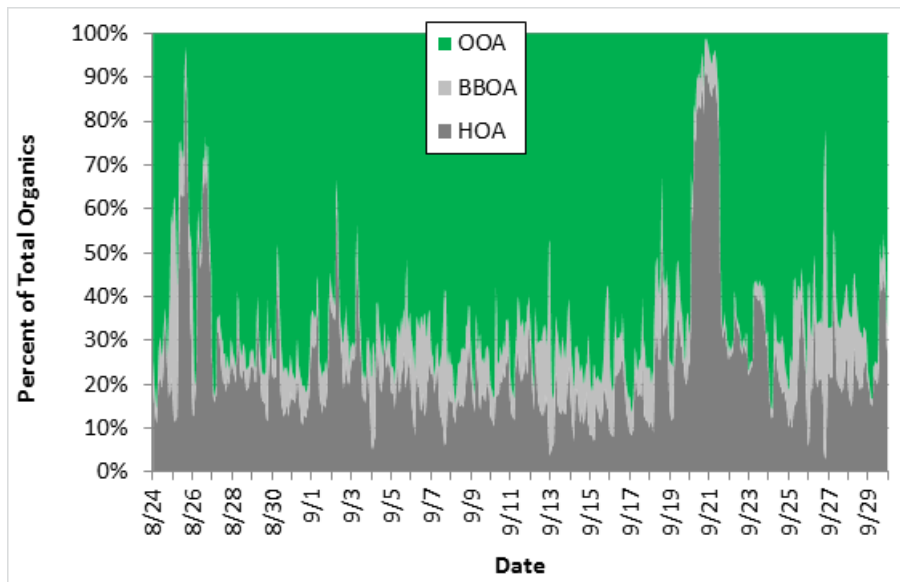
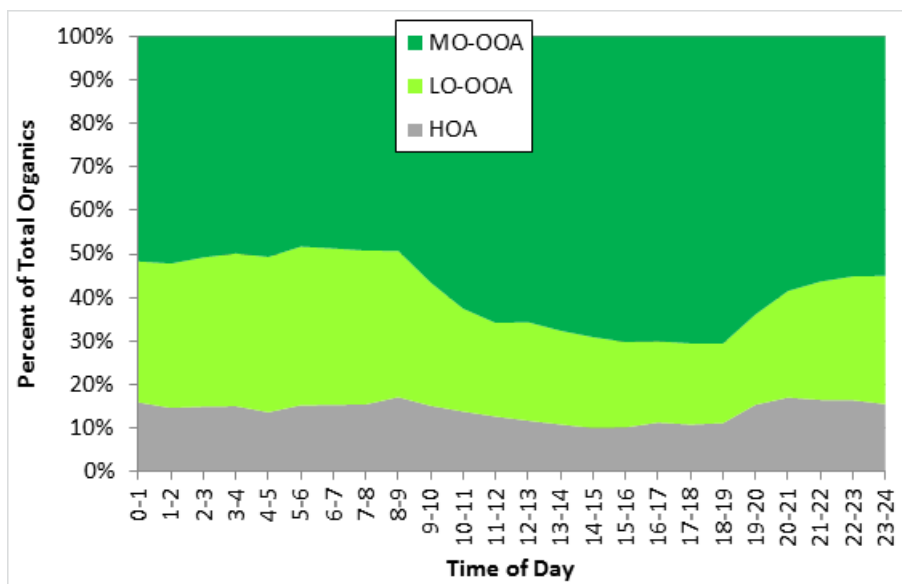


Figure 30. Comparison of OA composition by PMF and CAMx.

(a)



(b)

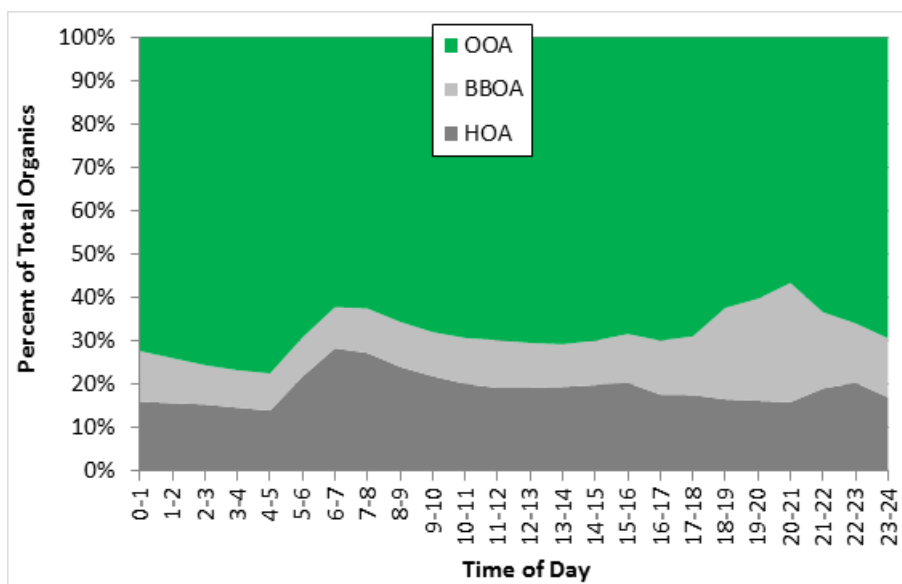


Figure 31. Average diurnal cycles of OA composition by PMF and CAMx.

8.4 Contemporary vs Fossil Carbon Analysis

Radiocarbon analysis provides source apportionment of contemporary vs. fossil carbon in atmospheric OA. The model OC results were evaluated using the radiocarbon analysis data at the Conroe, Moody Tower and Manvel Croix sites during the last week of September, provided by Dr. Sheesley (AQR Project 14-029). Contemporary carbon fraction of the measured OC was estimated based on the $^{14}\text{C}/^{12}\text{C}$ ratio for the filter sample. The contemporary fraction of the modeled OC was calculated by summing biogenic SOA (PBS) and BBOA (PFP).

In general, the model significantly underpredicted the contemporary carbon fractions while showing relatively better agreement with observations in fossil carbon mass (Figure 32). Observed contemporary carbon fractions tend to be higher during weekends (September 21-22 and 28) partially due to lower mobile emissions (fossil carbon) during weekends. One of the factors contributing to the underestimation of modeled contemporary carbon fraction is the cooking-influenced organic aerosol (CIOA). CIOA is shown to be significant accounting for 17% of total OA mass in Pasadena, CA, during the 2010 CalNex campaign (Hayes et al., 2013). We expect that CIOA would be an important component of total OA in urban areas such as Houston. However, the current model does not distinguish CIOA from other anthropogenic OA emissions (HOA) resulting in underestimation of contemporary carbon fractions: this effect may be more pronounced on the weekend days due to lower modeled OC concentrations on those days. Underestimation of biogenic SOA can also contribute low contemporary-to-fossil ratios of the modeled OC.

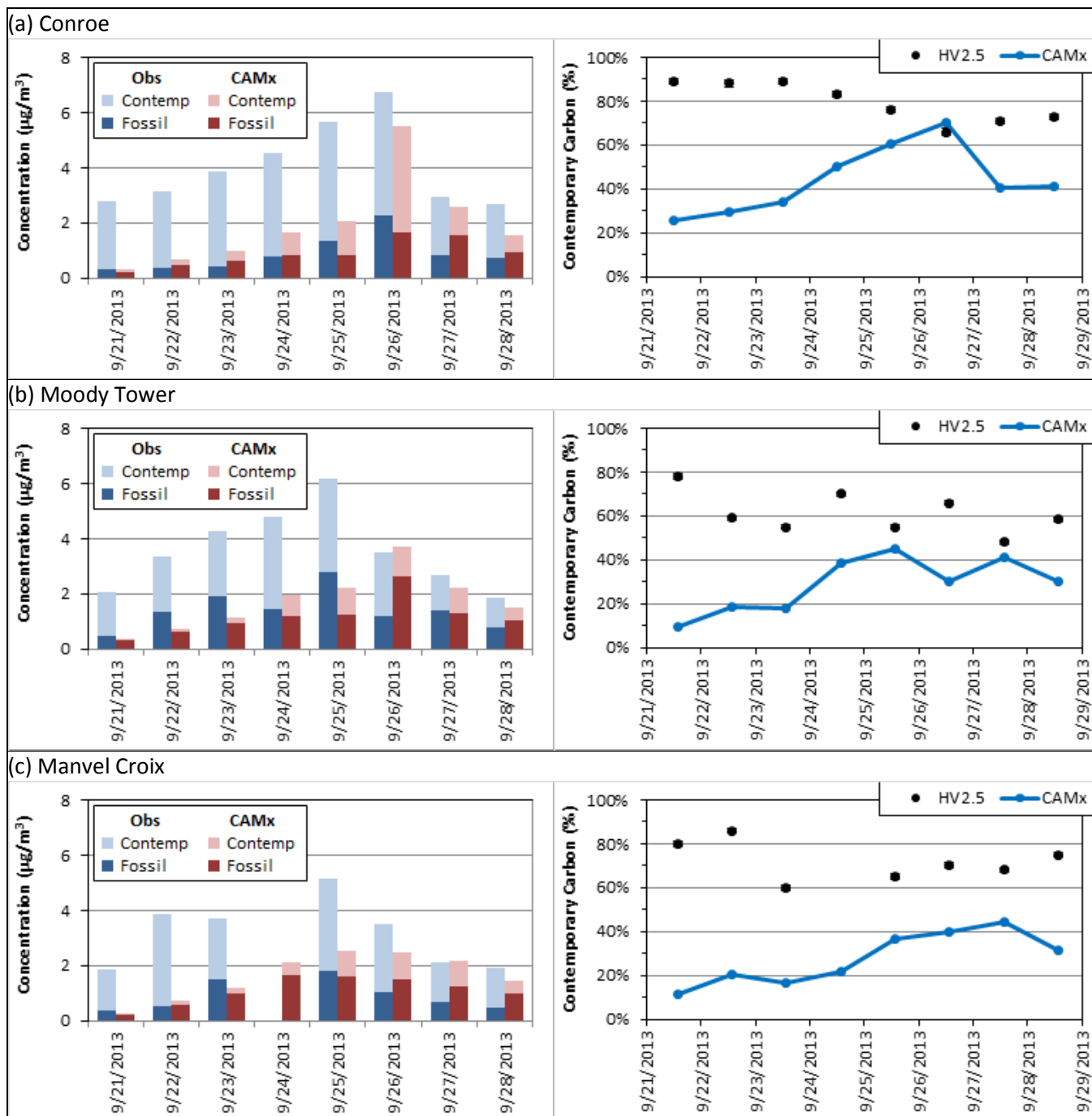


Figure 32. Observed vs. modeled organic carbon compositions (contemporary and fossil carbon mass; left panels) and contemporary carbon fractions (%; right panels) at Conroe, Moody Tower, and Manvel Croix.

8.5 Contributions of SOA Formation Pathways

To identify areas of potential improvements to the model performance, we assessed contributions of individual SOA formation pathways to total secondary OC. A brute-force approach was applied where the base model simulation is repeated with one of the pathways turned off at a time: Impact of each SOA formation pathway can be approximated by the difference between the base model result and the result without the pathway. Note that such a brute-force method does not provide a true apportionment of these pathways due to the indirect effect of gas-particle partitioning. Assuming absorptive partitioning for organic compounds (Pankow, 1994), the fraction of organics in the particle phase increases with increasing total organic mass. Therefore, eliminating a certain SOA formation pathway also decreases all other SOA components.

Figure 33 shows total secondary OC contributions from the following SOA formation pathways for a five-day test period (September 21-25):

- Oxidation reaction of aromatic VOC precursors (benzene, toluene, and xylene)
- Oxidation reaction of isoprene
- Oxidation reaction of monoterpenes with each of the oxidants (OH, O₃, and NO₃)
- Oxidation reaction of sesquiterpenes
- Oxidation reaction of IVOC from gasoline engines (IVOC_G)
- Oxidation reaction of IVOC from diesel engines (IVOC_D)
- Oxidation reaction of IVOC from biomass burning (IVOC_B)
- Chemical aging

As explained above, sum of the individual contributions is always greater than total modeled secondary OC concentration (indicated by diamond symbols on the plots). Nevertheless, we expect that the results still provide a good insight on relative importance of these contributions. Chemical aging accounts for the largest fraction (approximately 30-40%) of total secondary OC at Conroe, Moody Tower and Manvel Croix. Among biogenic VOC precursors, monoterpenes are the largest contributors with reaction with nitrate radical being the most important pathway. IVOCs account for approximately 10% of secondary OC at these sites with IVOC from gasoline engines being dominant among them.

The model evaluation using PMF (Section 8.3) and radiocarbon analysis (Section 8.4) has shown that the model tends to underestimate secondary (oxygenated) and/or contemporary carbon fractions. Therefore, we focused on possible improvements that could enhance secondary/contemporary carbon mass. Sensitivity tests for these improvements are discussed in the next section.

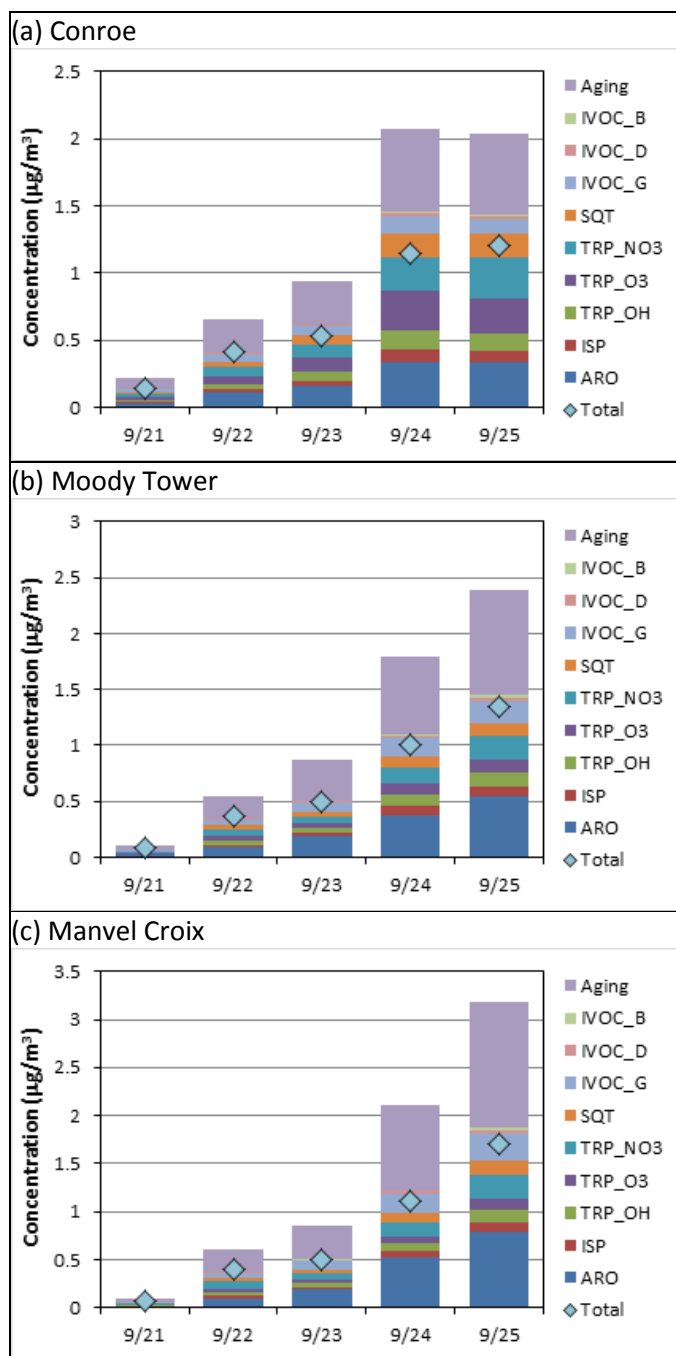


Figure 33. Contributions to daily average secondary OC concentrations from individual SOA formation pathways at Conroe, Moody Tower, and Manvel Croix, estimated by a brute-force method; total modeled secondary OC concentrations are also shown (blue diamond symbols).

8.6 Improvements to the Base Case Modeling

In this section, we discuss each modification/revision we made to the base case modeling and assess its impact on modeled OC components using a five-day test scenario (September 21-25).

8.6.1 Additional Basis Set for CIOA

As discussed earlier, CIOA could account for a significant fraction of contemporary carbon mass in urban area such as Houston. We estimated the fraction of POA emissions that are related to meat cooking, based on the TCEQ inventory data of the 8 HGB-area counties: 26% of POA emissions in the area source sector is estimated to be CIOA. We note that the TCEQ inventory does not include residential charcoal grilling (only commercial cooking is included); therefore, the CIOA fraction may be higher. We added an additional basis set (PCP) to separately track the CIOA emissions. Volatility distribution of the CIOA emissions was estimated by Woody et al. (2014) (Table 12). Molecular properties of the PCP species are set to those of the HOA basis set (PAP) as a first approximation since CIOA would have been lumped into the HOA basis set in the base case modeling.

Table 12. Volatility distribution of POA emissions.

Source category	Emission fraction for volatility bin with saturation mass concentration (C*) in $\mu\text{g m}^{-3}$ of				
	0	1	10	100	1000
Gasoline engine ^a	0.27	0.15	0.26	0.15	0.17
Diesel engine ^a	0.03	0.25	0.37	0.24	0.11
Other anthropogenic ^a	0.09	0.09	0.14	0.18	0.50
Biomass burning ^a	0.2	0.1	0.1	0.2	0.4
Meat cooking ^b	0.35	0.35	0.10	0.10	0.10

^a Koo et al., 2014.

^b Woody et al., 2014.

Figure 34 compares OC component concentrations predicted by the base model and the revised model with CIOA. Total OC slightly increased with the new basis set for meat cooking since the CIOA emissions are allocated more into lower volatility bins compared to POA emissions from other sources (Table 12). On the other hand, the contemporary carbon fractions significantly increased as the revised model can now separately track CIOA which contributes to the contemporary carbon mass. On the last day of the test period where modeled OC is highest, the contemporary carbon fractions increased by 8-24% with the revised model.

8.6.2 Updated Aerosol Yields for Monoterpene+NO₃

The ACSM data at Conroe seems to suggest significant SOA formation from reaction of biogenic VOC precursors with nitrate radical during night (Section 6.3). The brute-force analysis discussed in Section 8.5 also shows that oxidation of monoterpenes with NO₃ is an important SOA formation pathway in our modeling. However, there exist large uncertainties in the aerosol yields which are determined by fitting smog chamber data (Barsanti et al., 2013). Recently, Boyd et al. (2015) investigated the oxidation of β -pinene with NO₃ radical over a wide range of aerosol loadings and determined the aerosol yields which were weighted more towards lower volatility products than previous studies. Table 13 compares the aerosol yields estimated by Boyd et al. (2015) with those currently used in the base model.

Table 13. VBS SOA mass yields for the reaction of monoterpene with NO₃.

		Product mass yields for volatility bin with C* of				
		0	1	10	100	1000
Base model ^a	High NOx	-	0.012	0.122	0.201	0.507
	Low NOx	-	0.107	0.092	0.359	0.608
Boyd et al. (2015) ^b		0.397	0.035	0.0	1.001	-

^a Koo et al., 2014.

^b Adjusted to the aerosol density of 1.5 $\mu\text{g}/\text{m}^3$.

Figure 35 compares OC component concentrations predicted by the base model and the revised model with updated monoterpene aerosol yields by Boyd et al. (2015). The updated monoterpene aerosol yields result large increases in total OC (by 36-53% on the last day of the test period) producing more than twice as much secondary biogenic OC as the base model.

8.6.3 Adjusted Aerosol Yields for IVOC Precursors

As described in Section 4.0, the IVOC precursors in our model are represented by n-alkane surrogate species (Jathar et al., 2014). The VBS aerosol yields of these surrogate species were determined by smog chamber data (Presto et al., 2010). Our review of the chamber study revealed that the aerosol yields were calculated assuming particle density of 1 $\mu\text{g}/\text{m}^3$. As our model uses the SOA density of 1.5 $\mu\text{g}/\text{m}^3$ based on the AMS and SMPS data (Kostenidou et al., 2007), we adjusted the aerosol yields for the IVOC precursors by multiplying the original yields by 1.5.

Figure 36 compares OC component concentrations predicted by the base model and the revised model with adjusted IVOC aerosol yields. With the adjusted yields, modeled total OC increased by 4-7% on the last day of the test period.

8.6.4 Fixed Biomass Burning POA Emissions from Area Sources

From reviewing our estimation of POA emissions from combustion sources, we discovered that POA emissions from agricultural/prescribed burning were allocated too low due to incorrectly estimated organic fraction of PM emissions from those sources. Correcting this error increased the biomass burning fraction of total POA emissions in the area source category from 8% to 38%.

Figure 37 compares OC component concentrations predicted with the original and corrected biomass burning POA emissions from area sources. Corrected allocation of biomass burning POA emissions increased contemporary carbon fractions by 8-19% on the last day of the test period while making almost no change in total OC concentrations.

8.6.5 SOA Formation from Alkane VOC Precursors

SOA formation from long alkane VOC precursors (8-11 carbons) has been included in several modeling studies (Carlton et al., 2010; Lane et al., 2008; Murphy and Pandis, 2009; Strader et al., 1999) with parameterization based on limited experimental data. We assessed contribution of this SOA formation pathway which is not included in our base model: a new VOC precursor representing long chain alkanes is added to the model using the reaction rate and aerosol mass yields of ALK5 (the largest lumped alkane species in the SAPRC chemistry mechanism). The ALK5 emissions were estimated by scaling PAR (lumped species representing single carbon bond in the carbon-bond chemistry mechanism, which approximately corresponds to ALK3+ALK4+ALK5) from the TCEQ emission inventory. The ratio of ALK5 to PAR emissions was estimated based on a previous SAPRC emission estimation over the Houston region (Li, 2010).

Figure 38 compares OC component concentrations predicted by the base model and the revised model with SOA formation from ALK5. The additional SOA formation pathway only slightly increased modeled total OC concentrations (by less than 3% at the three sites over the test period).

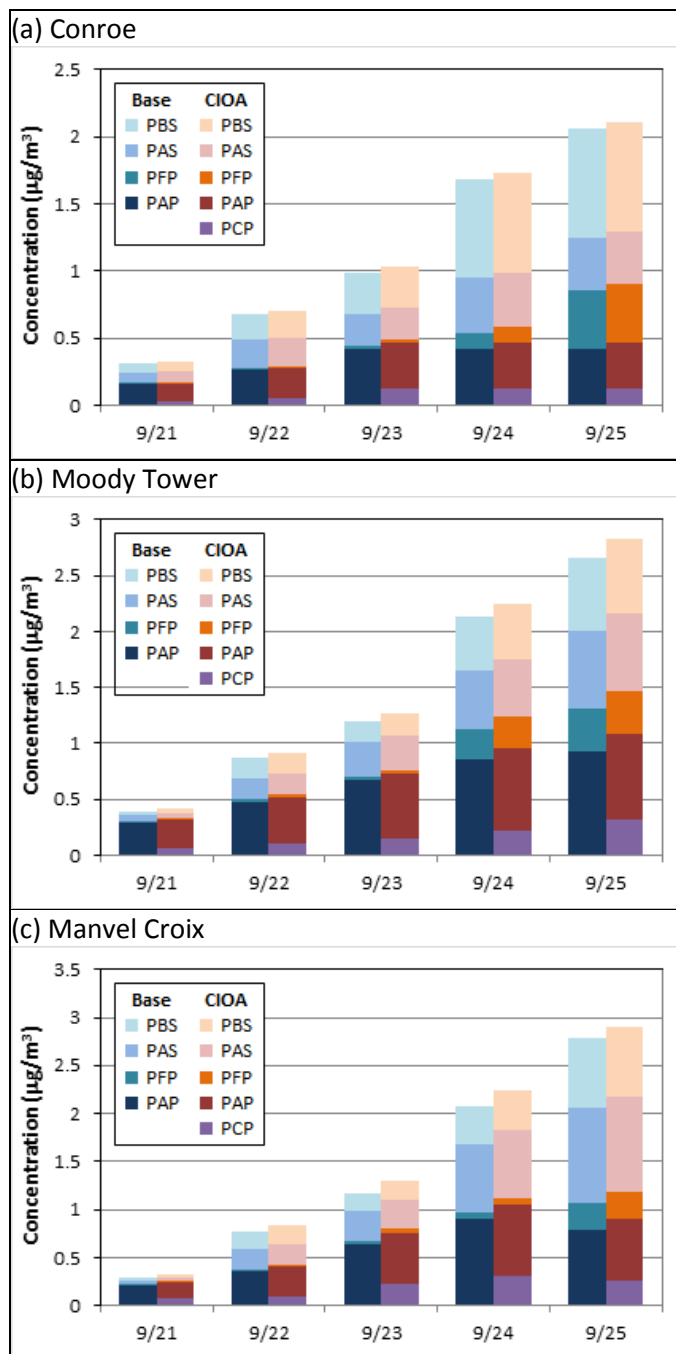


Figure 34. OC concentrations predicted by the base model (Base) and the revised model with CIOA (CIOA) at Conroe, Moody Tower, and Manvel Croix.

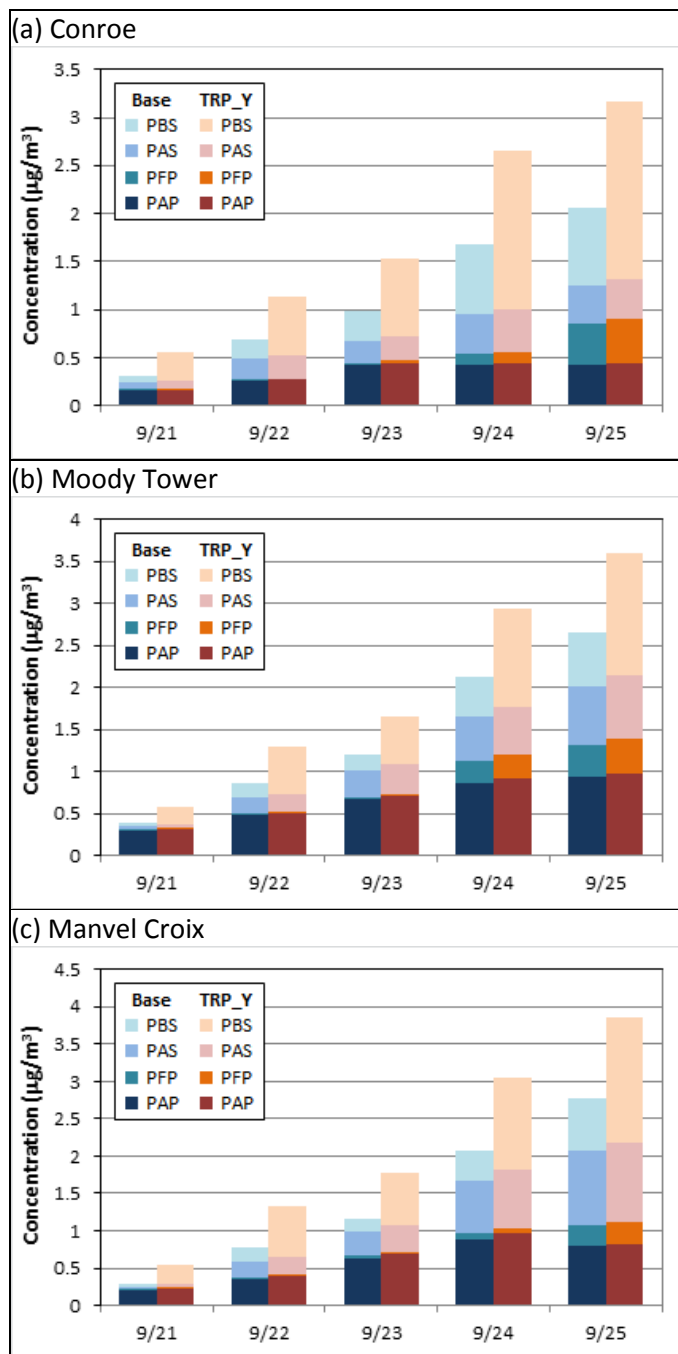


Figure 35. OC concentrations predicted by the base model (Base) and the revised model with updated monoterpene aerosol yields (TRP_Y) at Conroe, Moody Tower, and Manvel Croix.

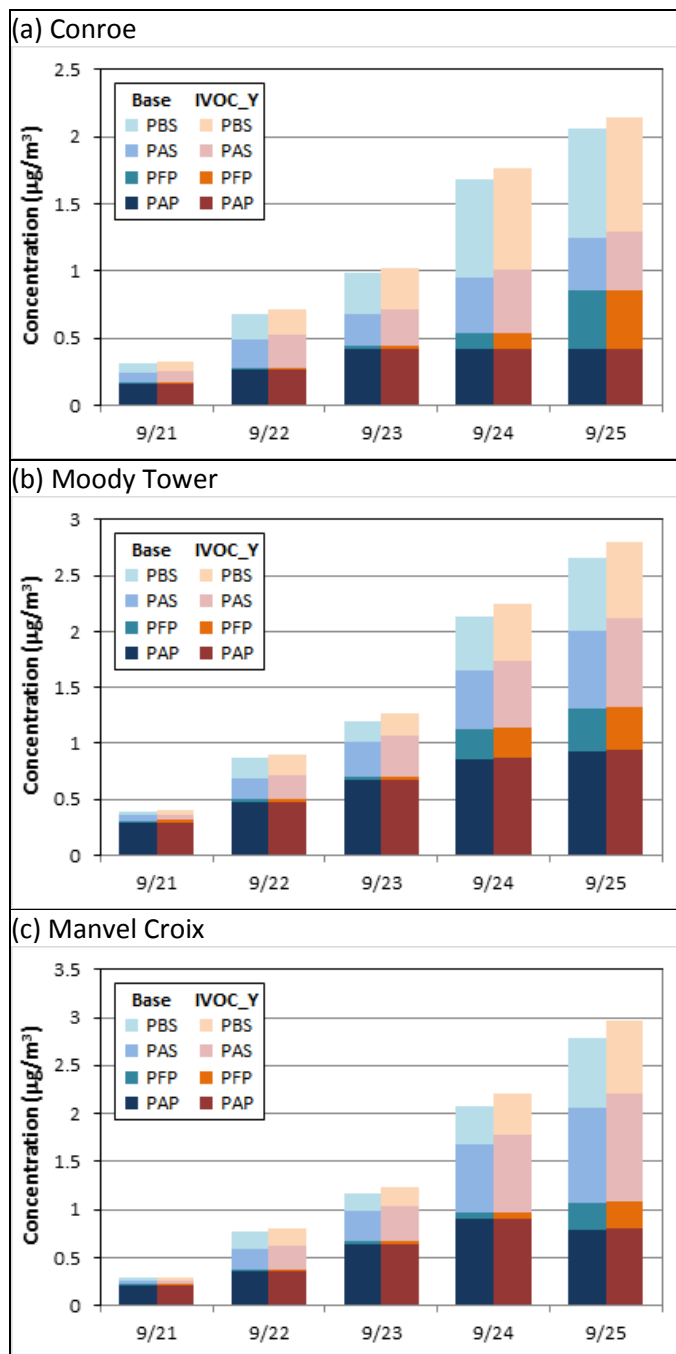


Figure 36. OC concentrations predicted by the base model (Base) and the revised model with adjusted IVOC aerosol yields (IVOC_Y) at Conroe, Moody Tower, and Manvel Croix.

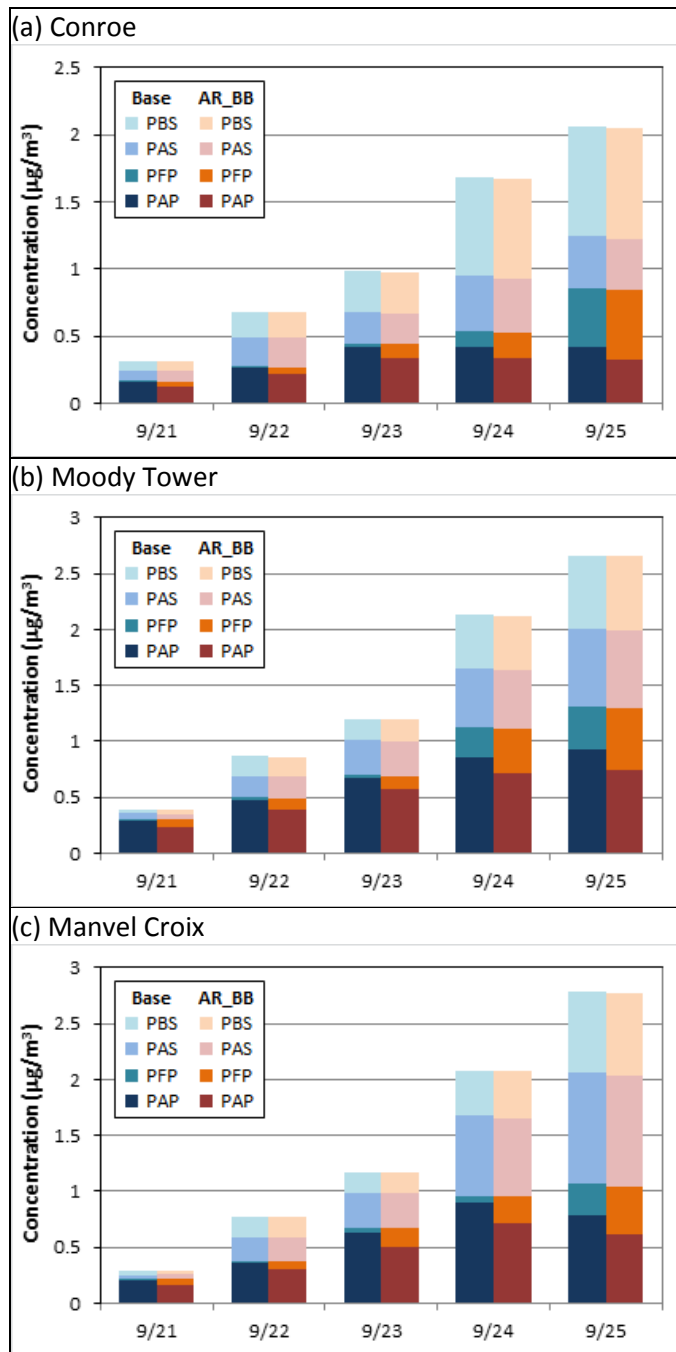


Figure 37. OC concentrations predicted by the base model (Base) and the revised model with fixed biomass burning POA emissions from area sources (AR_BB) at Conroe, Moody Tower, and Manvel Croix.

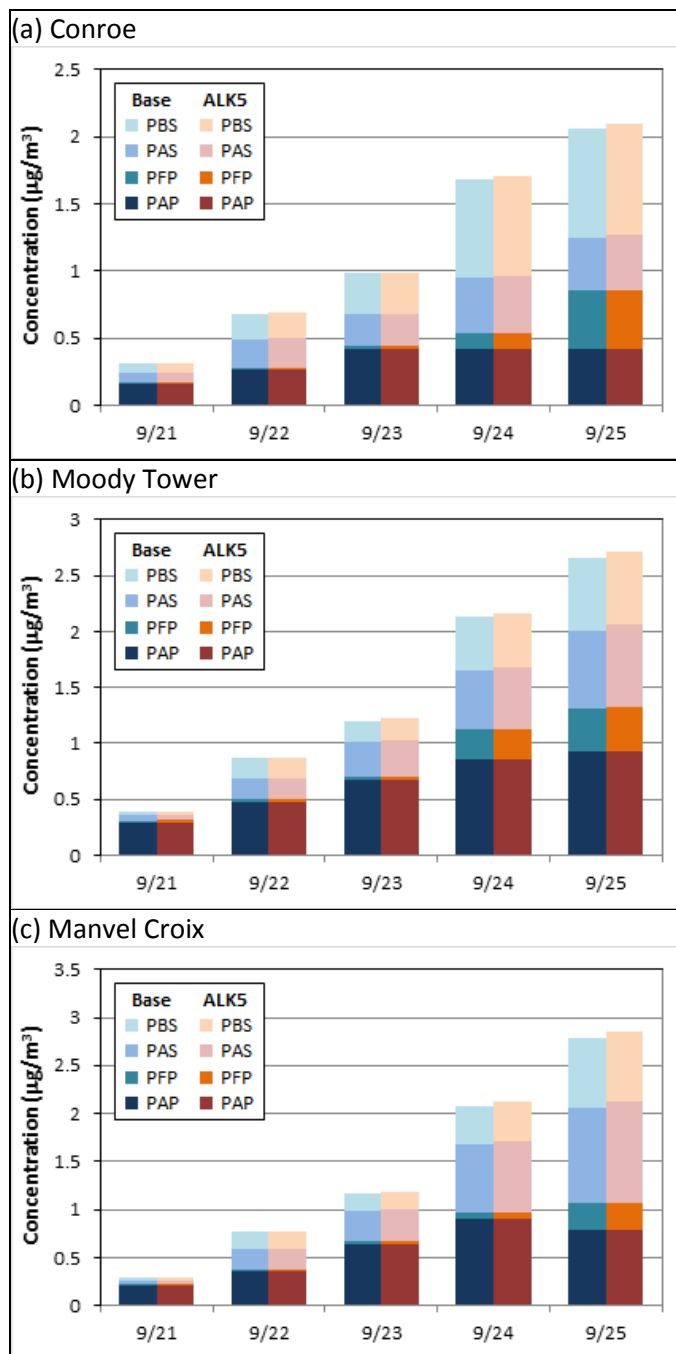


Figure 38. OC concentrations predicted by the base model (Base) and the revised model with SOA formation from long alkane VOC precursor (ALK5) at Conroe, Moody Tower, and Manvel Croix.

8.7 Evaluation of the Revised Model Performance

A revised model with all the improvements described in Section 8.6 was applied to the full base case scenario. The same model performance evaluation as done for the original base case modeling was conducted for the revised model results.

Figure 39 compares observed and modeled OC concentrations (similar to the OC panels of Figures 23 to 25). The revised model shows much better agreement with observations in mid-September while still underestimating the late September peaks at Moody Tower and Manvel Croix. Overall, the revised model significantly reduced the OC underestimation biases of the base model at Moody Tower and Manvel Croix and changed the sign of the biases (from large negative biases to small positive biases) at Conroe (Table 14).

Figure 40 compares hourly PM_{2.5} OA concentrations by the revised model with the ACSM PM₁ OA data at Conroe (similar to Figure 27). The revised model still underestimates the ACSM-measured OA, but with reduced bias and error (the normalized mean bias was reduced from -67% to -43% , and the normalized mean error was reduced from 70% to 54%).

Figure 41 shows average diurnal profiles of PM_{2.5} OA and O:C ratio predicted by the revised model at Conroe (similar to Figure 28 (b) and Figure 29 (b)). The revised model produced similar OA diurnal profile to that of the base model but with increased nighttime OA formation. The revised model yields the range of O:C ratios (0.4 ~ 0.6) more comparable to that of observed values (0.5 ~ 0.8) than the base model (0.3 ~ 0.5), but still lacks the observed O:C increase in the afternoon.

The revised model also gives better agreement with the PMF factor analysis. Figure 42 shows hourly time-series and average diurnal profile of modeled OA composition (similar to Figure 30 (b) and Figure 31 (b)). Average OOA fraction by the revised model (80%) is much closer to the PMF-based fraction (85%) than that of the base model (68%). Increasing HOA fraction in the morning rush hour is less pronounced with the revised model than with the base model.

Figure 43 compares contemporary carbon fractions predicted by the revised model with those of the filter samples estimated by radiocarbon analysis (similar to the right panels of Figure 32). The revised model shows much better agreement with the observed contemporary carbon fractions than the base model.

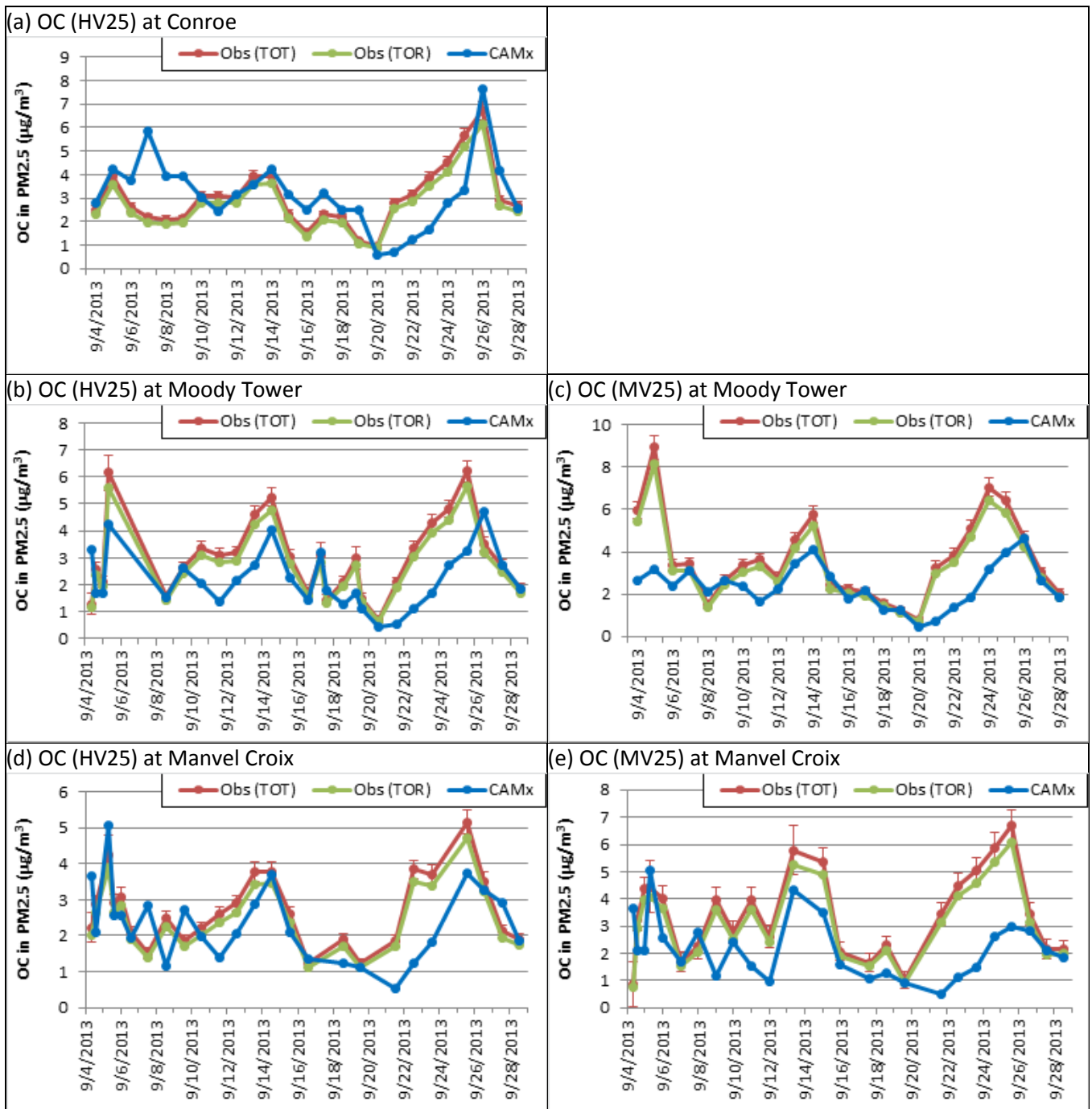


Figure 39. Modeled vs. observed OC concentrations at Conroe, Moody Tower and Manvel Croix during September 2013; the modeled OC concentrations were obtained from the revised model simulation; see Section 8.1 for description of the observed OC data.

Table 14. Performance metrics^a of revised model OC concentrations against filter measurements (the base model performance metrics are given in parentheses).

Site	Sampler	TOT					TOR				
		MO	MB	ME	NMB	NME	MO	MB	ME	NMB	NME
Conroe	HV2.5	3.0	0.17 (-1.2)	1.1 (1.2)	5.6% (-38%)	37% (41%)	2.7	0.43 (-0.89)	1.2 (1.0)	16% (-32%)	42% (37%)
Moody Tower	HV2.5	3.0	-0.82 (-1.5)	1.1 (1.5)	-27% (-49%)	36% (51%)	2.7	-0.56 (-1.2)	0.94 (1.3)	-20% (-44%)	34% (47%)
	MV2.5	3.7	-1.3 (-2.0)	1.4 (2.0)	-35% (-55%)	37% (55%)	3.3	-1.0 (-1.7)	1.1 (1.7)	-29% (-51%)	34% (51%)
Manvel Croix	HV2.5	2.7	-0.40 (-1.1)	0.82 (1.1)	-15% (-40%)	30% (42%)	2.5	-0.16 (-0.85)	0.71 (0.96)	-6.5% (-34%)	29% (39%)
	MV2.5	3.4	-1.3 (-1.9)	1.6 (2.0)	-37% (-55%)	46% (58%)	3.1	-1.0 (-1.6)	1.3 (1.7)	-31% (-50%)	43% (54%)

^a See Table 11 for definitions of performance metrics

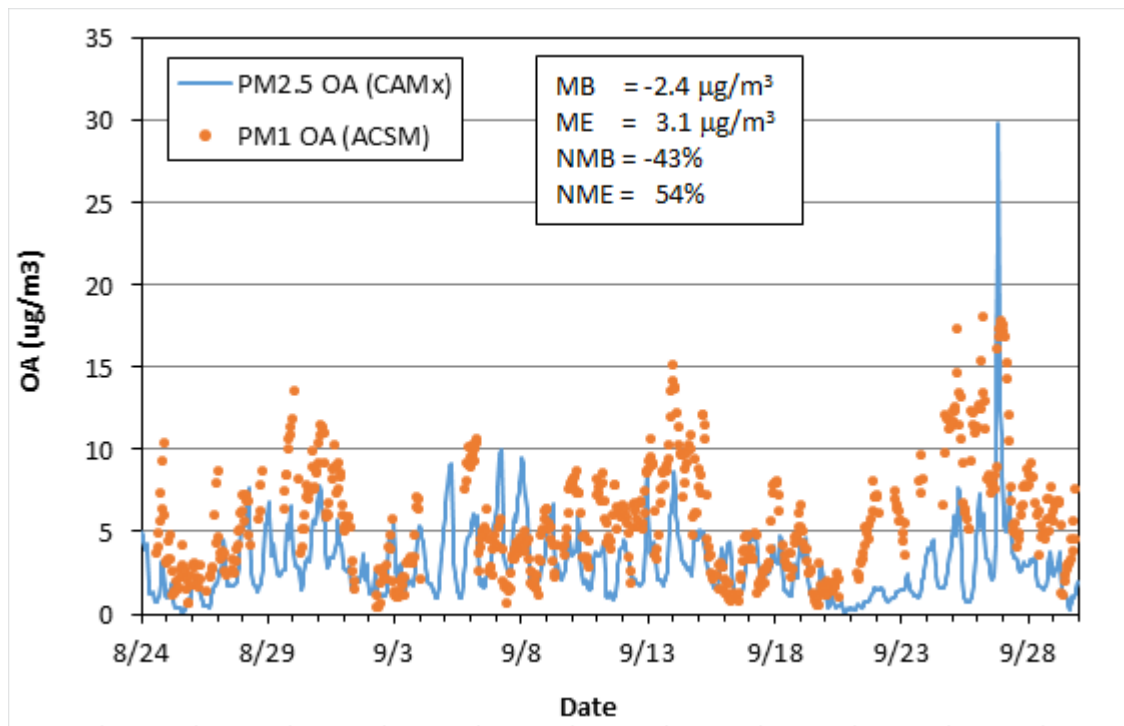
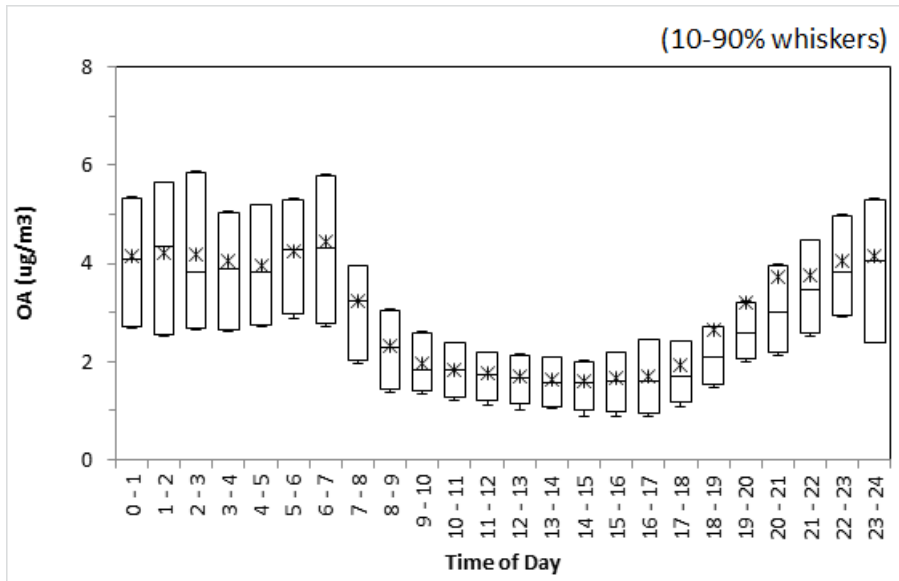


Figure 40. Hourly PM2.5 OA concentrations by the revised model and ACSM measurements of PM1 OA at Conroe.

(a) PM2.5 OA (revised model)



(b) O:C ratios (revised model)

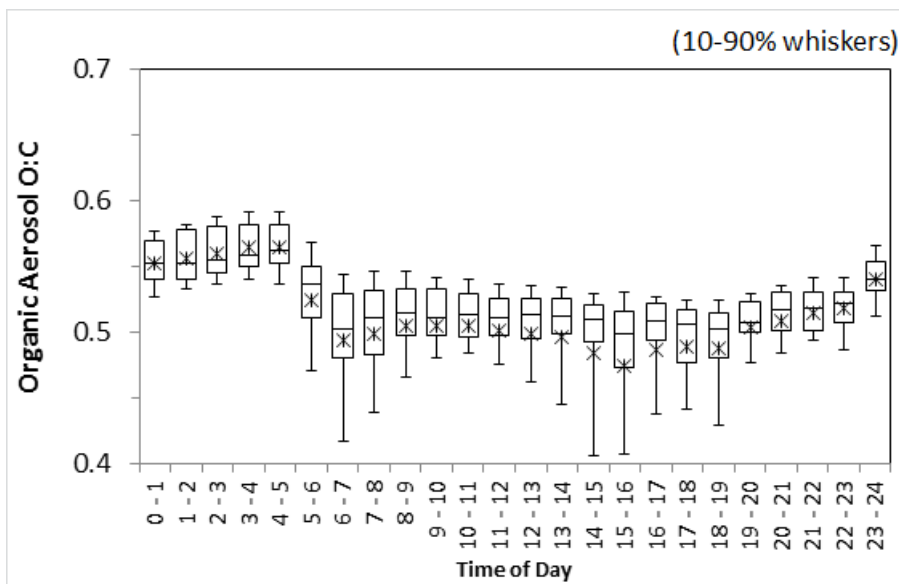
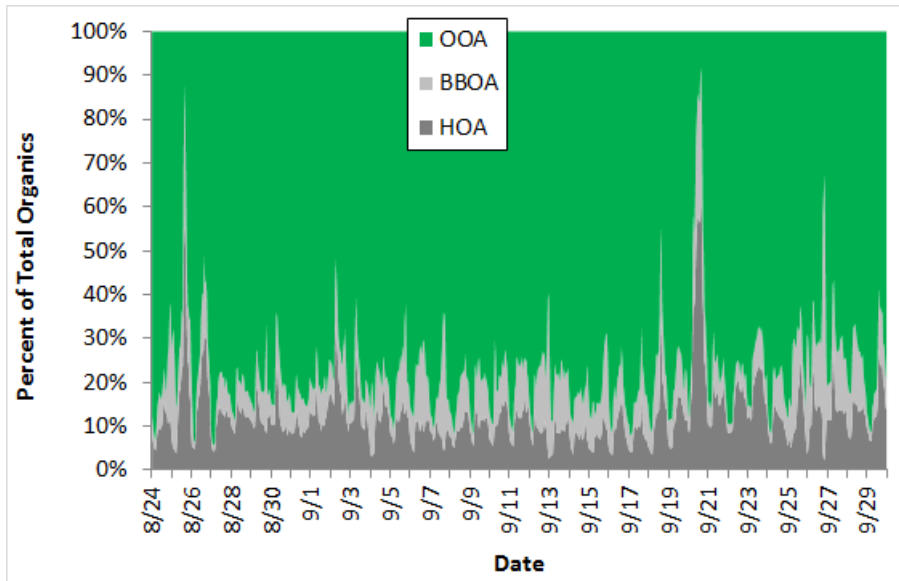


Figure 41. Box and whisker plots of diurnal cycles of modeled OA concentrations and O:C ratios at Conroe.

(a) Hourly OA composition (revised model)



(b) Average diurnal profile of OA composition (revised model)

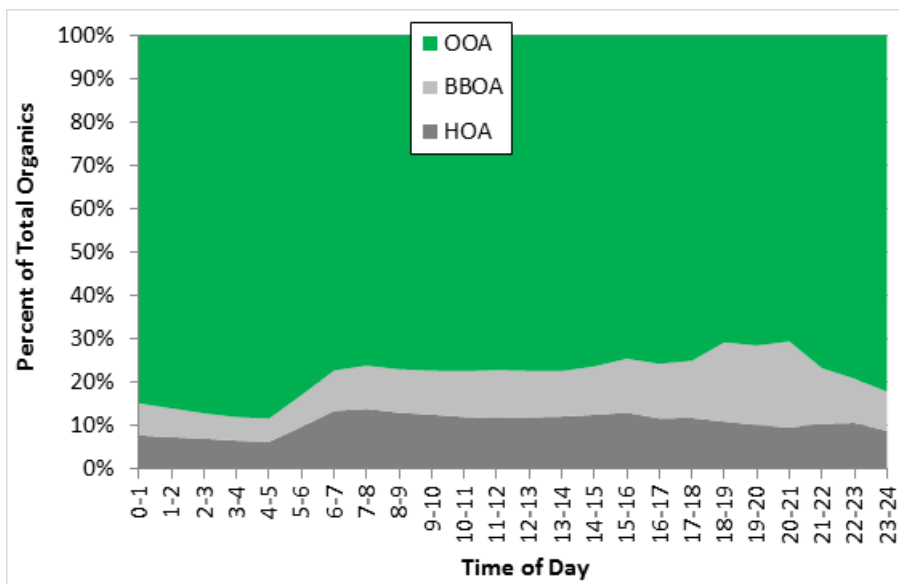


Figure 42. Hourly OA composition and average diurnal cycle of OA composition predicted by the revised model.

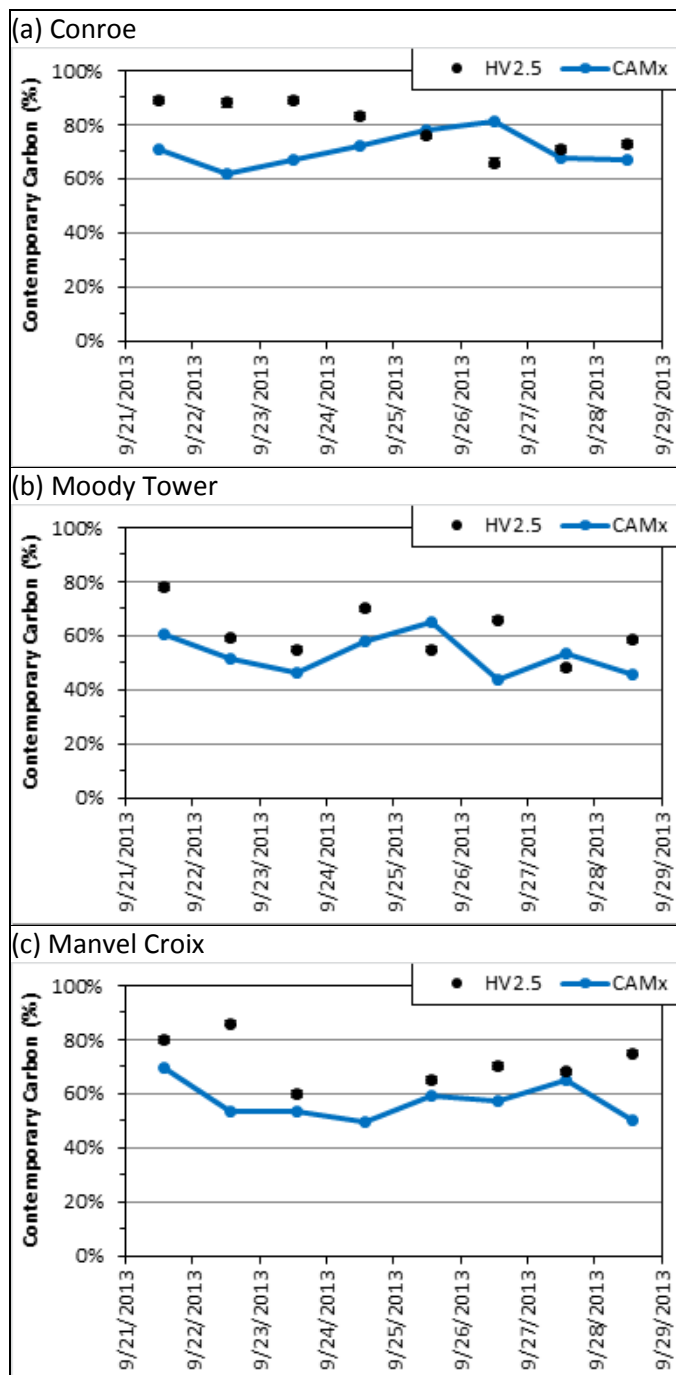


Figure 43. Contemporary carbon fractions estimated by radiocarbon analysis on the high volume filter samples (HV2.5) and predicted by the revised model (CAMx) at Conroe, Moody Tower, and Manvel Croix.

9.0 Audits of Data Quality

Data from the environmental chamber experiments were first analyzed by Surya Dhulipala, a Graduate Research Assistant (GRA) in the research group of Dr. Hildebrandt Ruiz. All data were then audited by Dr. Hildebrandt Ruiz. This audit consisted of a detailed review of all data analysis procedures and intermediate steps in the calculation of final values presented in this report.

The ACSM data collected during DISCOVER-AQ, which are the focus of this work, were analyzed separately by two researchers: PI Dr. Hildebrandt Ruiz and Jeffrey Bean, a GRA in Dr. Hildebrandt Ruiz's research group. The results from these two separate analyzes agreed perfectly as expected when the same procedures are followed and no mistakes are made. The SEMS data collected during DISCOVER-AQ, which are used for comparison here, were also analyzed separately by two researchers (GRA Jeffrey Bean and GRA Cameron Faxon), and the final values agreed. The analysis of inorganic ions from filter samples was performed by the Desert Research Institute (DRI) and followed the standard, audited DRI quality control procedures.

The CAMx base case modeling input database (meteorological inputs, model-ready emission inputs, initial and boundary conditions, etc.) was prepared by Ramboll Environ technical staff members (DJ Rasmussen, Michele Jimenez, and Jaegun Jung). All the model input data was then audited by Ramboll Environ senior technical staff members (meteorological inputs by Jeremiah Johnson; emissions and other inputs by Dr. Bonyoung Koo).

The model simulation and model performance evaluation were conducted by Jaegun Jung. The modeling and performance evaluation procedure was reviewed by Dr. Bonyoung Koo. The model performance evaluation results were analyzed separately by Drs. Bonyoung Koo and Greg Yarwood.

10.0 Conclusions and Recommendations

Sixteen laboratory chamber experiments were conducted to form SOA from the oxidation of different intermediate volatility organic compounds (IVOCs). Out of the six IVOCs studied (n-pentadecane, 2,6,10-trimethyldodecane, 2-methylnaphthalene, butyl CARBITOL™, Texanol™, and mineral spirits), all but Texanol™ formed secondary organic aerosol. SOA mass yields of 2-methylnaphthalene measured in this study agreed well with literature data. A novel contribution of this work is quantification of the SOA yield from butyl CARBITOL™, a glycol ether used in surface coatings. The SOA yields from this compound were similar to yields from 2-methylnaphthalene. The vapor pressure of SOA formed from n-pentadecane, 2,6,10-trimethyldodecane and mineral spirits was analyzed using a thermodenuder developed as part of this work. The SOA formed from mineral spirits was more volatile than the SOA formed from n-pentadecane and 2,6,10-trimethyldodecane (a branched pentadecane).

Ambient data collected during the DISCOVER-AQ campaign were analyzed focusing on the concentrations and composition of fine particulate matter. The data were obtained at an air quality monitoring ground site in Conroe, TX (30.350278°N, 95.425000°W) located approximately 60 km NNW from the Houston, TX urban center and approximately 125 km NW of the nearest coastline. On average 65% percent of the non-refractory PM₁ mass was due to organic material (including organic nitrates), highlighting the importance of organics in controlling fine PM mass in the Houston region. Positive matrix factorization analysis (PMF) was applied to the organic aerosol mass spectra measured by the ACSM. The data were best represented by two factors of oxygenated organic aerosol (OOA), a more oxidized OOA (MO-OOA) and a less oxidized OOA (LO-OOA), as well as a fresher factor representative of hydrocarbon like organic aerosol (HOA) and biomass burning organic aerosol (BBOA). According to this analysis on average 85% of the organic aerosol sampled at Conroe consisted of oxygenated organic aerosol, highlighting the importance of atmospheric processing in influencing concentrations of organic particulate matter in the Houston region.

The Comprehensive Air quality Model with Extensions (CAMx) utilizing the 1.5 dimensional volatility basis set (1.5-D VBS) was applied to simulate organic aerosol formation in the Houston region during the 2013 DISCOVER-AQ campaign. Emissions of intermediate volatility organic compounds (IVOC) from major combustion sources were added using IVOC fractions of total non-methane organic gas (NMOG) emissions estimated from environmental chamber studies. The model results were evaluated against PM_{2.5} filter measurements at Conroe, Moody Tower and Manvel Croix and PM₁ ACSM measurements at Conroe. The base model generally underpredicts the observed total organic carbon (OC) concentrations and PMF-estimated OOA fractions. The radio carbon analysis indicates that the base model underestimates contemporary carbon fractions while the modeled fossil carbon mass is comparable to observations.

Several improvements were made to the base model: a basis set for cooking-influenced organic aerosol was added, the organic aerosol mass yields from the reactions of monoterpenes and NO₃

were updated, the organic aerosol mass yields of IVOC precursors were adjusted, an error in the emissions of primary organic aerosol from biomass burning area sources was corrected and the formation of secondary organic aerosol from long alkane precursors (8-11 carbons) was added. The base case scenario was simulated again with the revised model. The results show that the revised model gives much better agreement than the base model with the measured OC concentrations, PMF-based OOA fractions, and contemporary carbon fractions by radiocarbon analysis.

The supplemental measurements in the evaluation database (including filter OC and radiocarbon analysis data, ACSM measurements and PMF analysis) were very useful in guiding model improvements and providing a more informative evaluation. This project greatly benefited from the AQRP projects 14-024 and 14-029 that collected these data.

Uncertainty in the sources of secondary organic aerosol adds substantial uncertainty in understanding the sources of PM_{2.5}. We make the following recommendations for additional environmental chamber experiments, ambient measurements and modeling activities to support improvements in the representation of organic aerosol in chemical transport models which are used for policy making:

- Environmental chamber experiments to evaluate systematically the mass yields of SOA formed from IVOCs from non-combustion sources – we initiated this work as part of this project by evaluating the SOA formation from two oxygenated IVOCs used in surface coatings (TexanolTM and butyl CARBITOLTM.)
- Environmental chamber experiments to evaluate systematically the effect of relative humidity on the mass yields of SOA formed from various different precursors – most yield parameters used in models are from experiments conducted at low relative humidity, which is not representative of conditions in Houston and many other regions in Texas.
- Ambient measurements of detailed PM composition and concentration at several locations within the same region to provide additional insights into sources of ambient PM and additional data for model evaluation – the ambient data collected during DISCOVER-AQ was very useful for the model evaluation conducted as part of this project.
- Ambient measurements in Texas during the winter to provide insights into sources of ambient PM and data for model comparisons under different meteorological conditions – most ambient measurement campaigns in Texas and other regions of the United States are conducted during the summer, which can create a bias.
- Update the CAMx VBS model to include an additional basis set for tracking CIOA (cooking influenced organic aerosol) emissions.

- Separately prepare IVOC emissions from gasoline and diesel combustion sources and biomass burning through the emission inventory processing – this may require updating the emission processors.
- Separately prepare POA emissions from meat cooking as well as gasoline/diesel engines and biomass burning through the emission inventory processing – this may require updating the emission processors.
- Estimate IVOC emissions from non-combustion sources.
- Systematically evaluate model sensitivity to SOA yields. Our modeling has shown that SOA yields for monoterpene reactions with NO_3 radical have a large impact on SOA formation.
- Evaluate the model treatment for aging of biogenic SOA – chemical aging of biogenic SOA is disabled in our VBS implementation based on findings from previous modeling studies. However, the model evaluation results in this study imply that the model may underestimate biogenic SOA in the Houston area which could be mitigated by including chemical aging of biogenic SOA. Alternatively, some biogenic SOA formation pathways may be missing from our VBS scheme.

11.0 References

- Aiken, A. C., DeCarlo, P. F., Kroll, J. H., Worsnop, D. R., Huffman, J. A., Docherty, K., Ulbrich, I. M., Mohr, C., Kimmel, J. R., Sueper, D., Sun, Y., Zhang, Q., Trimborn, A. M., Northway, M. J., Ziemann, P. J., Canagaratna, M. R., Alfarra, M. R., Prevot, A. S. H., Dommen, J., Duplissy, J., Metzger, A., Baltensperger, U. and Jimenez, J. L.: O/C and OM/OC Ratios of Primary, Secondary, and Ambient Organic Aerosols with High Resolution Time-of-Flight Aerosol Mass Spectrometry, *Environ. Sci. Technol.*, 42, 4478–4485, 2008.
- Aimanant, S. and Ziemann, P. J.: Chemical Mechanisms of Aging of Aerosol Formed from the Reaction of n -Pentadecane with OH Radicals in the Presence of NO_x, *Aerosol Sci. Technol.*, 47(9), 979–990, doi:10.1080/02786826.2013.804621, 2013.
- Aljawhary, D., Lee, A. K. Y. and Abbatt, J. P. D.: High-resolution chemical ionization mass spectrometry (ToF-CIMS): application to study SOA composition and processing, *Atmos. Meas. Tech.*, 6(11), 3211–3224, doi:10.5194/amt-6-3211-2013, 2013.
- Allan, J. D., Delia, A. E., Coe, H., Bower, K. N., Alfarra, M. R., Jimenez, J. L., Middlebrook, A. M., Drewnick, F., Onasch, T. B., Canagaratna, M. R., Jayne, J. T. and Worsnop, D. R.: A generalised method for the extraction of chemically resolved mass spectra from Aerodyne aerosol mass spectrometer data, *J. Aerosol Sci.*, 35(7), 909–922, doi:10.1016/j.jaerosci.2004.02.007, 2004.
- Allen, D.: Gulf Coast Aerosol Research and Characterization Program (Houston Supersite), Final Report to the U.S. Environmental Protection Agency, Cooperative Agreement No. R-82806201, 1–40, 2005.
- Atkinson-Palombo, C. M., Miller, J. A. and Balling Jr., R. C.: Quantifying the ozone “weekend effect” at various locations in Phoenix, Arizona, *Atmos. Environ.*, 40, 7644–7658, 2006.
- Bahreini, R., Ervens, B., Middlebrook, a. M., Warneke, C., de Gouw, J. a., DeCarlo, P. F., Jimenez, J. L., Brock, C. a., Neuman, J. a., Ryerson, T. B., Stark, H., Atlas, E., Brioude, J., Fried, a., Holloway, J. S., Peischl, J., Richter, D., Walega, J., Weibring, P., Wollny, a. G. and Fehsenfeld, F. C.: Organic aerosol formation in urban and industrial plumes near Houston and Dallas, Texas, *J. Geophys. Res.*, 114, 1–17, doi:10.1029/2008JD011493, 2009.
- Barsanti, K. C., Carlton, a. G. and Chung, S. H.: Analyzing experimental data and model parameters: Implications for predictions of SOA using chemical transport models, *Atmos. Chem. Phys.*, 13(23), 12073–12088, doi:10.5194/acp-13-12073-2013, 2013.
- Bertram, T. H., Kimmel, J. R., Crisp, T. a., Ryder, O. S., Yatavelli, R. L. N., Thornton, J. a., Cubison, M. J., Gonin, M. and Worsnop, D. R.: A field-deployable, chemical ionization time-of-flight mass spectrometer, *Atmos. Meas. Tech.*, 4(7), 1471–1479, doi:10.5194/amt-4-1471-2011, 2011.
- Boyd, C. M., Sanchez, J., Xu, L., Eugene, a. J., Nah, T., Tuet, W. Y., Guzman, M. I. and Ng, N. L.: Secondary organic aerosol formation from the β-pinene+NO₃ system: effect of humidity and peroxy radical fate, *Atmos. Chem. Phys.*, 15(13), 7497–7522, doi:10.5194/acp-15-7497-2015, 2015.

Burtscher, H., Baltensperger, U., Bukowiecki, N., Cohn, P., Hugglin, C., Mohr, M., Matter, U., Nyeki, S., Schmatloch, V., Streit, N. and Weingartner, E.: Separation of volatile and non-volatile aerosol fractions by thermodesorption: Instrumental development and applications, *J. Aerosol Sci.*, 32, 427–442, 2001.

Canagaratna, M. R., Jimenez, J.-L., Kroll, J. H., Chen, Q., Kessler, S. H., Massoli, P., Hildebrandt Ruiz, L., Fortner, E., Williams, L., Wilson, K., Surratt, J. D., Donahue, N. M., Jayne, J. T. and Worsnop, D. R.: Elemental Ratio Measurements of Organic Compounds using Aerosol Mass Spectrometry: Characterization, Improved Calibration, and Implications, *Atmos. Chem. Phys.*, 15, 253–272, 2015.

Carlton, A. G., Bhave, P. V, Napelenok, S. L., Edney, E. O., Pinder, R. W., Pouliot, G. A. and Houyoux, M.: Model Representation of Secondary Organic Aerosol in CMAQv4.7, *Environ. Sci. Technol.*, 44, 8553–8560, 2010.

Chan, A. W. H., Kautzman, K. E., Chhabra, P. S., Surratt, J. D., Chan, M. N., Crouse, J. D., Kürten, A., Wennberg, P. O., Flagan, R. C. and Seinfeld, J. H.: Secondary organic aerosol formation from photooxidation of naphthalene and alkylnaphthalenes: implications for oxidation of intermediate volatility organic compounds (IVOCs), *Atmos. Chem. Phys.*, 9, 3049–3060, 2009.

Donahue, N. M., Robinson, A. L., Stanier, C. O. and Pandis, S. N.: Coupled partitioning, dilution, and chemical aging of semivolatile organics, *Environ. Sci. Technol.*, 40(8), 2635–2643, 2006.

ENVIRON, 2015, User's Guide Comprehensive Air Quality Model with Extensions Version 6.2. <http://www.camx.com>

ENVIRON and ERG, 2013, Technical Support Document: Photochemical Modeling for the Louisiana 8-Hour Ozone State Implementation Plan. Prepared for the Louisiana Department of Environmental Quality, Office of Environmental Services, Air Permits Division, Baton Rouge, LA. Prepared by ENVIRON International Corporation, Novato, CA and Eastern Research Group, Inc., Rancho Cordova, CA.

Gong, S. L.: A parameterization of sea-salt aerosol source function for sub- and super-micron particles. *Global Biogeochemical Cycles* 17: .Gong, S. L., 2003, A parameterization of sea-salt aerosol source function for sub- and super-micron particles., *Global Biogeochem. Cycles*, 17, 1097–1104, 2003.

Guenther, A. B., Jiang, X., Heald, C.L. Sakulyanontvittaya, T., Duhl, T., Emmons, L. K. and Wang, X.: The Model of Emissions of Gases and Aerosols from Nature version 2.1 (MEGAN2.1): an extended and updated framework for modeling biogenic emissions. , 5, 1503-1560., *Geosci. Model Dev.*, 5, 1471–1492, 2012.

Hayes, P. L., Ortega, a. M., Cubison, M. J., Froyd, K. D., Zhao, Y., Cliff, S. S., Hu, W. W., Toohey, D. W., Flynn, J. H., Lefer, B. L., Grossberg, N., Alvarez, S., Rappenglück, B., Taylor, J. W., Allan, J. D., Holloway, J. S., Gilman, J. B., Kuster, W. C., De Gouw, J. a., Massoli, P., Zhang, X., Liu, J., Weber, R. J., Corrigan, a. L., Russell, L. M., Isaacman, G., Worton, D. R., Kreisberg, N. M., Goldstein, a. H., Thalman, R., Waxman, E. M., Volkamer, R., Lin, Y. H., Surratt, J. D., Kleindienst, T. E., Offenberg, J. H., Dusanter, S., Griffith, S., Stevens, P. S., Brioude, J., Angevine, W. M. and Jimenez, J. L.: Organic aerosol composition and sources in

Pasadena, California, during the 2010 CalNex campaign, *J. Geophys. Res. Atmos.*, 118(16), 9233–9257, doi:10.1002/jgrd.50530, 2013.

Hildebrandt, L., Donahue, N. M. and Pandis, S. N.: High formation of secondary organic aerosol from the photo-oxidation of toluene, *Atmos. Chem. Phys.*, (9), 2973–2986, 2009.

Hildebrandt, L., Engelhart, G. J., Mohr, C., Kostenidou, E., Lanz, V. A., Bougiatioti, A., DeCarlo, P. F., Prevot, A. S. H., Baltensperger, U., Mihalopoulos, N., Donahue, N. M. and Pandis, S. N.: Aged organic aerosol in the Eastern Mediterranean: The Finokalia Aerosol Measurement Experiment – 2008, *Atmos. Chem. Phys.*, 10, 4167–4186, 2010.

Hildebrandt, L., Kostenidou, E., Lanz, V. A., Prevot, A. S. H., Baltensperger, U., Mihalopoulos, N., Donahue, N. M. and Pandis, S. N.: Sources and atmospheric processing of organic aerosol in the Mediterranean: Insights from Aerosol Mass Spectrometer Factor Analysis, *Atmos. Chem. Phys.*, 11, 12499–12515, 2011.

Hildebrandt Ruiz, L. and Yarwood, G.: Interactions between Organic Aerosol and NO_y: Influence on Oxidant Production, Austin, TX. Prepared for the Texas AQRP (Project 12-012), by the University of Texas at Austin, and ENVIRON International Corporation, Novato, CA. http://aqrp.ceer.utexas.edu/projectinfoFY12_13/12-012/12-012%20Final%20Report.pdf, 2013.

Huffman, J. A., Docherty, K. S., Aiken, A. C., Cubison, M. J., Ulbrich, I. M., DeCarlo, P. F., Sueper, D., Jayne, J. T., Worsnop, D. R., Ziemann, P. J. and Jimenez, J. L.: Chemically-resolved aerosol volatility measurements from two megacity field studies, *Atmos. Chem. Phys.*, 9, 7161–7182, 2009.

Huffman, J. A., Ziemann, P. J., Jayne, J. T., Worsnop, D. R. and Jimenez, J. L.: Development and characterization of a fast-stepping/scanning thermodesorber for chemically-resolved aerosol volatility measurements, *Aerosol Sci. Technol.*, 42, 395–407, 2008.

Jathar, S. H., Gordon, T. D., Hennigan, C. J., Pye, H. O. T., Pouliot, G., Adams, P. J., Donahue, N. M. and Robinson, A. L.: Unspeciated organic emissions from combustion sources and their influence on the secondary organic aerosol budget in the United States, *Proc. Natl. Acad. Sci.*, 111, 10473–10478, 2014.

Johnson, J., Karamchandani, P., Wilson, G. and Yarwood, G.: TCEQ Ozone Forecasting System, Prepared for Mark Estes., 2013.

Kain, J. S.: The Kain-Fritsch convective parameterization: An update., *J. Appl. Meteor.*, 43, 170–181, 2004.

Karnezi, E., Riipinen, I. and Pandis, S. N.: Measuring the atmospheric organic aerosol volatility distribution: a theoretical analysis, *Atmos. Meas. Tech. Discuss.*, 7(1), 859–893, doi:10.5194/amtd-7-859-2014, 2014.

Kebabian, P. L., Wood, E. C., Herndon, S. C. and Freedman, A.: A Practical Alternative to Detection of Nitrogen Dioxide : Cavity Attenuated Phase Shift Spectroscopy, *Environ. Sci. Technol.*, 42(16), 6040–6045, doi:10.1021/es703204j, 2008.

Koo, B., Knipping, E. and Yarwood, G.: 1.5-Dimensional volatility basis set approach for modeling organic aerosol in CAMx and CMAQ, *Atmos. Environ.*, 95, 158–164, 2014.

Kostenidou, E., Pathak, R. K. and Pandis, S. N.: An Algorithm for the Calculation of Secondary Organic Aerosol Density Combining AMS and SMPS Data, *Aerosol Sci. Technol.*, 41(11), 1002–1010, doi:10.1080/02786820701666270, 2007.

Lane, T. E., Donahue, N. M. and Pandis, S. N.: Simulating secondary organic aerosol formation using the volatility basis-set approach in a chemical transport model, *Atmos. Environ.*, 42, 7439–7451, 2008.

Lanz, V. A., Alfarra, M. R., Baltensperger, U., Buchmann, B., Hueglin, C. and Prevot, A. S. H.: Source apportionment of submicron organic aerosols at an urban site by factor analytical modelling of aerosol mass spectra, *Atmos. Chem. Phys.*, 7, 1503–1522, 2007.

Lanz, V. a., Prévôt, a. S. H., Alfarra, M. R., Mohr, C., DeCarlo, P. F., Weimer, S., Gianini, M. F. D., Hueglin, C., Schneider, J., Favez, O., D'Anna, B., George, C. and Baltensperger, U.: Characterization of aerosol chemical composition by aerosol mass spectrometry in Central Europe: an overview, *Atmos. Chem. Phys. Discuss.*, 9(6), 24985–25021, doi:10.5194/acpd-9-24985-2009, 2009.

Lee, B. H., Lopez-Hilfiker, F. D., Mohr, C., Kurtén, T., Worsnop, D. R. and Thornton, J. a: An iodide-adduct high-resolution time-of-flight chemical-ionization mass spectrometer: application to atmospheric inorganic and organic compounds., *Environ. Sci. Technol.*, 48(11), 6309–17, doi:10.1021/es500362a, 2014.

De Leeuw, G., Neele, F. P., Hill, M., Smith, M. H. and Vignati, E.: Production of sea spray aerosol in the surf zone, *J. Geophys. Res.*, 105, 29397–29409, 2000.

Li, J.: Implementation and Application of SAPRC07 and MCM Mechanisms in the Community Multi-Scale Air Quality Model, Texas A&M University. 2010.

Lim, Y. B. and Ziemann, P. J.: Effects of molecular structure on aerosol yields from OH radical-initiated reactions of linear, branched, and cyclic alkanes in the presence of NO_x., *Environ. Sci. Technol.*, 43(7), 2328–2334, 2009.

Middlebrook, A. M., Bahreini, R., Jimenez, J. L. & Canagaratna, M. R. Evaluation of Composition-Dependent Collection Efficiencies for the Aerodyne Aerosol Mass Spectrometer using Field Data. *Aerosol Sci. Technol.*, 46, 258–271, 2012.

Murphy, B. N. and Pandis, S. N.: Simulating the Formation of Semivolatile Primary and Secondary Organic Aerosol in a Regional Chemical Transport Model, *Environ. Sci. Technol.*, 43(11), 4722–4728, 2009.

Ng, N. L., Canagaratna, M. R., Zhang, Q., Jimenez, J. L., Tian, J., Ulbrich, I. M., Kroll, J. H., Docherty, K. S., Chhabra, P. S., Bahreini, R., Murphy, S. M., Seinfeld, J. H., Hildebrandt, L., Donahue, N. M., DeCarlo, P. F., Lanz, V. A., Prevot, A. S. H., Dinar, E., Rudich, Y. and Worsnop, D. R.: Organic aerosol components observed in northern hemispheric datasets from aerosol mass spectrometry, *Atmos. Chem. Phys.*, 10, 4625–4641, 2010.

Ng, N. L., Herndon, S. C., Trimborn, a., Canagaratna, M. R., Croteau, P. L., Onasch, T. B., Sueper, D., Worsnop, D. R., Zhang, Q., Sun, Y. L. and Jayne, J. T.: An Aerosol Chemical Speciation Monitor (ACSM) for Routine Monitoring of the Composition and Mass Concentrations of Ambient Aerosol, *Aerosol Sci. Technol.*, 45(7), 780–794, doi:10.1080/02786826.2011.560211, 2011.

Paatero, P. and Tapper, U.: Positive Matrix Factorization: a nonnegative factor model with optimal utilization of error estimates of data values, *Environmetrics*, 5, 111–126, 1994.

Pacific Environmental Services: Development of Source Speciation Profiles from the TNRCC 2000 Point Source Database. Report prepared for the Texas Natural Resource Conservation Commission by Pacific Environmental Services under subcontract to ENVIRON, 2001.

Pankow, J. F.: An Absorption-Model Of Gas-Particle Partitioning Of Organic-Compounds In The Atmosphere, *Atmos. Environ.*, 28(2), 185–188, 1994.

Pankow, J. F., Seinfeld, J. H., Asher, W. E. and Erdakos, G. B.: Modeling the formation of secondary organic aerosol. 1. Application of theoretical principles to measurements obtained in the alpha-pinene/, beta-pinene/, sabinene/, Delta(3)-carene/, and cyclohexene/ozone systems, *Environ. Sci. Technol.*, 35(6), 1164–1172, 2001.

Presto, A. a, Miracolo, M. a, Donahue, N. M. and Robinson, A. L.: Secondary organic aerosol formation from high-NO(x) photo-oxidation of low volatility precursors: n-alkanes., *Environ. Sci. Technol.*, 44(6), 2029–34, doi:10.1021/es903712r, 2010.

Riipinen, I., Pierce, J. R., Donahue, N. M. and Pandis, S. N.: Equilibration time scales of organic aerosol inside thermodenuders: Evaporation kinetics versus thermodynamics, *Atmos. Environ.*, 44, 597–607, doi:10.1016/j.atmosenv.2009.11.022, 2010.

Robinson, A. L., Donahue, N. M., Shrivastava, M. K., Weitkamp, E. a, Sage, A. M., Grieshop, A. P., Lane, T. E., Pierce, J. R. and Pandis, S. N.: Rethinking organic aerosols: semivolatile emissions and photochemical aging., *Science*, 315(5816), 1259–62, doi:10.1126/science.1133061, 2007.

Skamarock, W.C., J.B. Klemp, J. Dudhia, D.O. Gill, D.M. Barker, M.G. Duda, X.-Y. Huang, W. Wang, J.G. Powers, A Description of the Advanced Research WRF Version 3. Prepared by the National Center for Atmospheric Research, NCAR Technical Note NCAR/TN-475+STR, 2008.

Shrivastava, M. K., Lane, T. E., Donahue, N. M., Pandis, S. N. and Robinson, A. L.: Effects of gas particle partitioning and aging of primary emissions on urban and regional organic aerosol concentrations, *J. Geophys. Res.*, 113(D18), D18301, doi:10.1029/2007JD009735, 2008.

Strader, R., Lurmann, F. and Pandis, S. N.: Evaluation of secondary organic aerosol formation in winter, *Atmos. Environ.*, 33, 4849–4863, 1999.

Tkacik, D. S., Presto, A. a, Donahue, N. M. and Robinson, A. L.: Secondary organic aerosol formation from intermediate-volatility organic compounds: cyclic, linear, and branched alkanes., *Environ. Sci. Technol.*, 46(16), 8773–8781, 2012.

Ulbrich, I. M., Canagaratna, M. R., Zhang, Q., Worsnop, D. R. and Jimenez, J. L.: Interpretation of organic components from Positive Matrix Factorization of aerosol mass spectrometric data, *Atmos. Chem. Phys.*, 9, 2891–2918, 2009.

United States Environmental Protection Agency: National Ambient Air Quality Standards for Particulate Matter; Final Rule, *Fed. Regist.*, 78(10) [online] Available from: <http://www.gpo.gov/fdsys/pkg/FR-2013-01-15/pdf/2012-30946.pdf>, 2013.

Wehner, B., Philippin, S. and Wiedensohler, A.: Design and calibration of a thermodenuder with an improved heating unit to measure the size-dependent volatile fraction of aerosol particles, *J. Aerosol Sci.*, 33, 1087–1093, 2002.

Wilks, D. S.: *Statistical Methods in the Atmospheric Sciences*, edited by R. Dmowska and H. J. R., Academic Press, Inc., San Diego., 1995.

Yatavelli, R. L. N., Lopez-Hilfiker, F., Wargo, J. D., Kimmel, J. R., Cubison, M. J., Bertram, T. H., Jimenez, J. L., Gonin, M., Worsnop, D. R. and Thornton, J. a.: A Chemical Ionization High-Resolution Time-of-Flight Mass Spectrometer Coupled to a Micro Orifice Volatilization Impactor (MOVI-HRToF-CIMS) for Analysis of Gas and Particle-Phase Organic Species, *Aerosol Sci. Technol.*, 46(12), 1313–1327, doi:10.1080/02786826.2012.712236, 2012.